Dilepton Production in Pb–Au Collisions at 158 GeV per Nucleon Using the CERES Detector

Evgeny Socol

Particle Physics Department
The Weizmann Institute of Science
Rehovot, Israel.

September 1999

Dilepton Production in Pb–Au Collisions at 158 GeV per Nucleon Using the CERES Detector

Evgeny Socol

Particle Physics Department
The Weizmann Institute of Science
Rehovot, Israel.

Thesis presented to the Feinberg Graduate School
of the Weizmann Institute of Science for the degree of Ph.D. in Physics

supervisor: Prof. Itzhak Tserruya

September 1999

Abstract

This thesis deals with the measurements and results of inclusive e^+e^- pair production in ultra-relativistic Pb–Au collisions at 158 GeV per nucleon. The measurements were performed in the framework of the CERES experiment at the CERN SPS.

The field of ultra-relativistic heavy-ion collisions is particularly interesting in light of the prediction of QCD that at high temperatures and/or high baryon densities matter is expected to undergo a phase transition leading to a deconfined state – called quark-gluon plasma (QGP) – and to chiral symmetry restoration. Dileptons provide a unique probe of these predictions. Since they interact only electromagnetically, they have a long mean free path and therefore carry information about the fireball – earliest and most interesting stage of the collision.

CERES is the only experiment dedicated to the measurement of low-mass (m < 1.5 GeV/c^2) electron-positron pairs and direct photons produced in ultra-relativistic heavy-ion collisions at the CERN SPS. In order to perform this interesting and challenging experiment CERES has developed a dedicated spectrometer. It covers the pseudorapidity region $2.05 < \eta < 2.65$ with 2π azimuthal symmetry and accepts a very broad range of p_t. The essential components of the CERES spectrometer are two Ring Imaging Cherenkov detectors (RICH) – one situated before, the other after a short solenoid which provides an azimuthal kick between the two RICH radiators. The coils shape the field lines such that the first RICH has practically zero field, and the second RICH has straight field lines pointing to the target. With this spectrometer, CERES has carried out over the last seven years a systematic research programme with p, S and Pb beams, including p–Be and p–Au collisions (1993) at a beam energy 450 GeV, S–Au collisions (1992) at 200 GeV per nucleon and Pb–Au collisions (1995-96) at 158 GeV per nucleon.

In 1994-95 the CERES spectrometer was considerably upgraded in order to cope with Pb-induced collisions. The main items of the upgrade were a doublet of silicon drift detectors (SiDC) located just after the target, and a multiwire proportional counter with pad readout (the pad chamber, PC) located behind the double RICH spectrometer.

This thesis deals with the upgrade and with the analysis of the 1995 and mainly the 1996 Pb–Au data. The emphasis of this work is in achieving the best accuracy in the measurements, both hardware-wise and software-wise. In the data analysis, a new approach was developed for the systematic study and suppression of the combinatorial background. The main result is that within the experimental errors, dominated by 25% systematic errors in the mass range $0.2 < m < 1.5$ GeV/c^2, there is an enhancement by a factor of $\sim$1.8 of the measured e^+e^- yield over the yield from the known hadronic sources. The enhancement is most pronounced in the mass range $0.2 < m < 0.7$ GeV/c^2 and at low e^+e^- transverse momentum ($p_t < 500$ MeV/c). Although the error bars are large, the data clearly indicate a non-linear dependence of the excess as a function of multiplicity.

Acknowledgements

This thesis summarizes a significant part of 6-year period of my life. Too many people should be mentioned as those who helped, and I apologize before those who are not mentioned explicitly.

First of all it is a pleasure for me to thank my advisor Prof. Itzhak Tserruya for inviting me to join one of the most beautiful experiments in the High Energy Physics field. His role in running the CERES experiment at its decisive stage, in which I had a blessing to take part, cannot be overestimated. I want to thank him for his really infinite patience, permanent encouragement and constant help in both science and life.

I want to thank Prof. Shmuel Gurvitz and Dr. Asher Shor for their constant interest to this work and innumerable discussions. My thanks also to Prof. Benjamin Svetisky for several extremely helpful consultations.

Many thanks to all the Weizmann CERES group members, especially to Dr. Ilia Ravinovich for guidance and help, to Alexander Cherlin for help with MC studies and to Alexander Milov for many discussions. I want also to thank everybody who helped me in CERN, especially Prof. Axel Drees, Prof. Peter Glassel, Dr. Andreas Pfeiffer and Dr. Bjoern Lenkeit.

Thank you all.

Contents

List of Figures

List of Tables

Chapter 1

Introduction

This work is dedicated to e^+e^- pair production ($m_{e^+e^-} < 1.5$ GeV/c^2) in Pb–Au collisions at $158 \cdot A$ GeV/c measured by the CERES (**Ch**E**r**enkov **R**ing **E**lectron **S**pectrometer) experiment in 1995-96 at the SPS accelerator at CERN. This chapter deals with the physics background and the motivation for performing the experiment. We begin with a short overview on relativistic heavy-ion collisions which is the general framework of the CERES experiment.

1.1 Ultra-relativistic heavy-ion collisions

The relatively new interdisciplinary field of ultra-relativistic heavy-ion collisions has emerged from the domains of particle physics and nuclear physics. Combining the elementary-interaction aspect of high-energy physics with the macroscopic-matter aspect of nuclear physics, the subject of heavy-ion collisions is the study of bulk matter consisting of strongly interacting particles (hadrons and quarks). It may therefore be called "condensed matter physics" of elementary particles. The energy scale is given by Λ_{QCD} or the pion mass, both of the order of 150 MeV. What makes this field particularly interesting is the prediction of QCD that at high temperatures and/or high baryon densities matter is expected to undergo a phase transition to a new state called quark-gluon plasma[1] (QGP), where quarks and gluons are free to move over a volume large compared to the hadron size. Chiral symmetry restoration is also predicted to occur under those conditions. At low temperature and density, quarks and gluons are bound (confined) by the strong force into colorless objects, the hadrons. When increasing the energy density by increasing the temperature ("heating") or the matter density ("compressing"), a phase transition occurs, where partons are deconfined and chiral symmetry is approximately restored. When chiral symmetry is restored the quark condensate $< q\bar{q} >$ drops to zero and consequently a detectable decrease in the mesons masses is expected [8]. It is not clear whether deconfinement and chiral symmetry restoration are two different phase transitions or only one. In any case the two phenomena are expected to occur under very similar conditions of temperature and density.

Confinement is one of the most challenging theoretical problems in high-energy physics. It

[1] There is an enormous literature on QGP. Recent review articles can be found in refs. [1, 2, 3]. A detailed coverage of both theoretical and experimental aspects of the subject can be found in the recent Quark-Matter Conference proceedings [4]– [7].

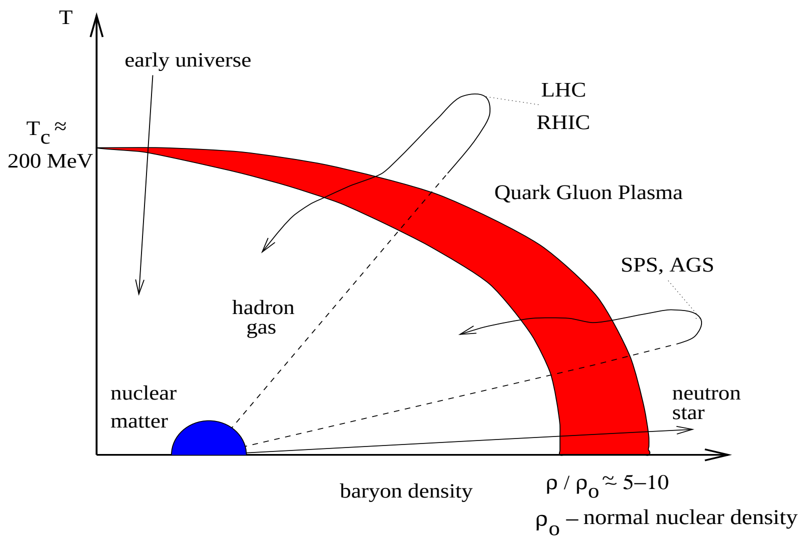

Figure 1.1: The phase diagram for the quark matter to hadron gas phase transition.

is very difficult to treat it since the energy scale is low (of the order of one GeV or below) and consequently perturbation methods of QCD are not applicable. The chiral symmetry restoration is also a very attractive issue.

Fig. 1.1 shows a schematic phase diagram of the transition from hadronic to quark matter. The estimated temperature and baryon density conditions for the phase transition are indicated in the figure. The study of the deconfined QGP phase is relevant not only to high-energy physics. Cosmology and astrophysics have also an interest in this field. The upper-left part of the diagram corresponds to the early universe, a few μs after the Big Bang, when the temperature was high and the relative baryon density was low; the other extreme of low temperature and high baryon density may be close to the conditions inside neutron stars. High-energy ion collisions allow to scan this phase diagram going from the baryon rich to the baryon free region as the collision energy increases. The phase transitions are expected to occur at energy densities of the order of 2-3 GeV/fm^3, so a necessary prerequisite is the deposition of a large amount of energy in the small collision region. The acceleration at the CERN SPS (Super Proton Synchrotron) of S ions to an energy of 200 GeV per nucleon and of Pb ions to an energy of 158 GeV per nucleon provided the proper tools for these studies and apparently allow to reach the desired energy density [9].

1.2 Dileptons in ultra-relativistic heavy-ion collisions.

1.2.1 Importance

Lepton pairs are expected to be a good probe of the initial fireball. Since they interact only electromagnetically, they have a long mean-free-path and once formed they can leave the interaction region without any additional interactions. The main interest is to identify the thermal radiation emitted by the system. Because of the strong temperature dependence of the Stephan-Boltzmann law, the major fraction of the thermal radiation is expected to be emitted during the hottest, i.e. the earliest part of the collision. The dileptons can be emitted through $q\bar{q}$

annihilation in the QGP phase or through $\pi^+\pi^-$ annihilation in the dense hadron gas (HG). The shapes of the thermal radiation from the QGP and the HG phases are expected to be very different and consequently the identification of the thermal radiation can tell us the nature of the matter formed in the collision. Dileptons originating from $\pi^+\pi^-$ annihilation have a sharp threshold at $2m_\pi$ and a broad peak around the mass of the ρ meson (in the vector dominance model the $\pi^+\pi^-$ annihilation cross-section is dominated by the pole at the ρ mass of the π electromagnetic form-factor). In contrast, the $q\bar{q}$ annihilation yields an exponential shape with inverse slope parameter reflecting the temperature of the system.

In addition, dileptons provide a tool to study the production of the vector mesons ρ, ω and ϕ through their leptonic decays. This is of particular interest with regard to the ρ meson. Its lifetime is very short (1.3 fm/c) compared to the typical lifetime of the fireball of 10-20 fm/c, so almost all ρ mesons decay inside the fireball. If chiral symmetry restoration takes place, the ρ meson will decay with a reduced mass providing a unique experimental opportunity to detect the onset of this phase transition [8]. The ϕ meson is also very interesting [10]. ϕ-production is suppressed in proton – proton (p – p) collisions by the OZI rule [11], whereas in a QGP the OZI rule will not apply. Furthermore, if chemical equilibrium is achieved in the plasma, strangeness production is expected to be enhanced [12]. Consequently the ratio of ϕ-meson to non-strange meson production is expected to be several times larger, than that found in p – p collisions.

In order to identify any new physics from electron pairs produced in heavy-ion collisions, one has to compare the results with the yield of electron pairs in p – p collisions. The latter have been the subject of intensive studies over the last two decades. A schematic view of the e^+e^- invariant mass spectrum is shown in Figure 1.2. One can distinguish three regions in this spectrum:

1. The high mass region at $m \geq 3$ GeV/c^2 includes the J/Ψ and the Ψ' resonances and a continuum dominated by the Drell-Yan (D-Y) mechanism [13].

2. The intermediate mass region, $m_\phi < m < m_{J/\Psi}$, is dominated by the semi-leptonic decay of the charmed mesons $D\bar{D}$ and by the D-Y process.

3. The low mass region at $m \leq 1.5$ GeV/c^2, where most of the cross section lies, includes

   - the Dalitz decays of the π^0, η, $\eta\prime$ and ω;
   - the resonance decay of the ρ^0, ω and ϕ.

An additional source of e^+e^- pairs comes from hadronic bremsstrahlung. It contributes at the very low masses, and is practically negligible in our case due to the p_t cut of 200 MeV/c applied in the analysis to the e^- and the e^+ tracks (see Chapter 3).

If a QGP is formed, signs of new physics are expected in all three regions:

- J/Ψ suppression in the high mass region. The prediction that J/Ψ production should be suppressed in a QGP is based on the Debye color screening of the $c\bar{c}$ binding potential by the free color charges moving in the deconfined medium [14];

- enhanced open charm production [15] and thermal radiation from the QGP in the intermediate mass region [16];

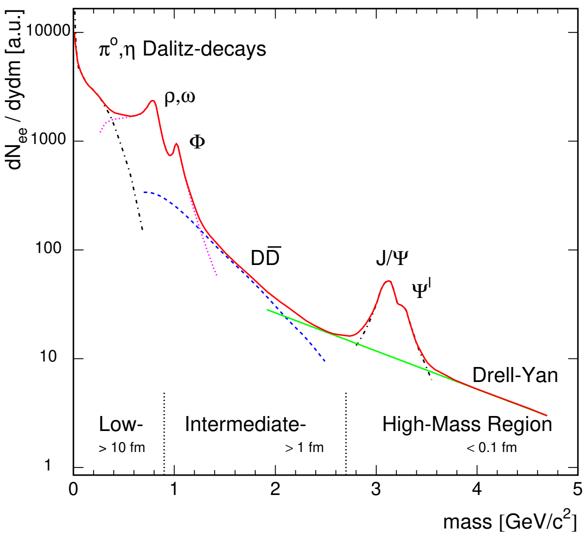

Figure 1.2: Schematic view of the e^+e^- mass spectrum in $p-p$ collisions (not to scale).

- thermal radiation from the HG, change of vector meson properties and ϕ enhancement [10] in the low mass region.

Indeed, most of these signs have been observed experimentally in the heavy-ion programme of the CERN SPS, in particular (i) an anomalous J/Ψ suppression in $Pb-Pb$ collisions, (ii) an enhancement of dimuons in the intermediate mass region and (iii) a strong enhancement of low-mass dileptons. The latter will be discussed in this work in great details. For the other two, see the proceedings of the last Quark Matter Conferences [6, 7].

Dileptons in the low mass region and direct photons are the main topics of the CERES physics program. The motivation to study direct photons is the same as for dileptons since real and virtual photons are expected to carry the same physics information. However, the measurement of photons is much less sensitive to a new source due to the much larger physics background, as compared to dileptons. This thesis deals only with the low mass e^+e^- pair production measured by CERES in $Pb-Au$ collisions.

1.2.2 Experimental challenge

The interest in the measurement of low-mass dielectrons is matched by the difficulty of their experimental detection. There are three main experimental challenges that an experiment attempting to measure dielectrons in ultra-relativistic heavy-ion collisions has to deal with.

- The source of dielectrons is very weak. The same reason that makes the dileptons a unique probe of the first stages of collision – namely the absence of strong interactions – makes their yield extremely low: about $3.1\cdot10^{-6}$ e^+e^- pairs with invariant mass $m > 200$ MeV/c^2 per charged particle. This weak source must be detected in the presence of

- a strong yield of e^+e^- pairs of trivial origin: γ-conversions and π^0-Dalitz decays; π^0-Dalitz decays contribute about $6\cdot10^{-3}$ e^+e^- per charged particle;

- hundreds of charged particles per central collision, which produce a serious load on the detectors.

In the absence of any rejection, misidentified tracks of pairs of trivial origin lead to a huge combinatorial background, which increases quadratically with the event multiplicity. The transverse momentum cut on single electrons allows to improve considerably the signal-to-background ratio. Namely, applying a $p_t > 200$ MeV/c cut reduces the signal (e^+e^- pairs with invariant mass $m > 200$ MeV/c^2) by less than factor of 2 (from $3.1 \cdot 10^{-6}$ to $1.8 \cdot 10^{-6}$ per charged particle), while the π^0-Dalitz e^+e^- pair yield goes down by a factor of 30 (from $6 \cdot 10^{-3}$ to $2 \cdot 10^{-4}$ e^+e^- per charged particle). Consequently, the combinatorial background goes down (depending on event multiplicity) by several orders of magnitude. The hardware and software means to deal with the combinatorial background problem will be described in detail in the next chapters.

1.3 The CERES experiment

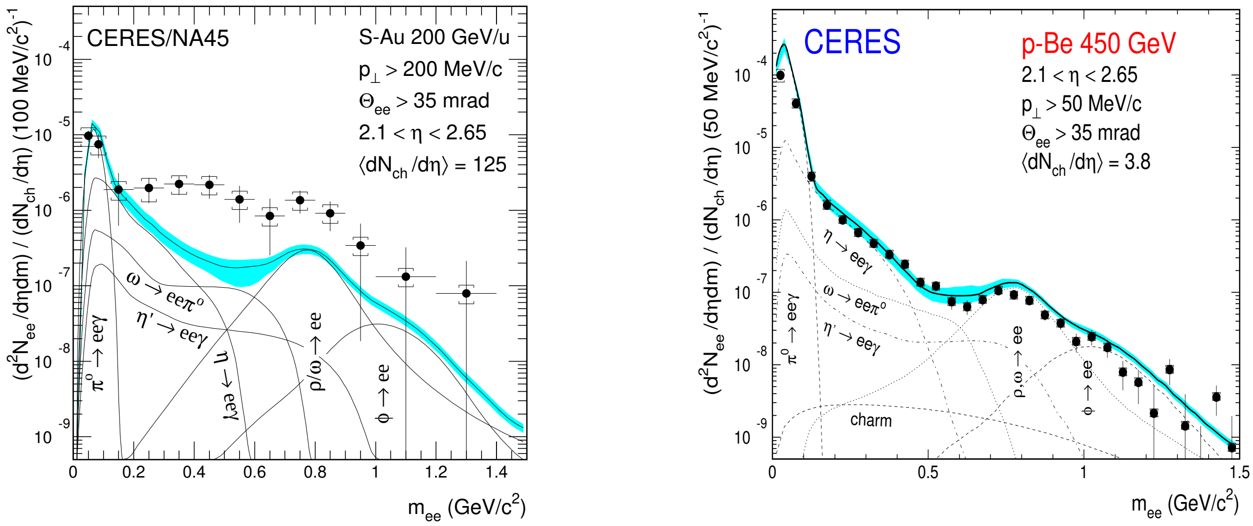

Figure 1.3: Mass spectra of inclusive e^+e^--pairs in S–Au[19] (left) and p–Be[18] (right) collisions showing the data (full circles) and the various contributions from hadron decays. Systematic (brackets) and statistical errors (bars) are plotted independently of each other. The shaded regions indicate the systematic error on the summed contributions.

CERES is the only experiment dedicated to the measurement of low-mass ($m < 1.5$ GeV/c^2) electron-positron pairs in ultra-relativistic heavy-ion collisions at the CERN SPS.

In order to perform this interesting and challenging experiment CERES has developed a dedicated spectrometer [17] which is briefly described in the next chapter. With this spectrometer, CERES has carried out over the last seven years a systematic research programme with p, S and Pb beams, including the following measurements:

- p–Be and p–Au collisions (1993) at a beam energy 450 GeV,

- S–Au collisions (1992) at 200 GeV per nucleon,

- Pb–Au collisions (1995, 1996) at 158 GeV per nucleon.

As a starting point of the work described in this thesis, the results could be summarized as follows: while in p–Be and p–Au collisions the results are very well reproduced by the known hadronic sources [18], in S – Au collisions, CERES saw a clear enhancement of low-mass pairs, which seems to increase non-linearly with event multiplicity [19]. The results are shown in Fig. 1.3. The ordinate is the probability density function (*pdf*) of the e^+e^- pair yield, normalized to the total charged particles yield (both per unit of rapidity). The *pdf* is measured in inverse mass units.

These results have triggered a considerable theoretical activity (see sect. 4.4.3 for an overview and references), mainly stimulated by the possibility that they may hint to chiral symmetry restoration.

In 1994-95 the CERES spectrometer was considerably upgraded in order to cope with Pb-induced collisions (the Pb beam became available at the CERN SPS in the fall of 1994). This thesis deals with this upgrade and with the analysis of the 1995 and mainly the 1996 Pb–Au data.

The rest of this thesis is organized as follows:
Chapter 2 reviews the CERES spectrometer and the upgrade scheme. I concentrate on the topics to which I have significantly contributed :
– design, production, tuning operating conditions and performance evaluation of the Pad Chamber;
– design of slow-control (high voltages) and monitoring (temperature, pressure, gain in UV detectors) software;
– refurbishing of UV-1 detector.
Chapter 3 describes the data analysis, concentrating on the parts in which I was heavily involved – namely, intercalibration of the different detectors and the whole signal extraction chain after the primary data reduction. The latter includes choosing relevant parameters for the background rejection, optimizing the cut values, and finally extracting the physical signal out of the combinatorial background.

Finally, chapter 4 presents the physical results, their comparison with other data sets, theoretical interpretations, summary and outlook.

Chapter 2

Spectrometer Upgrade and Data Taking

In the framework of this work I played an active role in the design, construction, operation and performance evaluation of the Pad Chamber, and in refurbishing of the UV-1 detector. I also developed the whole slow-control software of the CERES experiment which was used during the Pb runs. In this chapter I concentrate in these items, but I start with an overview of the experimental set-up for completeness.

2.1 Experimental setup

The CERES spectrometer (Fig. 2.1) is optimized to measure low-mass electron pairs from about ~ 50 MeV/c^2 up to ~ 1.5 GeV/c^2, limited at the upper end by statistics. It covers the pseudorapidity region $2.1 < \eta < 2.65$ with 2π azimuthal symmetry and accepts a very broad range of p_t. A detailed description of the original CERES set-up can be found in [17].

The essential components of the CERES spectrometer are two Ring Imaging Cherenkov detectors (RICH) – one situated before, the other after a short superconducting double solenoid. An electron produced in the target emits Cherenkov photons while traversing the radiator volume filled with CH_4. The Cherenkov light is reflected backward by the spherical mirror producing a ring image at the mirror focal plane. The ring images are read out by UV-sensitive gas detectors consisting of three amplification stages, two Parallel-Plate Avalanche Chambers (PPAC) and one Multi-Wire Proportional Counter (MWPC) (for a complete description of the UV detectors the reader is directed to refs. [20] and [21]). The magnetic field provides an azimuthal kick between the two RICH radiators. The main coils and the outer warm correction coils shape the field lines such that the first RICH has practically zero field, and the second RICH has straight field lines pointing to the target i.e. parallel to the trajectories of the particles and therefore not affecting them (a few field lines are drawn in the lower part of Figure 2.1).

For the Pb runs, which started in 1995, the set-up included also external tracking detectors: a doublet of silicon radial-drift detectors (SiDC) located downstream of the target and before RICH-1, and a multiwire proportional chamber with pad readout (the pad chamber, PC) downstream of RICH-2.

There are several essential features in the design of the CERES spectrometer of particular

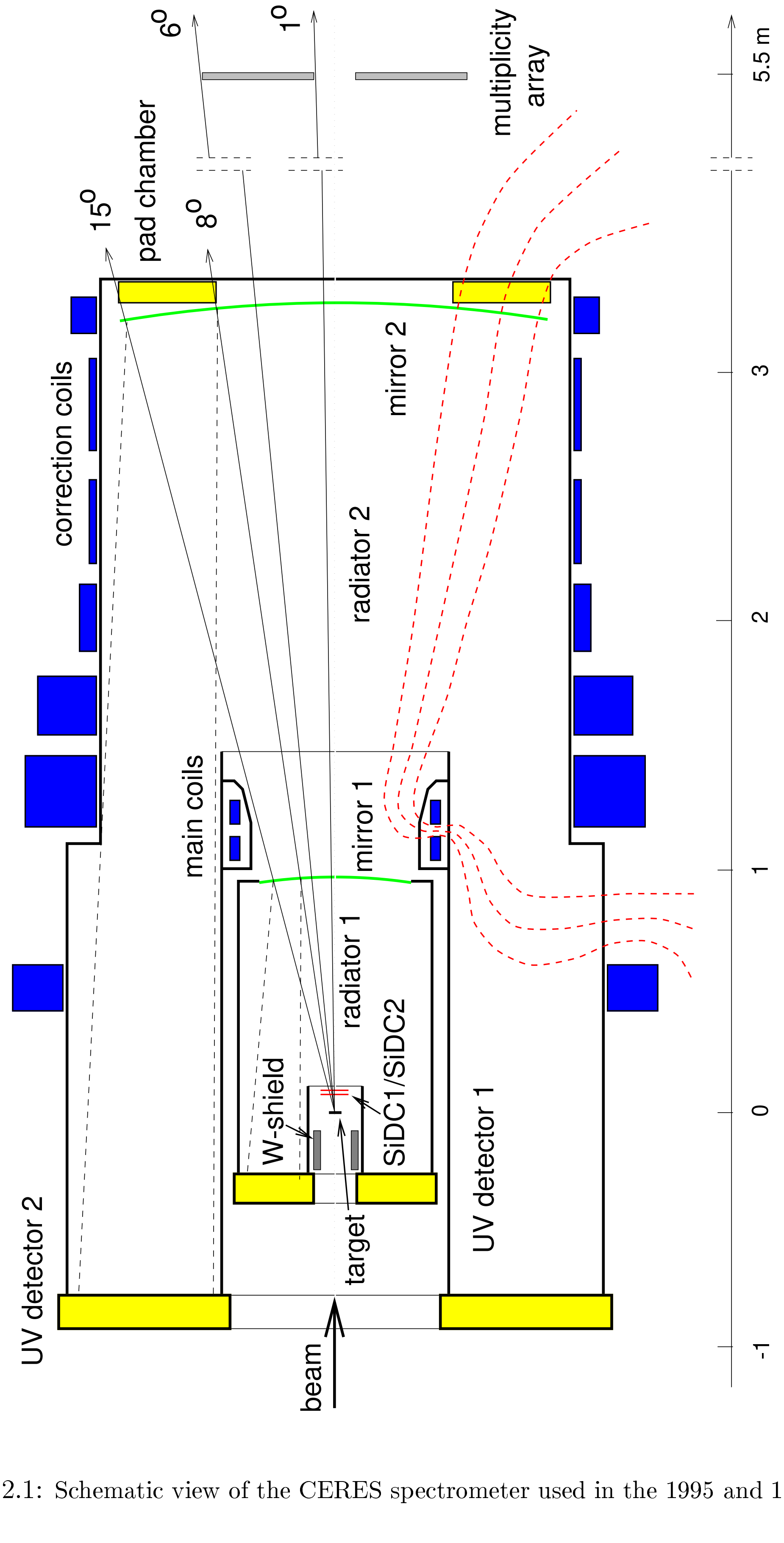

Figure 2.1: Schematic view of the CERES spectrometer used in the 1995 and 1996 runs.

importance for the detection of electron pairs and for its operation at high multiplicities.

- The two RICHes are almost “blind” to hadrons. The radiators of the RICH detectors are filled with CH_4 at atmospheric pressure, which has a threshold of $\gamma_{th} \simeq 32$. This high value ensures that essentially only electrons emit Cherenkov radiation when traversing the detector.

- The UV detectors are placed upstream of the target, and thus they are not traversed by the intense flux of forward-going charged particles produced in the interaction.

- The amount of material within the acceptance (not counting the target) is kept below 1% of a radiation length. This minimizes the amount of γ-conversions which would otherwise contribute to the combinatorial background.

- The shape of the magnetic field results in a field-free region in RICH-1. This is of extreme importance since it allows to recognize and reject π^0 Dalitz decays and conversion pairs by their small opening angle.

- The external tracking detectors are essential to cope with the high multiplicity environment in central Pb–Au collisions. They add redundancy to the directional tracking of the RICH detectors and considerably reduce the amount of fake tracks (see sect. 3.5.1). Furthermore, they provide additional background rejection (sect. 3.5.3) and improve the momentum and mass resolutions of the spectrometer.

2.2 Upgrade – overview

The spectrometer in its original concept – namely with only one Silicon Drift Chamber and no Pad Chamber – would not be able to cope with the higher background and the higher multiplicities of central Pb – Au collisions. The reason is that the ring-recognition efficiency decreases, and simultaneously the amount of fake rings (random combinations of hits in the RICH detectors) increases with the event multiplicity. These two problems are aggravated by the fact that the location of the ring centers is unknown, and therefore the whole detector area needs to by searched for the presence of rings. This procedure was completely adequate for proton-induced collisions where the background is small and the events are rather clean. It was still acceptable for S–Au central collisions where the average charged particle rapidity density is $dN_{ch}/d\eta \sim 125$, but would completely fail in the Pb case according to our simulations. With increasing amount of rings per event, both genuine and fake, it is not possible to achieve enough rejection without seriously vetoing the signal.

To cope with these problems the CERES detector has been considerably upgraded in 1994 – 1995. The essence of the upgrade is the addition of new detectors to provide external tracking and information on the ring center location in RICH-1 and RICH-2. The main items of the upgrade are:

- A doublet of SiDC located 100 mm after the target with a 15 mm spacing between them. Their acceptance is slightly larger than 1 unit of pseudorapidity. They provide the (θ, φ) coordinates of all charged particles produced in the collision. This allows a precise vertex reconstruction without any additional information from RICH-1. The SiDC are also used for the determination of the pseudorapidity density of charged particles, $dN_{ch}/d\eta$. In addition to that, they play together with RICH-1 an essential role in identifying close electron pairs from conversions and π^0 Dalitz decays (see chapter 3).

CERES was the first experiment to successfully exploit SiDCs. A detailed description of these detectors is given elsewhere [22]. The basic principle of operation is the following: a charged particle traversing the SiDC produces an electron cloud inside the depleted region that spans the whole thickness of the silicon wafer. Due to the radial electric field, generated by a set of concentric rings, the cloud drifts radially (with velocity v_{drift}) towards the anode located at the outer circumference (R_{out}) of the wafer. The anode is segmented azimuthally in 360 pixels with 1° pitch and the charge is collected by one or (preferably) several pixels.

- A multiwire proportional counter (MWPC) with pad readout (the pad chamber, PC) located behind the spectrometer, after the RICH-2 mirror. The pad chamber plays for RICH-2 the same role that the two SiDC do for RICH-1. It provides external tracking behind RICH-2, giving an a priori information of the ring center location in RICH-2 and thus helping to fight the fake ring problem. A detailed description of this detector which was designed, constructed and installed by our group, is given in the following section.
- A new data acquisition system (DAQ) almost one order of magnitude faster than the one previously used.
- A new first level trigger (FLT) based on an array of 24 scintillators located behind the detector (the 64-pad silicon detector of the original set-up had to be removed due to limited space in the target area, to make room for the installation of the second silicon drift chamber).

2.3 The pad chamber

The Pad Chamber was added to the CERES spectrometer, as mentioned above, in order to provide external tracking behind RICH-2. As a by-product, the Pad Chamber together with the doublet of SiDC allows to do hadron tracking and to study several interesting hadron properties (like p_t and multiplicity distributions, etc. – see [23] and [24]). In addition, the Pad Chamber proved to be an undispensible tool in the geometrical intercalibration of the detectors, providing a parameter-free common reference for the silicon and the RICH detectors (see sect. 2.1 and 3.2).

2.3.1 Design

Since the new tracking detector has to track particles after their deflection in the magnetic field, the only place to put it (see Fig. 2.1) is behind the whole installation, at a distance of ~3.3 m from the target. In order to cover the fiducial pseudorapidity interval of the CERES spectrometer, namely $2.05 < \eta < 2.65$, the detector has an inner (outer) active radius of

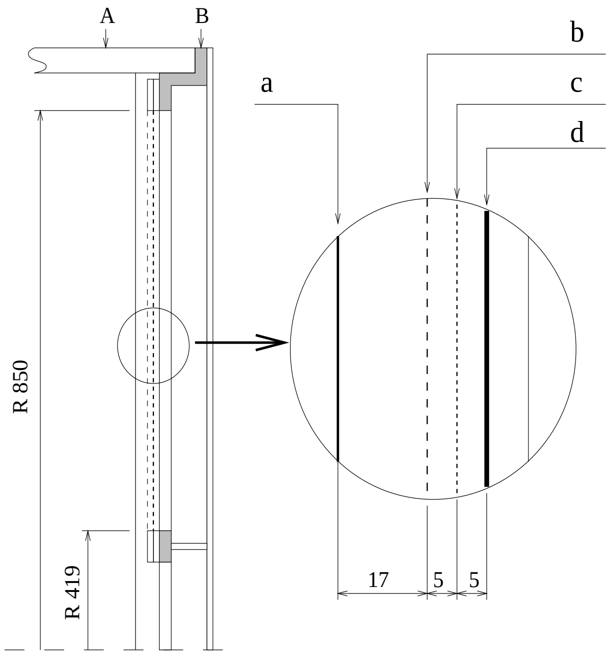

Figure 2.2: The Pad Chamber lay-out. All dimensions are in mm. a – RICH-2 exit window, b – upstream mesh cathode, c – multiwire anode, d – pad cathode. A – RICH-2 end flange, B – the Pad Chamber vessel.

R_{in} = 419 mm (R_{out} = 850 mm). A multiwire proportional counter (MWPC) is the most appropriate choice for a detector of such size, combining sufficient efficiency (close to 100%) and resolution (down to 1 mm or less) with low (in respect to other alternatives) cost. A MWPC is more stable in a heavy-ion beam environment than a parallel plate avalanche counter (PPAC) – see [21] for discussion and comparison.

Pad readout electronics were successfully developed and used by CERES for the RICH detectors. The same electronics was adopted for the new detector so that no new electronics had to be designed. This fixed the pad size to be 7.62×7.62 mm^2, as in RICH-2.

2.3.2 Geometry and construction

The chamber (Fig. 2.2) is made of three electrodes (wire anode, mesh cathode and pad cathode). It is symmetric with a cathode-anode distance of 5 mm on both sides. The chamber is attached directly to the RICH-2 radiator end flange. The upstream cathode is located at a distance of 17 mm from an aluminized mylar foil which serves as exit window of the RICH-2 radiator.

The upstream cathode is made of a stainless steel mesh with 50 μm diameter wire and a pitch of 0.5 mm. This electrode was produced in one piece, the mesh being stretched between two concentric rings of G10 without any spokes using the same procedure and tooling that were previously developed by our group for the construction of the UV detectors [20].

The second electrode is the wire anode. It is made of 30 μm diameter gold plated tungsten wires spaced by 3 mm. Initially, it was proposed to make the wire anode as in UV-2 [20], where

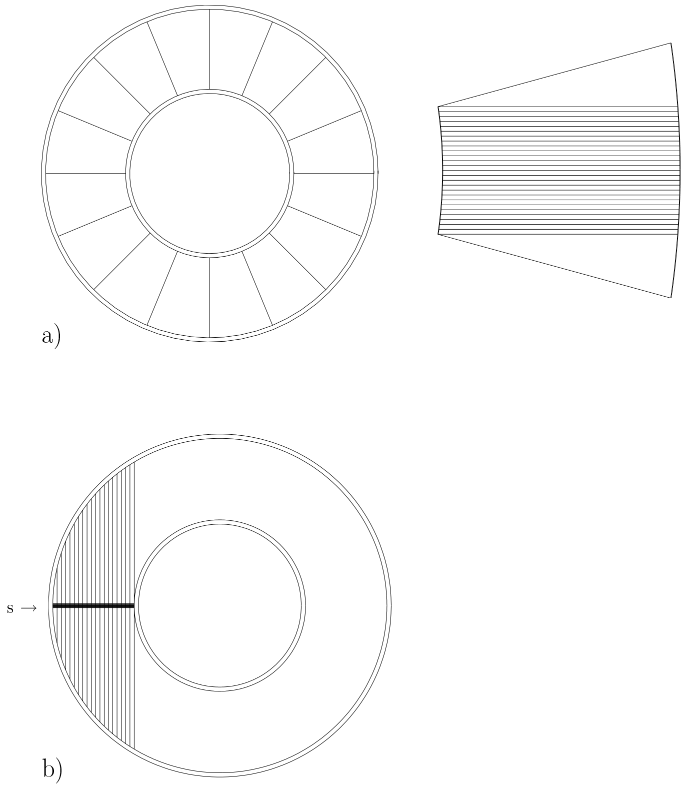

Figure 2.3: Wire anode of UV-2(a) and wire anode of the pad chamber(b). s – 3 mm spoke.

the electrode is divided azimuthally in 16 sectors by radial spokes, and the wires within each sector are parallel to the central radius of that sector as shown in Fig. 2.3a. The advantage of this scheme is that the mechanical stresses are almost compensated due to the circular geometry. However, we decided that in the pad chamber all wires will be parallel to each other (Fig. 2.3b) in order to avoid the dead area (about 10%, that leads to 20% inefficiency for pairs) resulting from the use of the spokes.

Since no winding machine was available for the nearly 2m long wires needed, we have developed a procedure and constructed the necessary tooling for precise manual positioning of the wires. The essensial part which provides accurate placing of wires is a CNC-produced "comb". A tension of 100g was applied to each wire by hanging a copper rod of appropriate size. This is comfortably below the elastic limit (140g) for a 30 μm tungsten wire. The pad chamber was designed to cope with 5 KV accross the gap. With this voltage, the longest wires of the electrode would be close to the staggering instability [25]. To avoid that, the wires were glued onto a small spoke (3 mm wide) in the middle of the electrode (see Fig. 2.3). All three electrodes are attached to the detector vessel made of stainless steel. The vessel itself served as a jig plate during the construction of the electrodes.

The pad electrode with ~29 000 pads and the asssociated electronics were produced by the

Heidelberg University group.

2.3.3 Operating conditions

The chamber was tested with argon based mixtures, using different quenchers – carbon dioxide (CO_2), methane (CH_4) and isobutane (iC_4H_{10}) – at $\sim$ 10% (volume) level. The performance of the detector was essentially the same with all three mixtures. We finally decided to use 90/10 Ar/CO_2 mixture, because of the smaller drift velocity in the CO_2, which is better matched to the trigger and readout sequence of the front end electronics. After the tests, the detector was attached to the CERES spectrometer (directly to the end flange of the radiator tank of RICH-2), just in time to be used as an integral part of the CERES set-up during the 1995 Pb beam run.

In an Ar – based mixture, about 100 e/cm are deposited by a minimum ionizing particle (ref. [25], Table 1). In 90/10 Ar/CO_2 mixture and 2000 V across the gap, the anode-cathode region drift velocity is saturated at about 5 cm/μs [25]. This means that electrons deposited in the anode-cathode region will be collected during $\sim$100 ns (5 mm / (5 cm/μs)) after the nuclear collision – whereas the CERES first level trigger is available at about 200 ns. So in order to collect all the primary charges available, the first electrode was kept at a positive potential of 100 V while the exit window of the radiator was kept at ground potential. We are thereby collecting also the charges deposited between the RICH-2 exit window (denoted by **a** at Fig.2.2) and the upstream mesh cathode (**b**), bringing the ionization path to a total length of 27 mm (see Fig.2.2). The drift velocity in the drift region is about 4 mm/μs [25] (100 V over 17 mm produce an electric field of 60 V/cm), and the total drift time is about 4.25 μs. Since the charge integration time of the pad readout electronics is about 2 μs, less than half the charge deposited in the drift region is collected.

Summarizing, a total of about 250 primary charges are deposited by a minimum-ionizing particle in the MWPC (ionization path of 27 mm). However, the "effective" (i.e. collected) total primary charge is only about 80 electrons (only electrons from the 17 mm drift region can be collected, and half of them are lost due to insufficient integration time).

2.3.4 Hit reconstruction software

The electronic avalanche produced by a charged particles transvesing the Pad Chamber (hit) induces a signal in a group of pads. The raw Pad Chamber event consists of the location and pulse height of each of the pads. Before the hit recognition, an event clean-up is performed. This is necessary because on top of the hits from charged particles, we have occasionally large clusters of pads originating either from a highly ionizing particle traversing the detector plane at a small angle (with respect to the plane itself), or from the electronic noise of excited pads from defective electronic modules. These clusters have to be removed in order to minimize the number of fake hits and tracks. There are also isolated pads and two-pad clusters (mainly due to pedestal fluctuations) which have to be removed as well. To illustrate the clean-up procedure, we show in Fig. 2.4 a typical event on the Pad Chamber before and after the clean-up.

A hit on the Pad Chamber is defined as the center of gravity of a cluster of pads (a cluster is defined as a group of connected pads with a signal above threshold). The hit amplitude is measured in the range 1-255 (from the 8-bit digitization of the analog signal). A cluster may

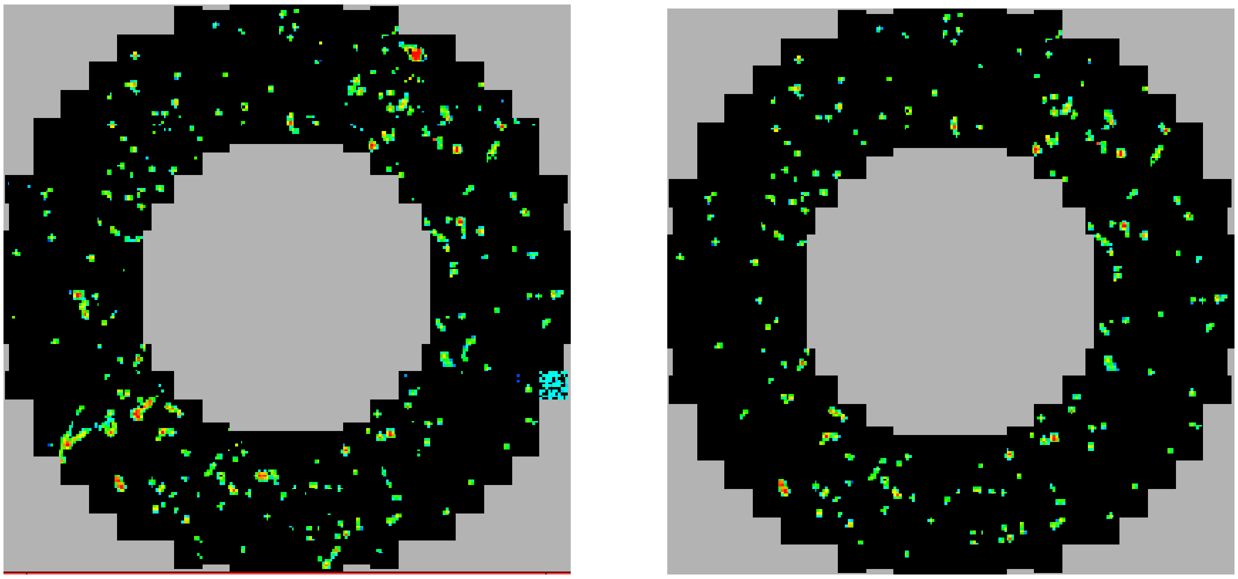

Figure 2.4: A typical Pad Chamber event before (left) and after (right) clean-up.

contain more than one hit if two or more of them fall close to each other. The procedure of hit recognition starts from the determination of local maxima in a cluster, with the amplitude threshold kept at its minimal value of one count. If there are more than one local maximum, a hit split algorithm is performed. The amplitude threshold is increased by one count at a time till the cluster breaks up into two or more subclusters, which are defined as single hits.

2.3.5 Performance evaluation

Pulse height and gain.

Figure 2.5 shows the pulse height distribution (in units of ADC; each ADC unit corresponds to $\sim$ 1800 electron charges–e) of a minimum ionizing particle for a voltage of 2050 V accross the anode-cathode gap. The solid line is a fit to the Landau expression [25]

$$f(a) \sim exp(-\frac{x + e^{-x}}{2}),$$

where $x = (a - a_0)/\sigma_a$ with parameteres $a_0 = 100$ (peak location), σ_a=30 ADC counts. The average signal is $2.3{\cdot}10^5$ e. Since the effective number of primary electrons is about 80 (see sect.2.3.3), and the fact that the induced charge is collected from only one of the two cathodes, the charge multiplication factor of the chamber is approximately $6 \cdot 10^3$.

Position resolution

The position resolution was estimated using the matching between the two silicon drift detectors SiDC-1, SiDC-2 and the Pad Chamber. If we denote by
σ_1, σ_2, σ_p – the radial (θ) resolutions of SiDC-1, SiDC-2 and PC respectively, then the position resolution σ_s of the SiDC doublet ($\theta = 0.5(\theta_1 + \theta_2)$) is:

$$\sigma_s^2 = (\sigma_1^2 + \sigma_2^2)/4.$$

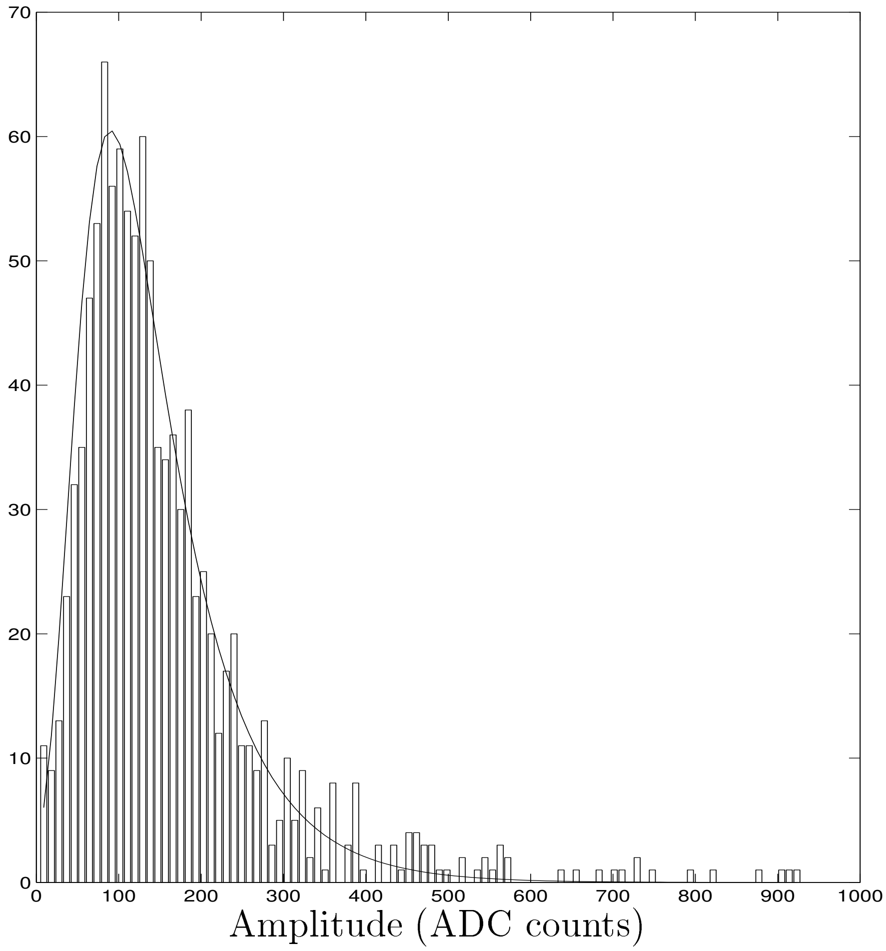

Figure 2.5: The Pad Chamber hit amplitude distribution (histogram) together with a fit to a Landau distribution (solid line).

The dispersion S_{12} of the SiDC1-2 $\Delta\theta = \theta_2 - \theta_1$ distribution is given by:

$$S_{12}^2 = \sigma_1^2 + \sigma_2^2,$$

and for S_{sp} – the dispersion of the SiDC – PC $\Delta\theta$ distribution we obtain

$$S_{sp}^2 = \sigma_s^2 + \sigma_p^2 = 0.25\,(\sigma_1^2 + \sigma_2^2) + \sigma_p^2 = 0.25\,S_{12}^2 + \sigma_p^2$$

We immediately obtain from this the relevant dispersion of the Pad Chamber position accuracy

$$\sigma_p^2 = S_{sp}^2 - 0.25 S_{12}^2$$

Using a sample of high-momentum ($p > 6$ GeV/c) π tracks identified in the two RICH detectors, for which multiple scattering is negligible, yields: $S_{12} = 0.6$ mrad, $S_{sp} = 0.7$ mrad (see Fig. 2.6). So finally the Pad Chamber position resolution is σ_p= 0.63 mrad = 0.27 pads.

Efficiency.
The detector efficiency was estimatied using the matching between the SiDC and the Pad

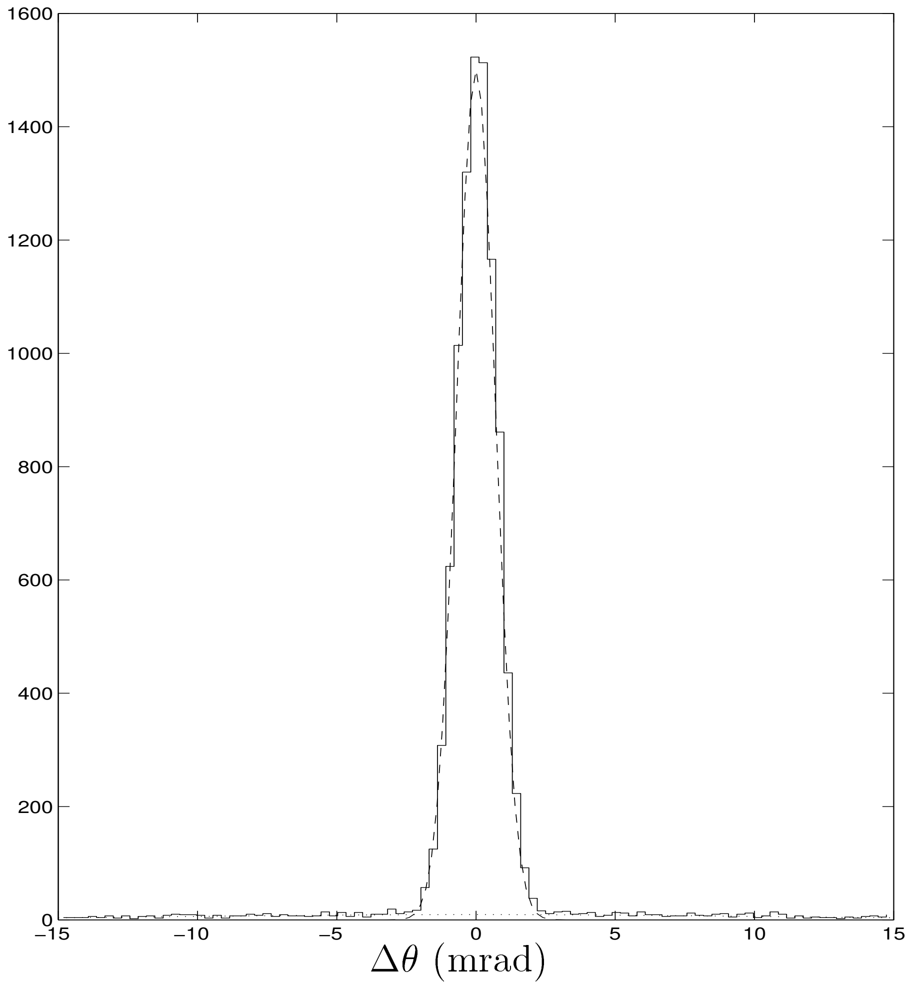

Figure 2.6: The SiDC – Pad Chamber matching distribution (histogram) together with a gaussian fit (dashed line).

Chamber of high-momentum ($p > 6$ GeV/c) π tracks identified in the two RICH detectors. This distribution is composed of two parts (see Fig. 2.6): a narrow ($\sigma \sim 0.5$ pad) one corresponding to real matching and a wide (~ 5 pads) – corresponding to fake matching. The shape of the background distribution was determined by random pointing. Then the whole matching distribution was fitted by the sum of a gaussian distribution and the background shape. Taking the Pad Chamber efficiency as the fraction of real pointing in the experimental distribution yields 91%. However, this number is clearly an under-estimation, since the π sample contains also some amount of fake tracks, and therefore the estimated number must be renormalized to the number of real π tracks in the experimental sample. Taking into account the pion sample purity, we came to a detector efficiency of at least 95%. The 5% loss is explained by the 1.5% inefficiency caused by the two spokes and several electronic modules that did not operate properly.

Hit size and double hit resolution.
The hit width (estimated as the root mean square width of the pad amplitude spatial distribution) has an average size of 0.72 pads (see Fig. 2.7), which is very close to the size empirically

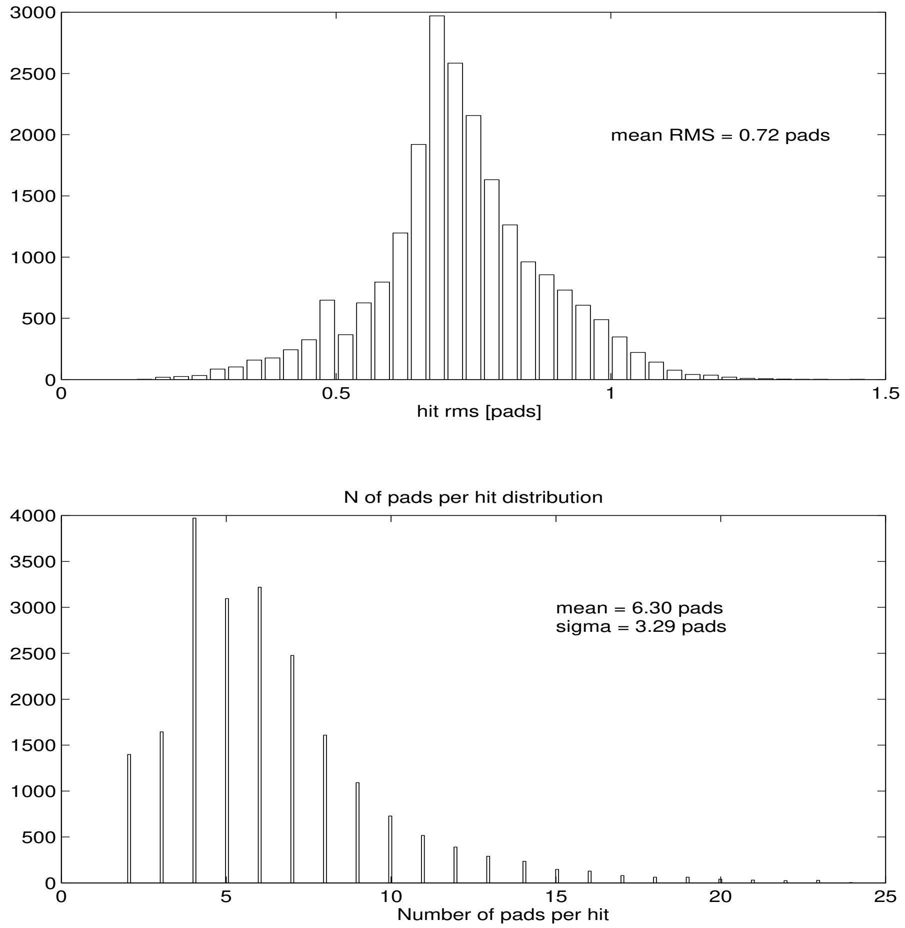

Figure 2.7: The Pad Chamber hits size distribution.

estimated for the UV-2 detector (0.67) [20], which has identical geometrical conditions. This value is in good agreement with an estimation (0.65 pad) based on the electrostatic image of a point charge at the anode plane (see ref. [26] for details), taking into account the actual pad size.

The double pulse resolution is about 1.5 pads, in good agreement with the pulse size.

2.4 On-line slow control software

The CERES slow control software is used for two general purposes:

- high voltage (HV) control;
- monitoring temperature, atmospheric pressure and gain in the UV detectors and the pad chamber.

High voltage control

The high voltage software takes control of all the gas detectors and the UV lamps used to calibrate the UV detectors, and its main purpose is to ensure a safe opration of all gas counters. It performs the following functions:

– setting voltages,
– switching the HV on and off,
– monitoring the currents of the electrodes,
– counting "overcurrent" conditions (or spark),
– sounding alarm and subsequently automatic switching off the detector if a continuous discharge occurs.

A new on-line software for the high-voltage control was developed. The software runs on a FIC-8230 (Motorola-68020 based CPU unit) in VME crate under the operating system OS9 and drives a high voltage supply (CAEN SY–127) via a VME controller (CAEN A–200).

The software is realized as 3 separate processes. All the programs were written in C with heavy use of OS9 real-time tools.

Temperature and pressure monitoring

There are two main reasons to worry about the enviromental conditions (temperature and atmospheric pressure). First, since the whole spectrometer is kept at a temperature of about 50°C, large temperature differences between different parts of the spectrometer could have severe consequences. E.g. a temperature below 43°C would cause TMAE condensation in the detectors [20] (saturated vapor of TMAE [Tetrakis (dimethylamine) ethylene] is the photo-sensitive agent of the UV detectors). In addition to that, temperature gradients cause mechanical stresses in the entrance window of UV-1 (made of CaF_2) and are capable of destroying it.

Second, to keep the spectrometer efficiency at the designed level, the gain of the UV detectors and the Pad Chamber must be constant within ± 20 %. Decreasing the gain leads to the loss of hits, while increasing it, yields massive pile-ups and excessive detector sparking. The gain at the gas detectors depends crucially on the environment, particularly on gas density, which is proportional to p/T, p being the atmospheric pressure and T the absolute temperature. So the temperature of the detectors and the atmospheric pressure (which changes more rapidly) must be monitored in order to adjust the high voltages to keep the gain constant.

The analysis of data from the UV detectors yielded an empirical formula for the gain g:

$$g = f_0 + f_1 x + f_2 x^2$$

$$x = \frac{1}{\sigma}\left(\frac{p}{T} - \frac{p_0}{T_0}\right)$$

where p is measured in mbars (1 bar = 760 mm Hg), T – is the absolute temperature, and $f_0 = 5.0 \cdot 10^5$, $f_1 = -1.0$, $f_2 = 1.0$, $\sigma = 0.05$ are empirical coefficients. p_0, T_0 are reference values: $p_0 = 1000$ mbar, $T_0 = 323K$.

The temperature is monitored by about 100 temperature probes (PT100) all around the spectrometer, and the chamber gain is assessed regularly during the run by: (i) the temperature monitoring according to the empirical formula described above, and (ii) running the data analysis software over ∼1000 events to obtain exact values. The real-time estimation of the gain given by the temperature monitoring program was always found within 10% of the exact gain value, estimated off-line by the data analysis software. If necessary, the high voltage was adjusted to maintain the gain constant to within ±20%.

A new message display software was also designed and developed. Messages coming from slow control and DAQ programs running in different VME crates (on different CPUs) were displayed in a terminal. The new software consists of the message server ("daemon") and the library of message-sending routines. An essential part of the design was creating a protocol for "handshaking" between the different programs.

2.5 Refurbishing of UV-1

The UV detectors have been operated without opening them since 1991. During the 1995 run, UV1 showed a degraded performance. The detector could not be operated at the desired gain of 2.5 10^5 without an excessive spark rate which actually limited its effective lifetime.

The detector was therefore opened for inspection after the 1995 run. All mesh electrodes, and in particular the cathodes and the multiwire plane showed some kind of a deposit. This was clearly visible under the microscope and it could be easily removed by gently brushing the electrode with a solvent.

To repair that, the following steps were taken:

- most of the mesh electrodes were replaced by spare ones (from the original production) or by new ones which were made using the tooling and procedures described in [20];

- the wire anode of the MWPC was subjected to ultrasonic cleaning. For this purpose a special bath ($90 \times 90 \times 2$ cm) of 2-mm thick aluminum was constructed. An ultrasonic generator (sonifier), Brandson-12, at a maximal acoustic power of about 130 W was used. The cleaning procedure was studied and optimized using small pieces of mesh from one of the electrodes. After each treatment the wire electrode was visually inspected under the microscope with a $\times 40$ magnification. First ethyl-alcohol was tried as cleaning solution, but much better results were obtained using isopropyl-alcohol. A treatment time of 15 minutes was found optimal.

- Finally, we also produced a new wire electrode, following the original construction procedure [20], which we kept as a spare in case that the cleaning procedure would have been ineffective.

The refurbished detector was tested during our set-up run with the proton beam and performed very well during the 1996 Pb run.

2.6 Data taking

CERES had a data taking run of 9 days during the SPS Pb beam period in the fall of 1995 and of 27 days in the fall of 1996. The data were collected with an interaction trigger corresponding to a charged-particle density $\mathrm{dN}_{ch}/\mathrm{d}\eta \geq 100$, i.e. to the top 35% (30%) of the geometrical cross section with an average multiplicity of $\langle \mathrm{dN}_{ch}/\mathrm{dy} \rangle = 220$ (250) in 1995 (1996). These averages were measured in the pseudorapidity range $\eta = 2$–3. The trigger was derived from an array of scintillator counters located downstream of the spectrometer. With an average beam intensity of 10^6 ions per burst (SPS ion burst duration is 4.8 s, out of 19.2 total cycle) we recorded to tape about 1000 events per burst. The total number of recorded events was about 10^7 in 1995 and $6 \cdot 10^7$ in 1996.

The target consisted of 8 Au disks of 25 μm thickness and 600 μm diameter, spaced by 2.8 mm between them. Such a structure keeps a large interaction rate while minimizing the amount of γ-conversions and secondary interactions. The total target thickness is limited to 200 μm, corresponding to an interaction length of 0.8%, in order to cope with the large δ-ray production by the Pb ions. The spacing between the target discs prevents from particles produced in one disc within the CERES acceptance to interact in the following discs.

Chapter 3

Data Analysis

In this chapter I describe in detail the data analysis procedure, emphasizing the approach developed for the systematic study and suppression of the combinatorial background.

3.1 Data analysis procedure: overview

The CERES data analysis is carried out in two stages. In the first stage, electron tracks are reconstructed and combined into pairs in each event, and all pairs with their relevant parameters are stored in a database for further processing (provided that the event contains at least 2 tracks with $p_t > 50$ MeV/c). The sequence of steps here is as follows:

- hit finding in the SiDC detectors and vertex reconstruction;
- event clean-up and hit finding in the two RICH detectors and in the pad chamber (PC);
- finding ring candidates in RICH-1 by performing a Hough transformation and matching the Hough peaks to SiDC hits;
- extending the SiDC – RICH-1 tracks into the pad chamber, finding PC hits in a given area around the extrapolation point;
- finding ring candidates in RICH-2 by making a Hough transformation and matching the Hough peaks to the PC hits;
- fitting rings in both RICH detectors.

The first stage gives a considerable data reduction (approximately 1 e^+e^- pair per 25 recorded events is stored in the database). It is very complicated logistically and CPU-time-consuming, since millions of events have to be processed by sophisticated pattern-recognition algorithms. For the analysis of the 1995 data, this stage was performed on the Meiko–CS2 parallel computer at the CERN CN division, using 32 processors simultaneously. For the analysis of the 1996 data (final version), the PC-farm of the CERN CN division was exploited. The off-line library was completely rewritten for this analysis from Fortran 90 to C++. The software used heavily *RW* (Rogue Wave) class library. The display software was based on *otcl* extension of the *Tk/Tcl* package and *Vogle* library. The length of CERES-written code was about 25 000 lines. The output was stored in the form of *ntuples* [27].

The second stage deals with the extraction of the signal, i.e. the invariant mass spectrum of the e^+e^- pairs. The p_t cut is raised to $p_t > 200$ MeV/c to improve the signal-to-background ratio. The softer tracks in the sample ($50 < p_t < 200$ MeV/c) are used to increase the rejection of π^0-Dalitz and γ-conversion pairs. The main steps here are as follows:

- rejection of fake tracks by applying strong ring-quality and geometrical matching cuts;
- removing misidentified high-momentum π tracks;
- identification of electron pairs from the trivial sources: – γ-conversions and π^0-Dalitz decays;
- rejection of single tracks originating from the trivial sources;
- combining the surviving tracks into pairs of unlike sign (+−) and like sign (++,−−) and extracting the desired signal by subtracting the combinatorial background (estimated by the like sign pairs) from the unlike sign pairs.

The second stage is the most critical part of the analysis, and a large fraction of this chapter is devoted to a detailed description of the procedure.

3.2 Geometrical intercalibration of the CERES spectrometer

Obviously, before starting the tracking, all five detectors (2 SiDCs, 2 RICHs and the pad chamber) must be properly intercalibrated. Since each of the 5 CERES detectors gives the particle coordinates in its own frame and units, these local coordinates must be converted into "world" coordinates to be used for tracking. Table 3.1 lists the relevant units for each detector and their corresponding world coordinates.

Detector	Local units	World coordinates
RICH	x,y of pad	θ, φ of particle propagation
SiDC	time, anode	x,y,z of particle crossing SiDC plate
PadC	x,y of pad	x,y,z of particle crossing PadC

Table 3.1: Local coordinates for different detectors and relevant world coordinates.

RICH detectors.

For the RICH detectors, let us consider first paraxial approximation, which is fairly good since the polar angles involved are smaller than 0.25 rad (we use this appoximation for clarity of presentation only; the data analysis software uses exact ray-tracing). The relation between the mirror focal length f, the particle direction angles θ, ϕ and the cartesian coordinates x, y of the ring center in the UV-detector plane is

$$x = f \operatorname{tg} \theta \cos \phi$$

$$y = f \,\mathrm{tg}\,\theta \sin\phi$$

if we assume that the detector axis coincides with the optical axis of the mirror (the UV-detector plane coincides, as mentioned before, with the focal plane of the mirror). If the detector axis is shifted by (x_o, y_o) from the optical axis, the relation is

$$x = f \,\mathrm{tg}\,\theta \cos\phi + x_o$$

$$y = f \,\mathrm{tg}\,\theta \sin\phi + y_o$$

It can be shown, that a small (several mrad) tilt of the RICH mirror is technically undistinguishable from a shift of the UV-detector axis with respect to the mirror axis. In this work I always assume the mirror axis to coincide exactly with the beam axis. This assumption has no practical consequences.

The three adjustable parameters for each RICH detector are therefore the focal length f and the offsets x_o, y_o.

Silicon Drift Chambers.
In the ideal case (detector center exactly on the beam line) the arrival time of the pulse is connected to the radius r of the hit by

$$t = t_0 + \frac{R_{out} - r}{v_{drift}}$$

and correspondingly

$$r = R_{out} - v_{drift}(t_0 - t)$$

Here the time delay t_0 and the drift velocity v_{drift} are free parameters in the sense that they are not known a priori and must be evaluated from the data[1]. t_0 depends on the hardware (like cable length) and it does not change during the running time. On the other hand, v_{drift} depends crucially on temperature and should be determined at least every 3 hours. For that, we use the difference between the minimum and maximum drift times which corresponds to a well known distance in the detector. Futhermore, t_0 varies from anode to anode, i.e.

$$t_0 = t_0(\varphi)$$

and the SiDC detector is shifted with respect to the beam axis[2]. Taking this shift into account we obtain for the world coordinates of the SiDC hit

$$x = (R_{out} - v_{drift}(t_0 - t)) \cos\varphi + x_o$$

$$y = (R_{out} - v_{drift}(t_0 - t)) \sin\varphi + y_o$$

where x_o, y_o are the coordinates of the SiDC center with respect to the beam axis.

The nearly on-axis configuration of the silicon detectors (i.e. smallness of the angles in the sense that $\sin\theta \sim \theta$) enables a robust vertex reconstruction without knowledge of the exact values of the relevant parameters. But at the same time it introduces a big uncertainty in the

[1] R_{out} is known with high accuracy, and it is therefore fixed in the software.

[2] We should also remember that a small shift of the SiDC detector in the xy plane is technically undistinguishable from the situation in which $t_0(\varphi) \sim \cos\varphi$.

local-to-world coordinate transformations, even if the actual vertex position is known from the target geometry.

Pad Chamber

Due to the large size of the PC and its large distance from the target[3], the only relevant PC free parameters are x, y shifts, that can be easily measured by a ruler.

Intercalibration

The intercalibration strategy developped in the framework of this work is as follows:
– fix the pad chamber parameters, the outer edge of the SiDCs R_{out} and the target positions from actual measurements,
– determine t_0, x_o, y_o for the SiDCs by matching with the PC,
– determine f, x_o and y_o of the RICH detectors by matching the SiDC to the RICH-1 and the PC to the RICH-2.

3.3 Electron track reconstruction

In the present analysis, we take full advantage of the external tracking detectors (the doublet of SiDC before and the pad chamber after the double RICH spectrometer) for the track reconstruction.

3.3.1 SiDC segments reconstruction

- **SiDC hit reconstruction.**
  As described in the previous chapter, the output of the SiDC spans a two dimensional space of drift time (radial position) versus anode number (azimuthal angle φ). The pixels in the $r-\varphi$ plane with a signal above a given threshold are grouped into clusters defined as the nearest-neighbor connected pixel structures. A hit is defined as the center of gravity of the cluster. Large size clusters pass through a hit splitting algorithm. This algorithm uses the characteristic shape of a single hit and tries to split the cluster into a number of subclusters, each one containing only a single hit.

- **Vertex determination.**
  The vertex of the event is reconstructed in two steps: first, matching of hits in both SiDC to tracks; second, matching of all tracks to one point in the target space. This point is defined as the vertex of the event. A detailed description of the algorithm may be found in [28].

- **Segment reconstruction**
  A segment is the best line determined by a pair of matched hits in SiDC-1 and SiDC-2 pointing to the vertex. Once the segment is reconstructed, we calculate the polar angle θ and the azimuthal angle ϕ of the particle propagation with respect to the z-axis (that coincides with the incident beam trajectory).

[3]The pad chamber tilt is negligible. If we assume the maximal deviation at the edges to be ± 0.5 mm, the corresponding tilt $\Delta\theta$ is $\Delta\theta = \pm 0.04$ mrad.

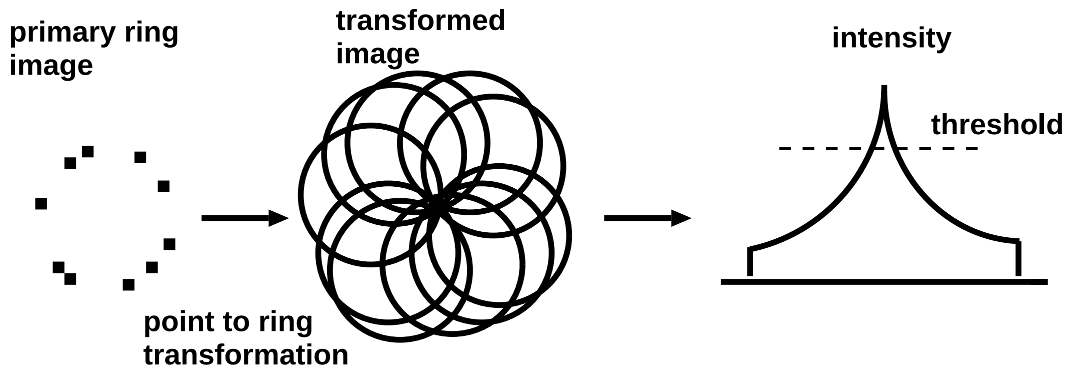

Figure 3.1: Ring candidate search by a Hough transformation.

3.3.2 Event clean-up and hit finding in the two RICH detectors and the pad chamber

The raw event data of the two RICH detectors and the pad chamber consist of the location and pulse height of each of the hit pads. The event analysis is very similar for all three detectors, and it was already described in sect. 2.3.4.

3.3.3 Ring candidates in RICH-1

The next stage of the event analysis is finding ring candidates in the whole area of RICH-1. This is done through the following steps:

– A two-stage point-to-ring Hough transformation [29] is performed. Namely, around each hit pad a ring with the nominal asymptotic radius is assigned. In the second stage the transformed image is smoothed. It exhibits therefore an intensity distribution with a pronounced maximum at the location of the ring center. The principle of the Hough technique is illustrated in Fig. 3.1.

– A ring candidate is identified as a peak in the Hough array, matched to a SiDC segment. Since the particle trajectory up to RICH-1 is a straight line, for each RICH-1 candidate, a SiDC segment is looked for within a small window. The window corresponds to some maximal (6 mrad) angular distance $\sqrt{\Delta\theta^2 + (\sin\theta \cdot \Delta\phi)^2}$ between the RICH-1 candidate and the SiDC segment;

– The algorithm requires at least two ring candidates per event, otherwise the event is discarded.

3.3.4 Tracking into the pad chamber

After passing RICH-1 the electron is deflected by the magnetic field in the azimuthal direction, clockwise or counter-clockwise according to its charge, whereas the polar angle is kept unchanged (besides a small deflection due to the focusing effect of the magnetic field). The deflection $\Delta\varphi$ between RICH-1 and PC is inversely proportional to the particle momentum p and is given by

$$p(GeV) = \frac{93mrad}{\Delta\varphi(mrad)} \tag{3.1}$$

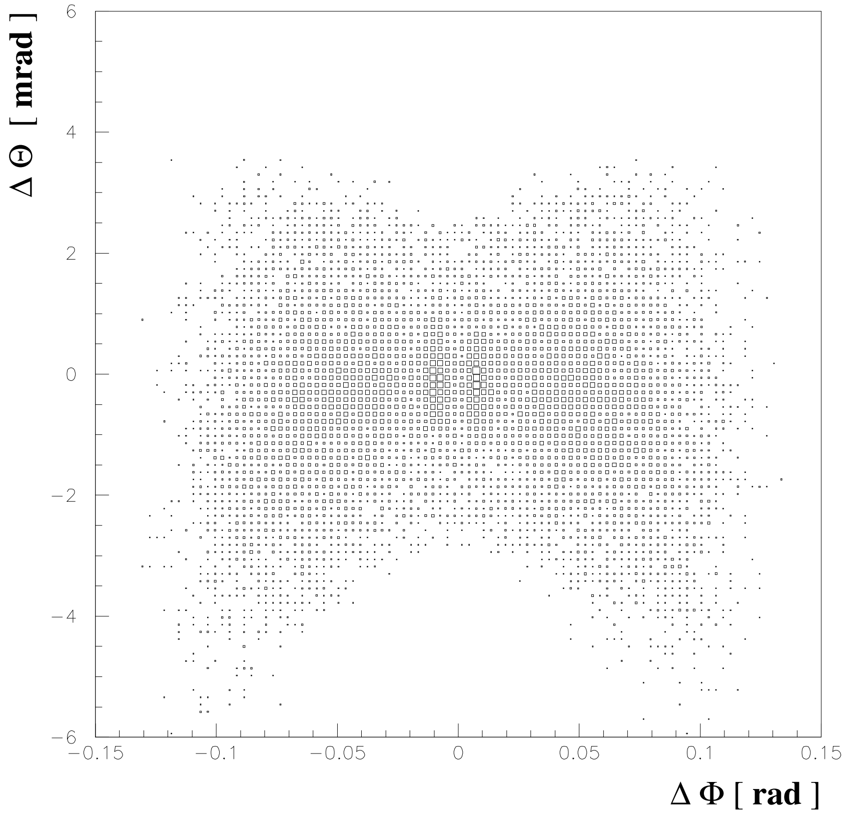

Figure 3.2: 2-dimensional distribution of polar θ and azimutal φ deviations between RICH-1 ring and pad chamber hit.

The constant in the numerator has a very weak dependence on the polar angle within the acceptance. It grows from 92 mrad to 94 mrad as θ varies from 140 mrad to 260 mrad.

In correlating a pad chamber hit to a ring candidate in RICH-1, a transverse momentum cut of p_t >50 MeV/c is applied, thus limiting the region of search of the hit location in the pad chamber in the azimuthal direction. The actual region were the hit is searched has a 'butterfly' shape when looking in polar coordinates, see Figure 3.2, where the azimuthal deflection, $\Delta\phi$, is in the abscissa and the radial shift, $\Delta\theta$, is in the ordinate. In the radial direction the region is limited by the detector resolution at the infinite momentum limit; as the momentum decreases, the searched area increases due to the multiple-scattering, producing the 'butterfly' shape.

3.3.5 Finding RICH-2 ring candidates

- A search for rings in the whole area of RICH-2 counter is done by performing a Hough transformation exactly as in RICH-1.

- For each PC hit matched to a RICH-1 candidate within the 'butterfly', a matching RICH-2 Hough peak is looked for. If there is such peak, it is marked as RICH-2 ring candidate.

At this step we have a full track with ring candidates in the two RICH detectors, matched to outer tracking detectors.

3.3.6 Ring fitting and final track identification

An electron ring fit is performed in both RICH detectors, to determine more precisely the coordinates of the ring centers. The rings are then combined into pairs. A ring in RICH-2 can have only one partner in RICH-1. In case of ambiguities the RICH-1 ring with the best θ matching is selected. A RICH-1 ring can have two RICH-2 counterparts (of different sign). This is the typical "V" pattern of γ-conversion. Then the algorithm seeks for the best matching SiDC segment for the RICH-1 ring and the best matching PC hit for SiDC – RICH-1 – RICH-2 track, finishing in this way the track identification. Tracks are combined to pairs and stored in a database for further analysis.

3.4 Combinatorial background rejection strategy

As mentioned earlier, the combinatorial background is the major problem of the measurement of low-mass electron pairs. Namely, out of every million of central Pb–Au collision events recorded during the data taking run, only about 250 of them contain an interesting e^+e^- pair (i.e. $m > 200$ MeV/c^{2}and both tracks with $p_t > 200$ MeV/c), whereas almost every event contains one e^+e^- pair from π_0-Dalitz decay or γ-conversion. In addition to that, there are fake tracks, i.e. artifacts that do not correspond to real particles traversing the spectrometer, and also high-energetic π-mesons mistakenly identified as electrons. Combining all tracks of a given event into pairs leads to a huge combinatorial background. The fully reconstructed pairs from the physical sources can be easily identified and therefore they do not contribute to this background. The combinatorial background is due to the large amount of partially reconstructed γ-conversions and π^0-Dalitz decays, where only one track has been reconstructed whereas the other one was lost – mainly due to the p_t-cut and finite reconstruction efficiency. The magnetic field between the RICH detectors deflects the low-momentum particles such that they can not be tracked through the magnetic field, so the cut $p_t > 50$ MeV/c (sect. 3.1) is essentially hardware-imposed .

The problem of optimizing the background rejection strategy may be formalized as follows. We have a sample consisting of signal and background points in a multi-dimensional parameter space (η_1, η_2, ...). Each point is a dielectron pair, and the parameters η are e.g. ring quality, matchings, momentum etc. The parameters of the signal and of the background have different distributions, and thus the signal can be (partially) separated by applying cuts in the multi-dimensional space ($\eta_1 < \eta_{1cut}$, $\eta_2 < \eta_{2cut}$ etc). Any statistical characteristics of the reduced sample (e.g. the signal, signal-to-background ratio, background-free equivalent signal etc.) can be expressed as function of the cut values: $H(\eta_{1cut}, \eta_{2cut}, ...)$ and one can find optimal values of $(\eta^{opt}_{1cut}, \eta^{opt}_{2cut}, ...)$ just by looking for the maximum of the function $H(\eta_1, \eta_2, ...)$. It is clear that placing too loose cuts leaves a lot of background, while placing too tight cuts leads to serious vetoing of the signal. Some trade-off must be found to achieve the best spectrum accuracy.

In the previous CERES data analysis (refs. [18] and [19]) the cuts were adjusted on the sample of open pairs (i.e. $m > 200$ MeV/c^2) themselves to maximize the signal and the signal-to-background (S/B) ratio. Although principally correct for large data samples, this method is inadequate for limited statistics and poor S/B ratio since it can create a "signal" out of statistical fluctuations. Intuitively one can estimate the expected bias as $\sqrt{U_i + L_i}$, where U_i and L_i are the initial numbers of unlike-sign and like-sign e^+e^- pairs, respectively. This effect can be demonstrated on a simple model, described in Appendix A. It is therefore absolutely necessary to develop objective tools and criteria to fix the values of the cuts.

In the present analysis the rejection is done in the following order:

- fake tracks are removed by applying matching and ring quality cuts;
- pion tracks are removed by applying a high momentum cut;
- tracks belonging to fully reconstructed γ-conversion pairs are removed from the sample;
- fully reconstructed π^0-Dalitz pairs are kept in the sample, but their tracks are not used in further pairing with other tracks;
- partially reconstructed ("one-leg") γ-conversion pairs are removed;
- partially reconstructed ("one-leg") π^0-Dalitz pairs are removed;
- all tracks with $p_t < 200$ MeV/c are removed. It should be stressed that though this cut is one of the strongest in the signal extraction chain, it is applied after all the other cuts, in order to enable identification of pairs of trivial origin with maximal efficiency. The influence of this cut on the CERES pair acceptance is clearly illustrated in Fig. 3.3.

In the course of this work we made a major effort to systematically study the effect of the applied cuts. The emphasis was to ensure that all the applied cuts have solid grounds, and that their values are chosen according to objective criteria.

1. Quality and matching cuts were adjusted using an enriched sample of genuine tracks and an enriched sample of fake tracks. Both samples were obtained from the data base of the first stage of data processing (see sect. 3.1) and are totally unbiased.

2. The physics cuts, for the rejection of tracks from trivial pairs, were studied and fixed on a sample of pure γ-conversions and of pure π^0-Dalitzes (i.e. m<130 MeV and opening angle θ <30 mrad). The two samples are rather large (about 50 000 pairs each) thereby reducing statistical fluctuation effects, and furthermore they allow an unbiased adjustment of all cuts:
   – For the rejection of γ-conversions, the cut values were adjusted by maximizing the S/B ratio where the signal S is the yield of π^0-Dalitzes and the background B is the yield of the pure conversion sample.
   – For the rejection of π^0-Dalitz decays, we do the opposite. The cuts are adjusted by maximizing the S/B ratio where the signal S is the yield of the pure γ-conversion sample whereas the background B is the yield of π^0-Dalitzes.

3. The set of cuts defined in 1. and 2. were then applied to the full data set to extract the signal of low-mass e^+e^- pairs with $m > 200$ MeV/c^2.

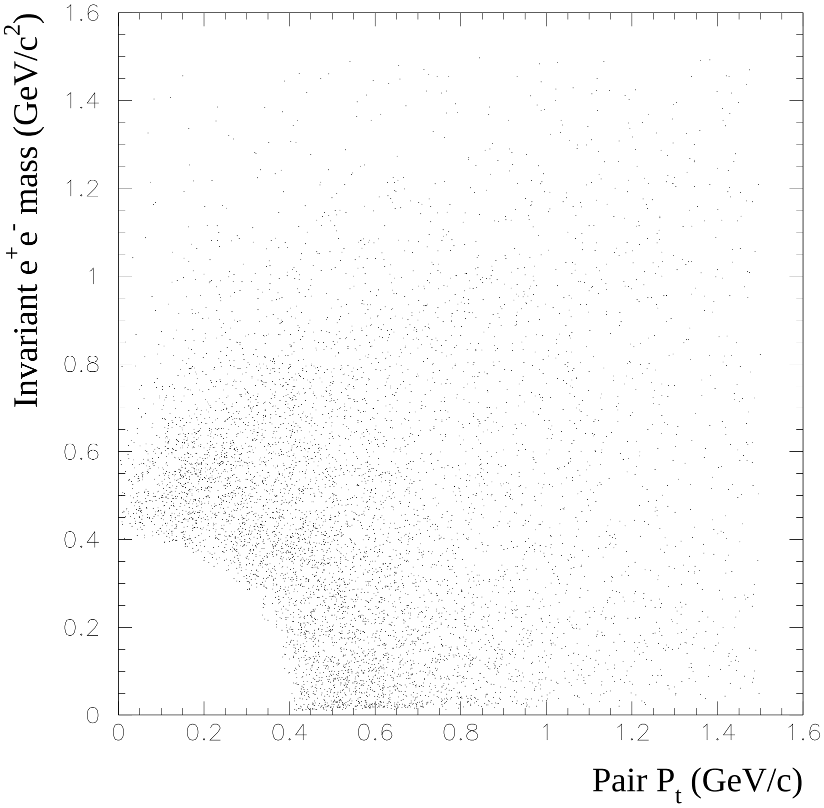

Figure 3.3: Effect of the single track p_t-cut ($p_t > 200$ MeV/c) on the CERES acceptance in e^+e^- pair p_t vs. invariant mass.

4. Final adjustment of cuts: the above procedure, like any other procedure, does not define sharply the values of the cuts but rather fixes them within a narrow band of the order of ± 10-15%. To avoid any "hand" adjustment of the cuts within that range, we used a random procedure of varying the cuts including all cuts simultaneously, the quality, matching and physics cuts (see 3.6.1 for details).

3.5 Rejection algoritm

Below we describe the procedure of choosing the relevant parameters and fixing the cut values for all the steps.

3.5.1 Fake tracks

Since an electron track is identified essentially by the two RICH rings, it is convenient to classify the fake tracks in 4 categories. Namely, each ring may be real (i.e. result of electron (positron) traversing the radiator) or fake (i.e. a pattern recognition artifact – random ring-like combination of hits). A fake track consisting of two real rings is possible if these rings belong to different (probably low-energy) tracks. The relevant criteria for the decision fake/real are ring quality and geometrical matching between different parts of the track. We summarize the different cases in table 3.2.

Track type	R1 quality	R2 quality	SiDC–RICH-1 matching	RICH-1 – 2 matching	PadC matching
fake R1, fake R2	bad	bad	bad	bad	bad
real R1, fake R2	good	bad	good	bad	bad
fake R1, real R2	bad	good	bad	bad	bad
real R1, real R2	good	good	good	bad	bad

Table 3.2: Different combinations giving fake tracks and their features.

The immediate consequence of this classification is that RICH-1 – 2 and pad chamber matchings provide the most powerful means to reject fake tracks, since for all types of fake tracks these two matchings are bad (determined by random hits). RICH-2 ring quality criteria are used to further reject tracks, composed of a real SiDC–RICH-1 segment and a fake RICH-2 ring. Finally, we use the SiDC–RICH-1 matching, and also RICH-1 ring quality, to reject tracks, composed of a fake SiDC–RICH segment.

We used the following rejection cuts to reject fake tracks.

- **RICH-1 – 2 and PC matching**

  Fig. 3.4 shows the matching distribution in the pad chamber, i.e. distribution of the deviation Δr_{PC} from the track predictor (based on SiDC and RICH information) to the actual pad chamber hit. The circles show the experimental distribution of deviations for all tracks. The dashed and dash-dotted lines show the distributions of real and fake tracks respectively. The shapes of the latter were obtained from a sample of real (fake) tracks defined by a good (bad) matching in RICH-1 – 2 and high (low) Hough amplitude (see sect. 3.3.3) of RICH rings. The solid line is a fit of the experimental distribution by the sum of the two shapes – of real and of fake tracks. One sees for example that cutting at 1.2 pad units will eliminate 33% of the fake tracks, while sacrificing only 6% of the real tracks.

  Tracks with higher momentum have better matching due to less multiple scattering. So a track with a large deviation Δr_{PC} is more likely to be fake, if its momentum is higher. Therefore we made the cut dependent directly on the momentum-dependent mean deviation $\overline{\Delta r_{PC}(p)}$: the track is discarded, if $\Delta r_{PC} > n_{PC} \cdot \overline{\Delta r_{PC}(p)}$, where n_{PC} is an adjustable parameter.

  A similar procedure was applied to RICH-1 – 2 matching. The mean polar angle difference $\overline{\Delta\theta_{RICH}}$ between rings in RICH-1 and RICH-2 is momentum-dependent, and the track is discarded if $\Delta\theta_{RICH} > n_{RICH} \cdot \overline{\Delta\theta_{RICH}}$.

  Finally, since each track has either good matching in RICH and PC, or bad matching in both, we united the two cuts into one. In other words, we made the cut not rectangular,

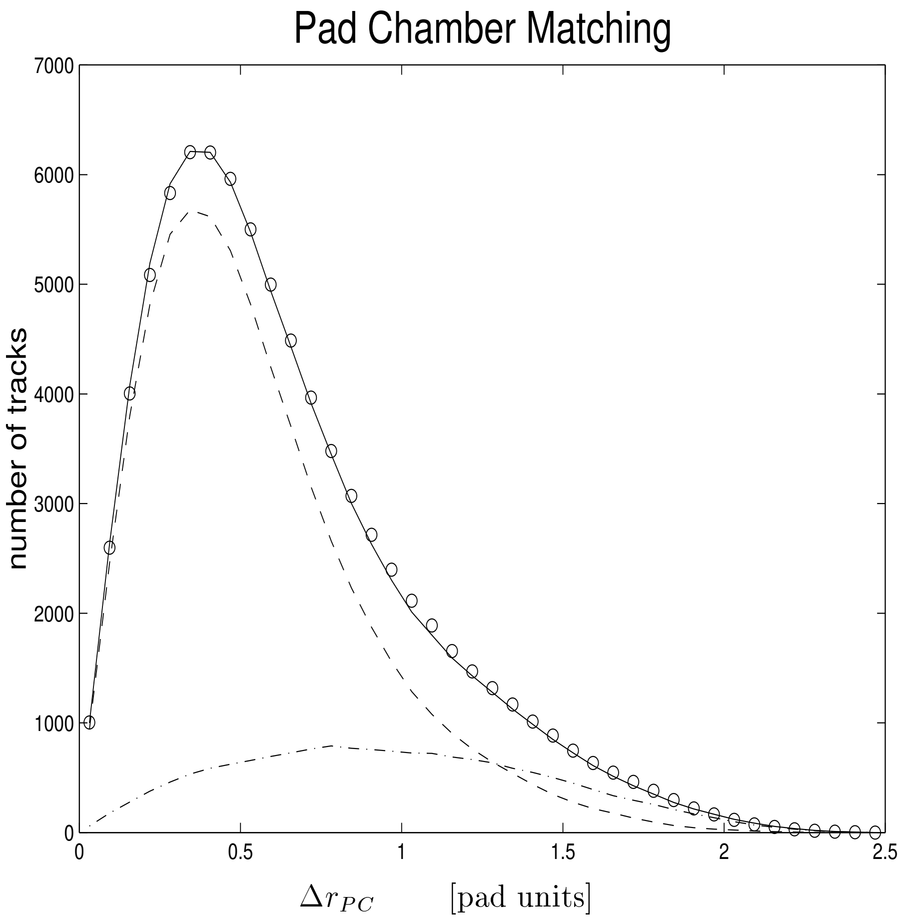

Figure 3.4: Hit – predictor distance in the pad chamber for all (circles), real (dashed line) and fake (dash-dotted line) tracks. The solid line is a fit of experimental distributions by the sum of distributions of real (dashed line) and fake (dash-dotted) tracks.

but circular in the two-dimensional space Δr_{PC} – $\Delta\theta_{RICH}$. The rejection criteria we use is

$$\frac{\Delta r_{PC}^2}{(n_{PC} \cdot \overline{\Delta r_{PC}})^2} + \frac{\Delta\theta_{RICH}^2}{(n_{RICH} \cdot \overline{\Delta\theta_{RICH}})^2} > 1$$

n_{PC} and n_{RICH} are chosen so that each individual cut rejects not more than 2% of real tracks. We used two sets of values for n_{RICH} and n_{PC}. If one of the two RICH rings has low Hough amplitude, indicating a high probability that the ring is fake, then the matching condition was more strict. The actual values were as follows:
for Hough amplitudes $HA_1 > 600$, $HA_2 > 900$ $n_{RICH} = 2.67$ and $n_{PC} = 4.0$;
for Hough amplitudes $HA_1 < 600$ or $HA_2 < 900$ $n_{RICH} = 1.87$ and $n_{PC} = 2.8$.

- **SiDC – RICH matching**
  The rejection criteria is

$$\frac{\Delta\theta_{S-R}^2}{\Delta\Theta^2} + \frac{\Delta\phi_{S-R}^2}{\Delta\Phi^2} > 1$$

where $\Delta\theta_{S-R}, \Delta\phi_{S-R}$ are polar and azimutal deviations between the RICH-1 ring centers

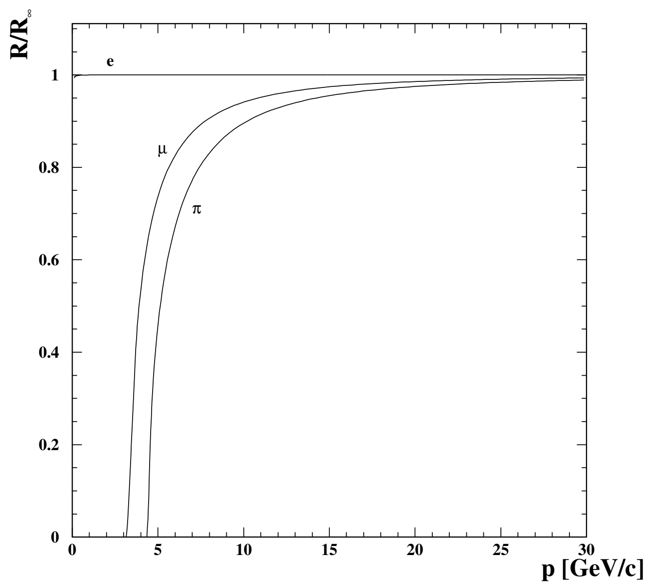

Figure 3.5: Cherenkov ring radius for electron, muon and pion as a function of the particle's momentum (normalized to the asymptotic radius) for CH_4 ($\gamma_{th} = 32$).

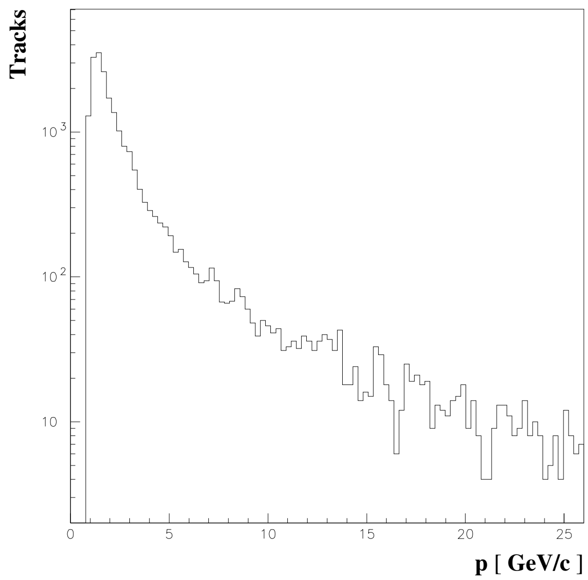

Figure 3.6: Momentum Distribution of identified electrons.

and the SiDC segments, and $\Delta\Theta, \Delta\Phi$ are the cut values. The choice of $\Delta\Theta, \Delta\Phi$ was dictated by the condition not to loose more than $\sim$2% of real tracks.

- **SiDC-1–2 matching – quality of SiDC segment**
  There is a probability that the SiDC segment of the found track is fake, i.e. the RICH-1 ring has no SiDC matching (this is for example the case for a late conversion). In order to get rid of such tracks, the track is discarded if $\Delta\theta_{SiDC1-2}$ exceeds a cut value of about 1.5 mrad. This value is dictated by preserving 99% of real tracks.

3.5.2 Rejection of pion tracks

The RICH radiators of the CERES spectrometer are filled with CH_4 at atmospheric pressure which has $\gamma_{th} \sim 32$. Therefore pions with $p < 4.5$ GeV/c, the momentum threshold for Cherenkov light emission by a pion, are not seen by the RICH detector. Higher momentum pions are easily recognized by their small ring radius.

$$\frac{R}{R_\infty} = \sqrt{1 - \gamma_{th}^2 \frac{m^2}{p^2 + m^2}} \tag{3.2}$$

This pion rejection can effectively be done for pions that produce rings with radius < 95% of the asymptotic ring radius R_∞, i.e. if their momentum $p \leq 14$ GeV/c (see Fig. 3.5). This ensures a pion rejection by about 4 orders of magnitude. Pions with $p \geq 14$ GeV/c produce rings which technically cannot be distinguished from the electron rings. In fact, from the point

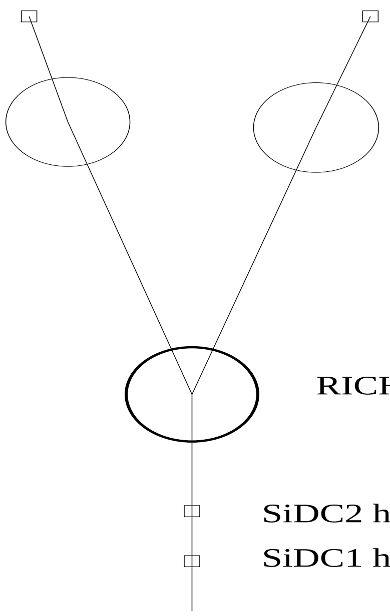

Figure 3.7: The typical pattern of a fully reconstructed target conversion.

of view of physical information these high momentum tracks are unreliable due to their very poor momentum resolution.

Fig. 3.6 shows the momentum distribution of all tracks identified as electrons. One can see that the low-energy tracks ($p \leq 9$ GeV/c) are well described by an exponential distribution. Then there is a high momentum tail which accounts for a very small fraction of all tracks (at the 1% level) which results from the big uncertainty in the momentum resolution of the CERES spectrometer that decreases at higher momenta. These high momentum tracks were not used in the analysis by rejecting all tracks with $p > 9$ GeV/c. The effect of this cut is in any case very minor.

3.5.3 Conversions

A fully reconstructed conversion pair is easily identified by its characteristic "V" pattern: the pair has a nearly-zero opening angle giving rise to two overlapping rings in RICH-1 (Fig. 3.7), which are opened by the magnetic field producing two distinct rings in RICH-2. The tracks belonging to such pairs are removed from the sample.

The rejection of a partially reconstructed ("one-leg") conversion is more elaborate. In this case one of the two tracks was not found, either because of inefficiency of the pattern recognition or because of the 50 MeV/c p_t cut. We identify them by their typical features.

All of them have a double ring in RICH-1. However, since the distribution of typical ring parameters (number of hits, sum amplitude, Hough amplitude) is rather wide, the distinction between single and double ring is limited. In order to further identify and reject conversions tracks, we exploit the SiDC information and we classify them according to the place where the conversion occurs, namely:
– target conversions

– SiDC-1 conversions
– SiDC-2 conversions
– late conversions

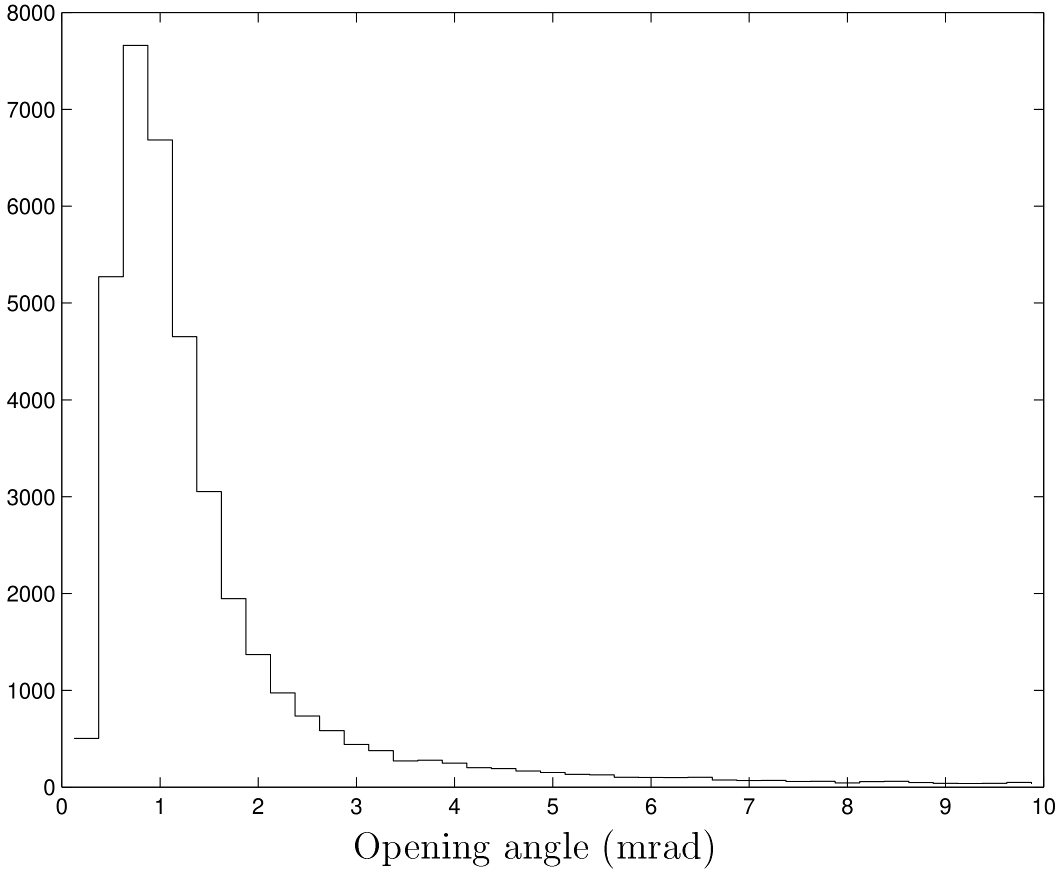

Figure 3.8: Opening angle distribution of γ-conversions e^+e^- pairs. At least one leg with $p_t > 200$ MeV/c is required. Generated by the Monte-Carlo event generator of sect. 3.8.

Target Conversions.
The opening angle distribution of conversion pairs is shown in Fig. 3.8. The double-hit resolution in both SiDCs is about 2.5 mrad. Therefore about 90% of the target conversions lead to unresolved hits in the silicon chambers, i.e. to a double hit amplitude in both SiDCs. Such tracks are effectively rejected by applying a cut on the hit amplitude of both silicon detectors. Technically, such rejection is done in the first stage of the data analysis, so that target conversions with unresolved hits are heavily suppressed in the database.

Other target conversions with larger opening angles, result in resolved hits in the silicon detectors and therefore the pattern consists of a regular track together with a close SiDC segment.

To reject the target conversions, we used therefore the following cuts.

- **Restricted cut on double energy deposition in both SiDC**
  The track was discarded if in addition to high "brightness" of the RICH-1 ring (Hough

amplitude $HA > C_{HA1}$) both SiDC amplitudes exceed cut values $a_{SiDC1} > C_1$, $a_{SiDC2} > C2$.

- The track is discarded also if it has high SiDC-1 amplitude and high RICH-1 ring brightness $HA > C_{HA2}$.

- **Close SiDC track** The track is discarded if it has a partner closer than a cut distance: $r_{to\,close\,track} < r_{min}$.

<u>**SiDC-1 Conversions.**</u>
γ-conversions originating in the SiDC-1 detector are always characterized by a double energy deposition in SiDC-2, since the distance between the two detectors (15 mm) is not enough to get enough separation of the two tracks which have typical opening angles of up to 3 – 4 mrad (see Fig. 3.8). Since the γ-conversion can occur at any depth within the wafer, the hit in SiDC-1 will have an amplitude ranging from zero up to the typical values of a double hit amplitude with an almost flat shape (see App. B; Fig. B.1 shows the result of a calculation of the energy deposition spectrum according to a formula derived there). Fig. 3.9 shows the experimental distributions of SiDC-1 amplitudes of reconstructed V-tracks. The shape is very well explained by the contributions from the following sources: double hit amplitude (unresolved double hit) from target conversions (dash-dotted line), single hit amplitude (resolved hits) from target conversions (dotted line) and convoluted double amplitude from SiDC-1 conversions (dashed line). The relative strength of the contributions enables to estimate the ratio of unresolved-to-resolved cases of target conversions as 10:1, which is in good agreement with the ratio, estimated above from the opening angle distrubution and the SiDC double hit resolution.

The rejection of SiDC-1 conversions was done as follows.

- **High SiDC-2 amplitude**
  The track is discarded if it has high SiDC-2 amplitude $a_{SiDC2} > C_2'$ and high RICH-1 ring brightness $HA > C_{HA2}'$.

- **Low SiDC-1 amplitude**
  The track is discarded if it has low SiDC-1 amplitude $a_{SiDC1} < C_1''$ and high RICH-1 ring brightness $HA > C_{HA2}''$.

<u>**SiDC-2 and late conversions**</u> are effectively suppresed by the tracking scheme since there is no matching hit in SiDC-1.

3.5.4 π^0-Dalitz pairs

A fully reconstructed π^0-Dalitz pair is easily identified by its characteristic pattern (see Fig. 3.10). The pair has a small opening angle giving rise to two intersecting rings in RICH-1, which are opened by the magnetic field producing two separated rings in RICH-2 and of course it has an invariant mass $m < m_\pi$. Such pairs are kept in the sample, but their tracks are not used in any further pairing with other tracks. Note also that some of the π^0-Dalitz pairs with very small opening angle produce the same pattern as γ-conversions, and are removed at an earlier stage.

Partially reconstructed π^0-Dalitz pairs are the main remaining source of the combinatorial background. The rejection of these tracks is the most difficult one. In this case, like in the

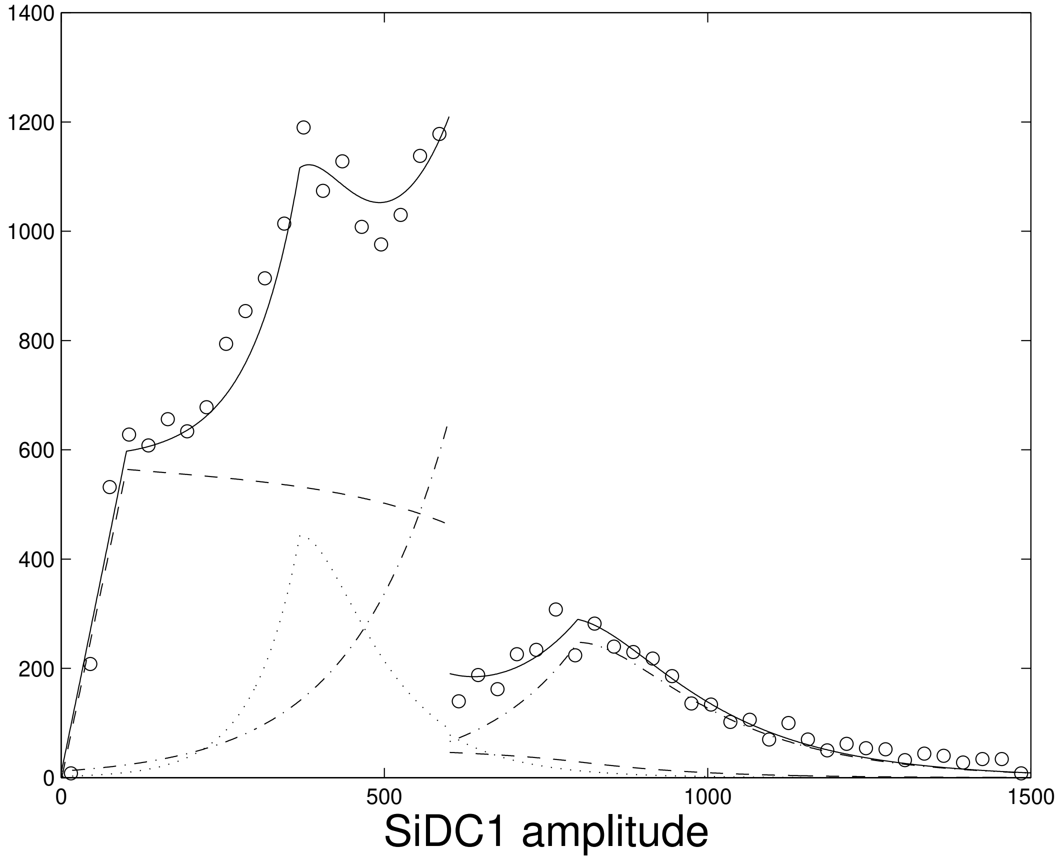

Figure 3.9: Experimental distributions of SiDC-1 amplitudes of reconstructed V-tracks, together with fit by sum of single (dotted), double(dash-dotted) and convoluted double (dashed) hit shapes. The discontinuity at a=600 is due to the cut applied at the DST production stage, which suppresses considerably the double hit component.

case of γ-conversions, one of the two tracks was not found, either because of inefficiency of the pattern recognition or because of the 50 MeV/c p_t cut. We identify them by their typical features: small distance to the next closest ring in UV-1, with fair quality and with good matching to the SiDC telescope. In our analysis, a cut of 35 mrad on this distance was applied. The main reason for choosing this value was to ease comparison with previous CERES data.

3.5.5 Summary

Table 3.3 summarizes the criteria enabling diagnostics of the different sources of background tracks from physics origin ($\pi^{\pm}$, π^0-Dalitz decays, γ-conversions).

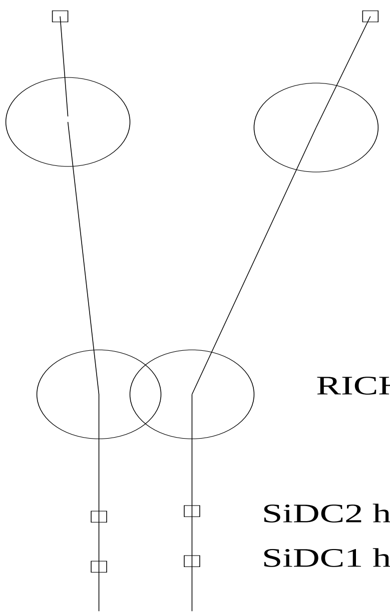

Figure 3.10: The typical pattern of a reconstructed π^0-Dalitz decay.

Track type	Cut
Pions	High momentum
π^0-Dalitz	Close RICH1 ring
γ-conversion	double RICH1 ring amplitude
	double amplitude in both SiDC
	OR close SiDC track
	OR double amplitude in SiDC2 and LOW in SiDC1

Table 3.3: Different physical tracks and their features.

3.6 Signal determination

3.6.1 Signal extraction

Once the rejection cuts are adjusted, they are applied to the whole data set in order to extract the signal. All tracks with $p_t > 200$ MeV/c surviving the cuts give rise to an unlike (e^+e^-) pair sample and a like-sign (e^+e^+ and e^-e^-) pair sample.

The residual combinatorial background in the e^+e^- sample is assumed to be equal to the total yield of like-sign pairs, defined as twice the geometrical mean of the number of like-sign pairs $N_{e^+e^+}$ and $N_{e^-e^-}$, i.e. $B = 2\ (N_{e^+e^+}\ N_{e^-e^-})^{1/2}$. For a discussion on this assumption see App. C. The pair signal S is then obtained by subtracting the like-sign contribution from the unlike-sign pairs as $S = N_{e^+e^-} - B$.

In order to reduce statistical bin-to-bin fluctuations in the background spectrum, a smooth like-sign spectrum was created from a large sample of tracks which are generated randomly according to the measured p_t, θ and ϕ distributions of tracks from like-sign pairs. By this

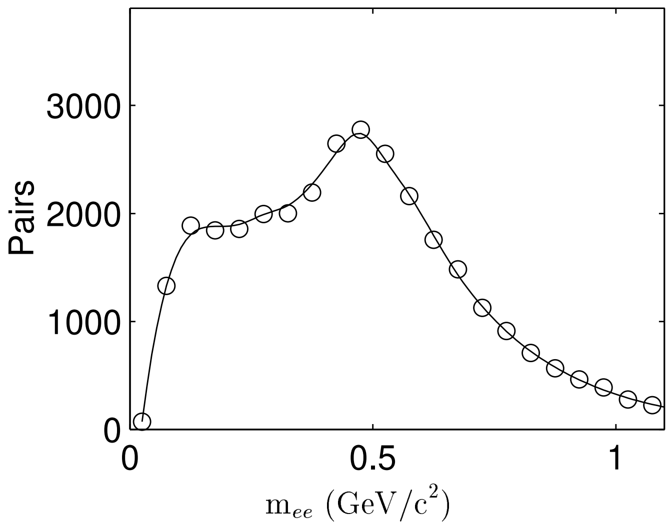

Figure 3.11: The experimental (circles) and smoothed (line) background for the 1996 data set. The smoothed one was used for all the results presented in Chap. 4.

technique, an excellent description of the like-sign mass, p_t and opening angle distributions is achieved. Fig. 3.11 shows the experimental (dots) and smoothed (line) background for the 1996 data set. With this procedure, the statistical error in the bin-to-bin signal S is reduced to $\Delta S = \Delta N_{\mathrm{e^+e^-}} = \sqrt{N_{\mathrm{e^+e^-}}}$, since the smooth background can be evaluated with practically no statistical error.

As described in detail in the previous section, the various cuts were adjusted using unbiased samples of tracks, fully reconstructed conversions and fully reconstructed π^0-Dalitz decays. However, this procedure, like any other procedure, does not define sharply the values of the cuts but rather fixes them within a narrow band of reasonable values. To avoid any "hand" adjustment of these cuts within that range, we used a random procedure of varying all cuts simultaneously, the quality, matching and physics cuts.

For reasons of speed and practicality the database was compressed by a factor of $\sim$12. This was achieved by rejecting pairs containing tracks of trivial origin, i.e. we first identified the trivial unlike pairs with opening angle below 50 mrad and invariant mass below 150 MeV. If a pair contains a track, previously identified as trivial, the pair is rejected. No real/fake track discrimination was done at this stage. We then applied the 200 MeV p_t cut. The compressed database was then subject to the set of cuts.

We made 1000 different filterings of the compressed database, each one with the same selection algorithm but with different cut values. The cut values were varied randomly (and uniformly) within the range $\pm$25% of the values determined previously. For each set of cuts, the pair reconstruction efficiency was calculated.

The results of this random walk are shown in Fig. 3.12, showing the magnitude of the signal S, the pair reconstruction efficiency E and the combinatorial background B. The magnitude of the signal varies by more than a factor of two. However, there is a correlation between the signal and the pair reconstruction efficiency E (as seen in the 2-dim plot of S vs. E) and as a consequence the distribution of the real signal, S/E, is somewhat narrower.

For the final analysis, we took the set of the cuts corresponding to the peak of the distribution

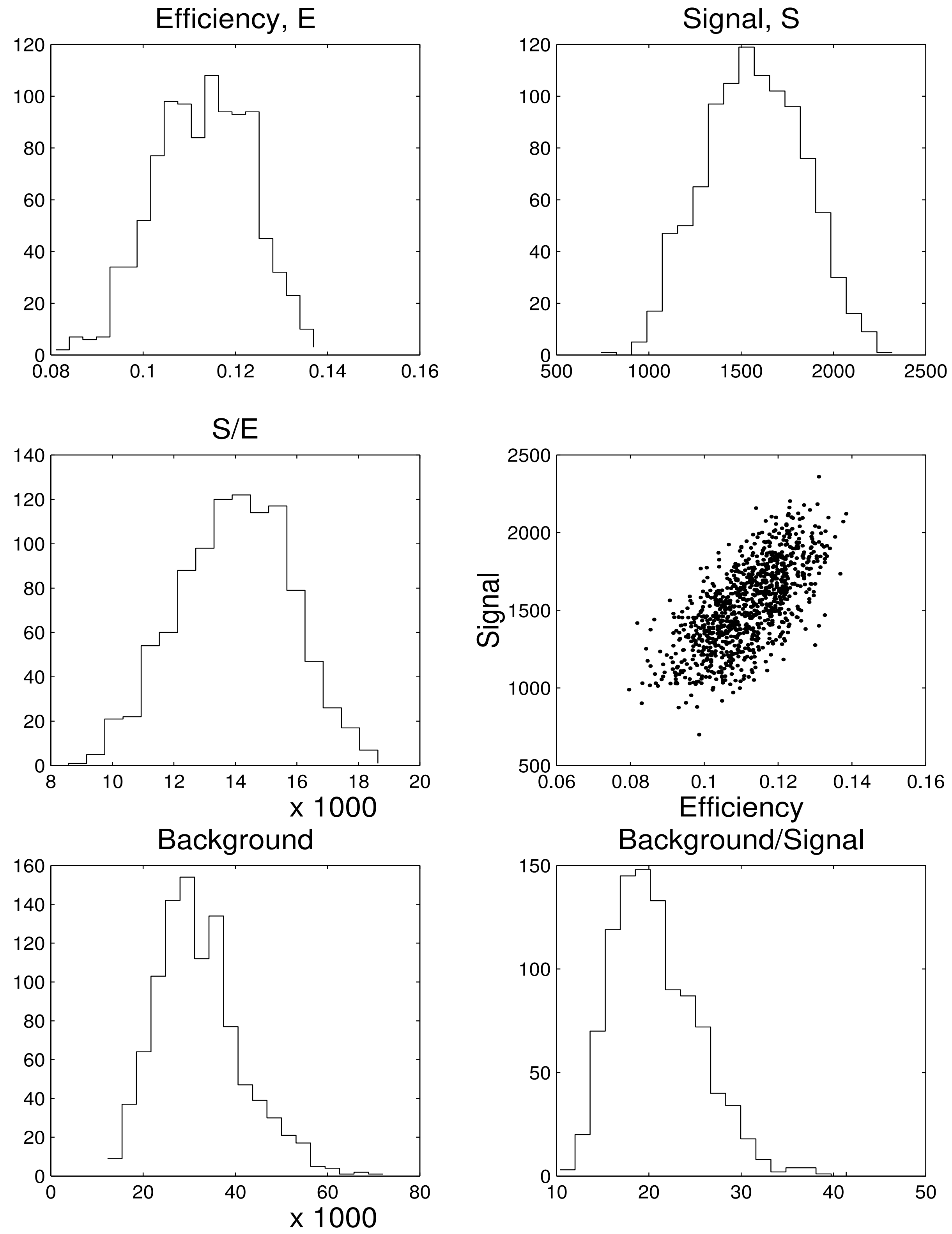

Figure 3.12: Effects of randomly varying all cuts within ± 25% of the selected cut values. Each point in the Signal vs. Efficiency graph represents one set of rejection cuts, a total of 1000 different sets was used.

of S/E.

3.6.2 Pair reconstruction efficiency

The rejection cuts described in sect. 3.4 reduce considerably the combinatorial background but they also reduce of the number of reconstructed pairs. However, the overall improvement of the signal to background (S/B) ratio is more than one order of magnitude.

For an absolute determination of the e^+e^- pair production yield, the results have to be corrected for the pair reconstruction efficiency resulting from the whole analysis chain, including pattern recognition and the sequence of rejection steps. The pair reconstruction efficiency was studied

- using fully reconstructed π^0-Dalitz pairs for which a large sample with a good signal-to-background ratio can be easily obtained.
- using a Monte-Carlo method.

Reconstruction efficiency study using π^0-Dalitz pairs.
The total number of π^0-Dalitz pairs ($n^{tot}_{\pi^0}$) collected during the data taking run is

$$n^{tot}_{\pi^0} = N_{ev} \cdot X \cdot Y^{ee}_{\pi^0}$$

where N_{ev} is the total number of valid recorded events, X – the average charged particle multiplicity, and $Y^{ee}_{\pi^0}$ – yield of π^0-Dalitz pairs per charged particle in the CERES acceptance. The number of identified π^0-Dalitz pairs is therefore

$$n_{\pi^0} = n^{tot}_{\pi^0} \cdot \epsilon$$

where ϵ is the π^0-Dalitz pair reconstruction efficiency. For the efficiency ϵ we thus get

$$\epsilon = \frac{n_{\pi^0}}{N_{trig} \cdot X \cdot Y^{ee}_{\pi^0}}$$

Actually, we have no possibility to differentiate between π^0-Dalitz pairs and other e^+e^-pairs with invariant mass below $\sim$ 200 MeV/c^2 (the main additional source of e^+e^- in this mass region – on the 10% level – is η-Dalitz decay). Thus to estimate the reconstruction efficiency we use the total number of measured e^+e^- pairs with $m <$ 200 MeV/c^2 instead of n_{π^0} and the total yield of dielectron pairs with invariant mass $m_{ee} <$ 200 MeV/c^2 instead of $Y^{ee}_{\pi^0}$. The yield was calculated using the CERES event generator (see sect. 3.8). After applying the cuts $p_t >$ 200 MeV/c on each track and opening angle $\theta_{open} >$ 35 mrad, this yield is found to be $8.8 \cdot 10^{-6}$ e^+e^- pairs per charged particle.

Reconstruction efficiency study using a Monte-Carlo method.
The following steps were performed.

- The CERES event generator (see sect. 3.8 below) was used to produce a large number ($\sim 10^5$) of dielectron pairs of all known physical sources ($\rho^0 \rightarrow e^+e^-$, $\omega \rightarrow e^+e^-$, $\phi \rightarrow e^+e^-$, $\pi^0 \rightarrow e^+e^-\gamma$, $\eta \rightarrow e^+e^-\gamma$, $\eta\prime \rightarrow e^+e^-\gamma$, $\omega \rightarrow e^+e^-\pi^0$). The cuts $p_t >$ 200 MeV/c on each track and opening angle $\theta_{open} >$ 35 mrad were applied, as well as the geometrical acceptance cuts.

- The GEANT software was used to simulate the passage of these particles (electrons and positrons) through the CERES spectrometer and to generate the spectrometer response.
- This simulated spectrometer response was overlayed on genuine raw events.
- The first stage of the data analysis (see sect. 3.1) was performed on this data.
- Finally, we applied our rejection cuts to the results of the first stage processing.

The pair reconstruction efficiency was found as the ratio of number of Monte-Carlo pairs that "survived" the whole analysis chain, to the number of initially "implanted" Monte-Carlo pairs.

Both methods are in very good agreement with each other. The results using the Monte-Carlo method (curve), and the sample of π^0 Dalitz pairs (circles), are shown in Fig. 3.13. The final pair reconstruction efficiency is about 11.8%. No significant mass dependence of the efficiency is observed. The reconstruction efficiency strongly depends on the event multiplicity, decreasing from 23% at low $dN_{ch}/d\eta$ to 6% at high $dN_{ch}/d\eta$.

3.7 Absolute normalization of the data

Following previous CERES results, we normalize the data to represent the pair production probability per charged particle within the CERES rapidity acceptance ($2.1 < \eta < 2.65$):

$$\frac{d^2 n_{e^+e^-}/d\eta dm}{dN_{ch}/d\eta} = \frac{1}{N_{events} \cdot \ < dN_{ch}/d\eta > \cdot \Delta\eta} \sum \frac{1}{\epsilon_i} \tag{3.3}$$

where,
N_{events} is the total number of analyzed events, which was $42.17 \cdot 10^6$ in 1996 ($\sim 9 \cdot 10^6$ in 1995),
ϵ_i is the event by event pair reconstruction efficiency of the off-line analysis,
$\Delta\eta = 0.55$ is the CERES fiducial acceptance,
$< dN_{ch}/d\eta >$ is the average charged particle rapidity distribution per unit of rapidity at the CERES acceptance. This number is trigger-dependent and in the 1996 Pb–Au run it was measured to be $< dN_{ch}/d\eta >= 250$ (and $< dN_{ch}/d\eta >= 220$ in 1995).

This is a convenient way to normalize the data, allowing a simple comparison between different collision systems. In the absence of new physics, an A–A collision can be considered as a mere superposition of nucleon-nucleon collisions. This implies that the particle production ratios remain constant from p–p to p–A and A–A collisions, or in other words that the e^+e^- pair production probability normalized to the particle density should be independent of the collision system:

$$\left(\frac{dN_{ee}/dy}{dN_{ch}/dy} \right)_{pp} = \left(\frac{dN_{ee}/dy}{dN_{ch}/dy} \right)_{pA} = \left(\frac{dN_{ee}/dy}{dN_{ch}/dy} \right)_{AA} \tag{3.4}$$

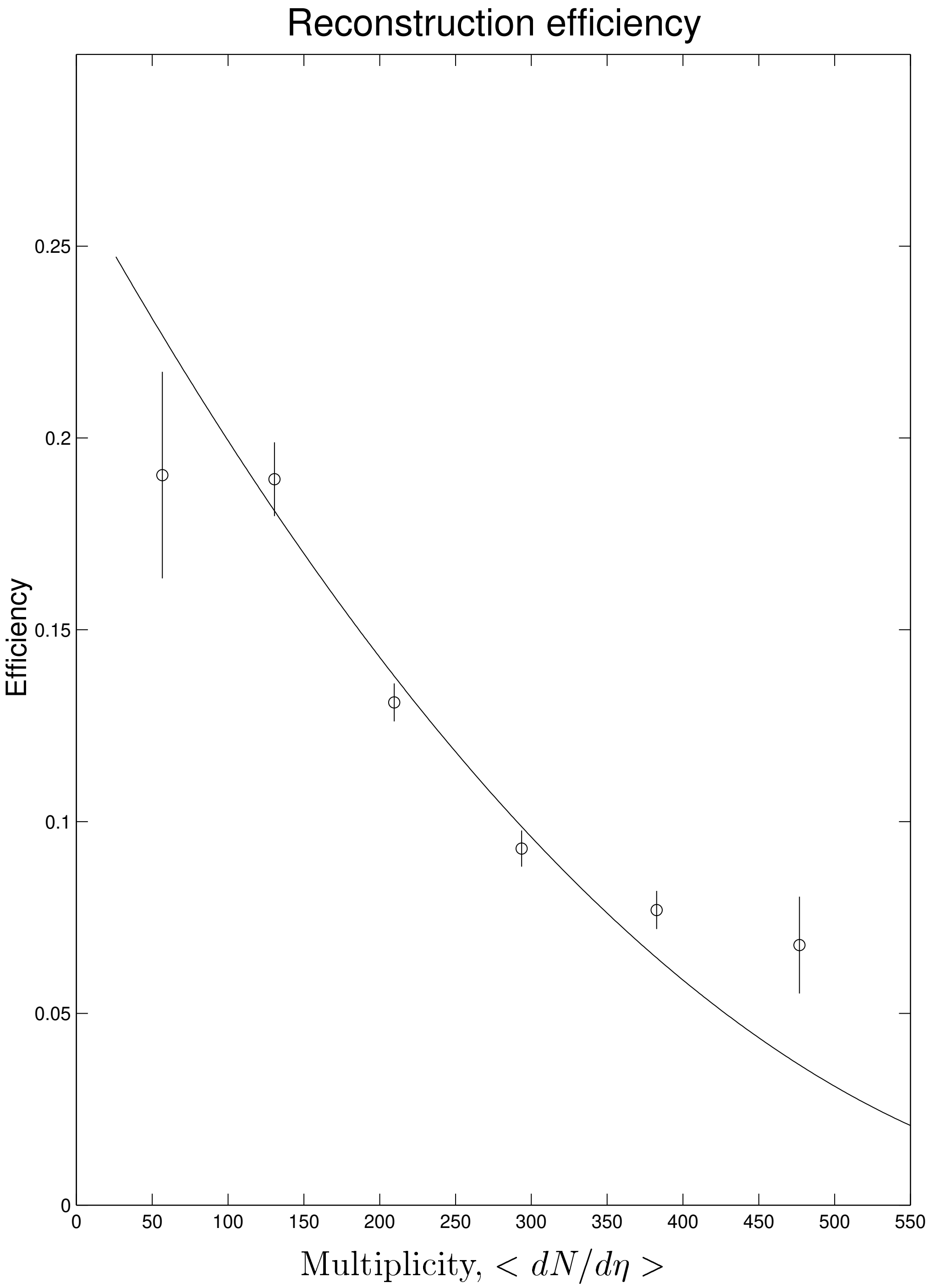

Figure 3.13: Pair reconstruction efficiency as a function of multiplicity. The curve represents the Monte-Carlo study of the efficiency whereas the points represent the efficiency derived from a sample of reconstructed π^0-Dalitz decays.

3.8 The event generator

The CERES event generator generates e^+e^- pairs from all known hadronic sources that contribute to the mass range covered in the CERES experiment. This is an essential tool to compare the measured e^+e^- invariant mass spectrum to the expectation from known sources.

The hadronic sources for electron-positron pairs in the low mass region accessible by CERES are: π^0, $\eta(547)$, $\rho^0(770)$, $\omega(782)$, $\eta\prime(958)$ and the $\phi(1020)$. The ρ^0, ω and ϕ are vector mesons, $J^{PC} = 1^{--}$, and therefore can decay to e^+e^- while the π^0, η and $\eta\prime$, $J^{PC} = 0^{-+}$, have a Dalitz decay channel to $e^+e^-\ \gamma$. The ω has an additional channel to e^+e^- via a Dalitz decay to $e^+e^-\ \pi^0$. The event generator simulates all these hadronic e^+e^- production processes, namely $\rho^0, \omega, \phi \rightarrow e^+e^-$, $\pi^0, \eta, \eta\prime \rightarrow e^+e^-\gamma$ and $\omega \rightarrow e^+e^-\pi^0$. The open charm contribution is negligible in this mass region (see ref. [30] for recent review) and is not taken into account.

The event generator produces hadrons over the full phase space. The relative meson yields are taken independent of collision system. The yield is scaled proportionally to the particle density. The rapidity distribution for π^0 is approximated by a Gaussian shape fitted to the measured data [31]. For heavier mesons the rapidity distribution is also taken Gaussian, with the width scaled according to the highest possible rapidity for a given particle: $\sigma(m)/\sigma(\pi^0) = y_{max}(m)/y_{max}(\pi^0)$. The p_t distribution for π^0 is similarly generated to fit different experimental data [31, 32, 33] and m_t-scaled for heavier mesons. Relative cross sections of the relevant mesons and their branching ratios to e^+e^- are taken from experimental data [18, 34] and listed in table 3.4 (see [35] for comprehensive discussion).

particle	$(\frac{\mathbf{d\sigma/dy}}{\mathbf{d\sigma_{\pi^0}/dy}})_{y=0}$	**decay process**	**branching ratio to** e^+e^- [36]
π^0	1	$\pi^0 \rightarrow e^+e^-\gamma$	$(1.198 \pm 0.032) \times 10^{-2}$
η	0.069 ± 0.005	$\eta \rightarrow e^+e^-\gamma$	$(5.0 \pm 1.2) \times 10^{-3}$
ρ^0	0.096 ± 0.010	$\rho^0 \rightarrow e^+e^-$	$(4.44 \pm 0.21) \times 10^{-5}$
ω	0.096 ± 0.010	$\omega \rightarrow e^+e^-$	$(7.15 \pm 0.19) \times 10^{-5}$
		$\omega \rightarrow e^+e^-\pi^0$	$(5.9 \pm 1.9) \times 10^{-4}$
$\eta\prime$	< 0.014	$\eta\prime \rightarrow e^+e^-\gamma$	$(6.4 \pm 3.0) \times 10^{-4}$
ϕ	0.008 ± 0.001	$\phi \rightarrow e^+e^-$	$(3.09 \pm 0.07) \times 10^{-4}$

Table 3.4: Relative cross section of the relevant mesons and their branching ratio to e^+e^- [18, 34].

After the decay, the e^+ and e^- are subject to the acceptance cuts of the detector and the cuts of the data analysis procedure, allowing to generate an inclusive mass spectrum which we call a cocktail plot, since it contains all processes with their proper strength.

As explained in the previous section, the CERES results are absolutely normalized to represent the pair production probability per event and per charged particle multiplicity measured in the CERES rapidity acceptance. Therefore, we must normalize the event generator in the same way in order to compare the two. This can easily be done. Since the generator contains the π^0-Dalitz channel, all the contributions can be relatively normalized with respect to the π^0. They are then multiplied by the $N_{\pi^0}/N_{\rm ch}$ ratio which is equal to 0.48, as extrapolated from the NA27 results in p-p at 400 GeV [37].

We included γ-conversions into the generator in order to make systematic studies of the combinatorial background.

In the ultra-relativistic case (energies of both particles $\epsilon_\pm >> m$) the electron and the positron are emitted at angles

$$\theta_\pm = m_e/\epsilon_\pm$$

relative to the direction of the incident photon in opposite directions (the exact angular distribution has essentially a δ-function form [38]). The distribution of electron energy in this case is [38]

$$\frac{d\sigma}{d\epsilon} \sim \frac{1}{\omega^3}(\epsilon_+^2 + \epsilon_-^2 + \frac{2}{3}\epsilon_+\epsilon_-)(\ln\frac{2\epsilon_+\epsilon_-}{\omega m_e} - \frac{1}{2})$$

where E_+, E_-, ω are the energies of positron, electron and original γ-quanta respectively, and m_e is electron mass.

The opening angle distribution of the conversion pairs is shown in Fig. 3.8.

Chapter 4

Physics Results

In this chapter I describe in detail the results of the 1996 data analysis. The experimental dielectron distributions (invariant mass, p_t and multiplicity dependences) are compared to expectations from the known hadronic sources and to several theoretical models. An outlook is also given.

4.1 Results of the 1996 data analysis

4.1.1 Mass spectrum

The final sample, obtained by the method described in the previous chapter, contains 5013 $\pm$ 128 reconstructed e^+e^- pairs with invariant mass $m < 0.2$ GeV/c^2 and a signal-to-background ratio of 1.0. For masses $m > 0.2$ GeV/c^2 we find a net signal of 1722 $\pm$ 170 pairs (28746 e^+e^-, 13436 e^+e^+, 13588 e^-e^-) with a signal-to-background ratio of 1:15.7 . The resulting invariant mass spectrum of e^+e^- pairs is shown in Fig. 4.1 together with the expected contributions from hadron decays calculated using the event generator described in sect. 3.8, both normalized as described in sect. 3.7. The statistical errors of the data are shown as vertical bars whereas the systematic errors are given separately as brackets. The latter contain contributions from the uncertainties in the calculation of the charged-particle density, the pair reconstruction efficiency, the absolute background level and the background smoothing procedure. They add up to 25% and are strongly correlated for close mass bins.

The results displayed in Fig. 4.1 are qualitatively very similar to those previously found in S–Au collisions (see Fig. 1.3). The invariant mass spectrum of e^+e^- pairs is in good agreement with the predictions from known hadron decays below 200 MeV/c^2 where the expected yield is dominated by π^0-Dalitz decays. For masses above 200 MeV/c^2 the measured pair yield deviates from the expectations and the yield is clearly enhanced compared to that predicted from hadron decays. In the mass interval $0.2 \leq \mathrm{m} \leq 2.0$ GeV/c^2 the enhancement factor (the ratio of the integrated measured yield to the yield calculated from the known hadronic sources, see sect. 3.8) is 1.8 $\pm$ 0.25 (stat) $\pm$ 0.45 (syst).

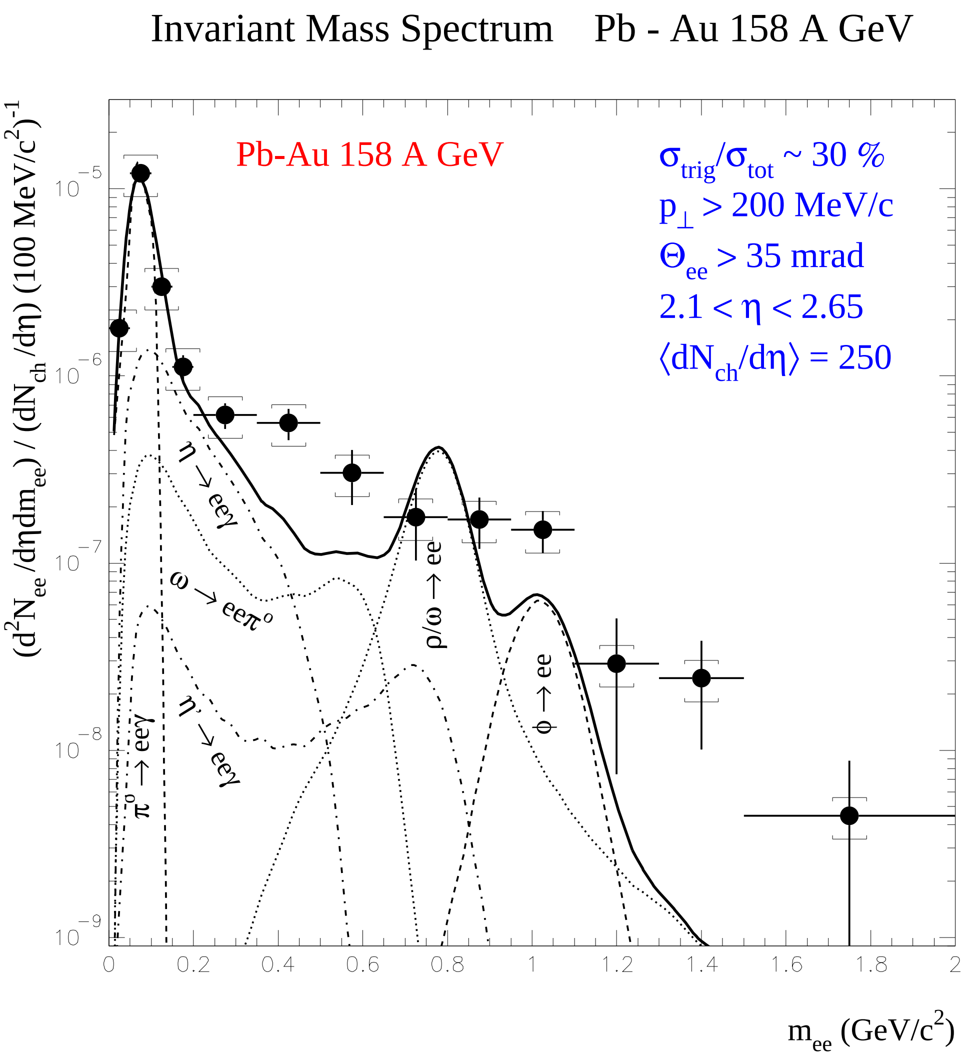

Figure 4.1: Inclusive e^+e^- mass spectrum in 158 A GeV Pb–Au collisions normalized to the observed charged-particle density. The solid line represents the sum of the various contributions from hadron decays. Systematic (brackets) and statistical errors (bars) are plotted independently of each other.

4.1.2 Transverse momentum dependence

Fig. 4.2 shows the mass spectra for subsamples with different pair-p_t: $p_t < 500$ MeV/c (left panel) and $p_t > 500$ MeV/c (right panel). The generator curve shown is folded with the momentum resolution and normalized as discussed in sect. 3.7 and 3.8. There is a striking difference between the two cases. One sees that the enhancement in the mass region m =200–600 MeV/c^2 is much more pronounced at low pair-p_t, $p_t < 500$ MeV/c, whereas for $p_t^{ee} > 500$ MeV/c the e^+e^- yield follows closely the shape of the expected yield from hadronic sources. The shape of the expected yield is very different for the two p_t^{ee} subsamples due to the p_t cut ($p_t > 200$ MeV/c on each track), applied during the data analysis (the effect of this cut on the pair acceptance is illustrated in Fig. 3.3).

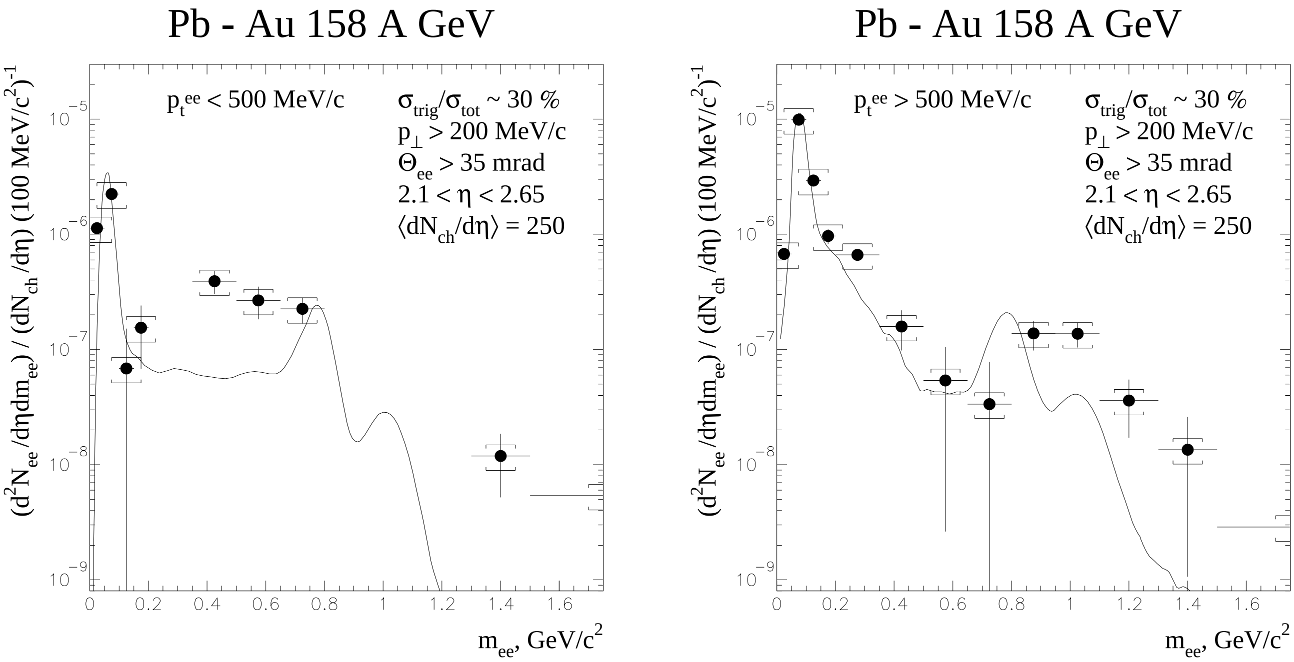

Figure 4.2: Inclusive mass spectra for different transverse momenta of dilepton pairs. Left: pair p_t^{ee} <500 MeV/c. Right: pair p_t^{ee} >500 MeV/c. The solid line represents the sum of the various contributions from hadron decays.

Fig.4.3 shows the pair transverse momentum distributions for low-mass (m <200 MeV/c^2) and high-mass (m >200 MeV/c^2) pairs. For masses below 200 MeV/c^2 the p_t distribution agrees with the prediction for π^0-Dalitz decays (left panel) up to a pair-of $p_t \sim 0.9$ GeV/c. At higher momenta we clearly see an enhancement, which is well above experimental errors. Although this enhancement is of the order of 2–3 in the range $1.0 < p_t < 1.5$ GeV/c, it represents an unsignificant effect (∼2%) in the total yield. For higher masses, the enhancement is visible over the entire p_t range, but more pronounced, as mentioned above, at low pair-p_t.

4.1.3 Multiplicity dependence

The dependence of the observed dielectron yield on the associated hadron multiplicity is a useful tool to characterize its origin. In the present Pb–Au sample we tried to exploit the

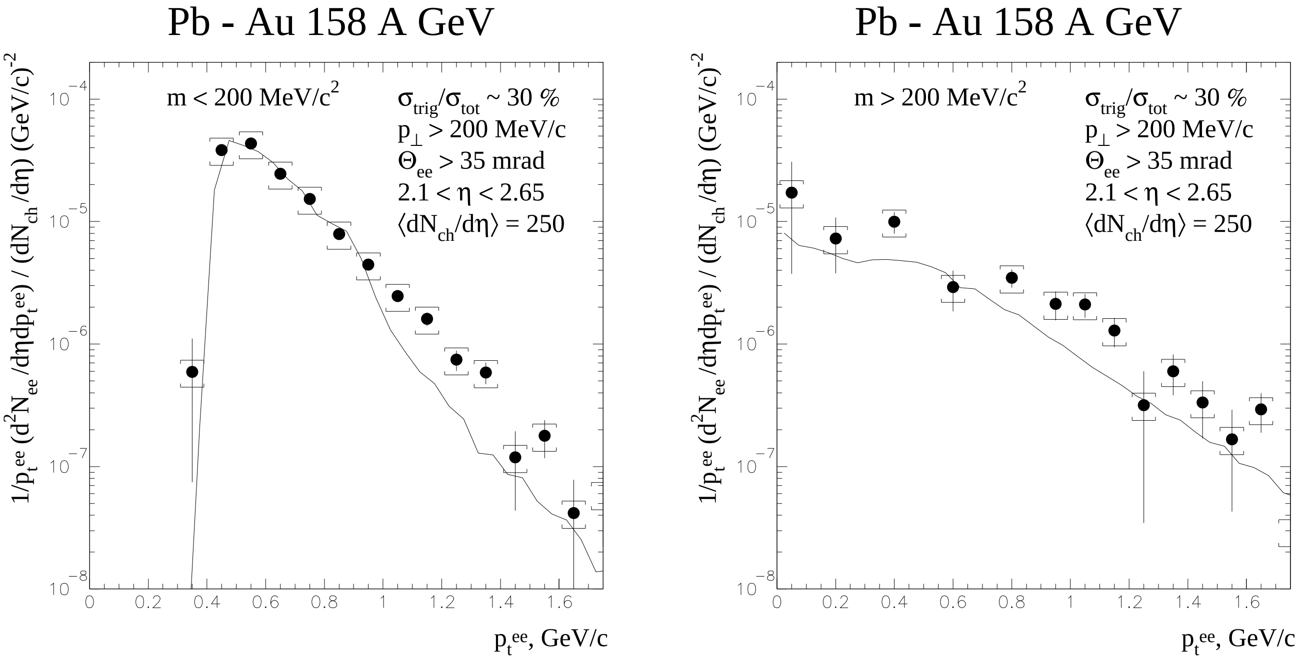

Figure 4.3: Transverse momentum spectra. Left: low-mass pairs ($m < 200$ MeV/c^2). Right: high-mass pairs ($m < 200$ MeV/c^2) p_t^{ee} >500 MeV/c. The solid line represents the sum of the various contributions from hadron decays.

large impact parameter range covered by the data to study the measured yield as a function of the event multiplicity. The distribution dN$_{ch}$/dη for $2 < \eta < 3$ as measured in the SiDC telescope and corrected for efficiency and pile-up in the silicon detectors is divided into four bins with approximately equal number of events (see upper panel of Fig. 4.4). The lower panel of Fig. 4.4 shows the pair density per charged particle density integrated over the mass range $m > 200$ MeV/c^2 for the four multiplicity bins. The scale on the right in Fig. 4.4 represents the enhancement factor for each multiplicity bin. Fig. 4.4 includes also the results from our p–Be and p–Au data samples [18]. If hadron decays were to be the only source of dielectron pairs – as it is the case in p–p and p–A collisions – the data should scale linearly with multiplicity, i.e. should follow the horizontal line shown in the plot. Although the error bars are large, the data clearly indicate a non-linear dependence as a function of multiplicity.

It is generally believed, that thermal dileptons should scale quadratically with particle density [40] ($dN_{ee}/d\eta \sim (dN_{ch}/d\eta)^{\alpha}$ with $\alpha = 2$). However, Feinberg [41] pointed two decades ago, that from very general arguments the number of thermal photons and dileptons should scale with α =4/3. Recent hydrodynamic calculations [42] are consistent with a scaling power $\alpha \sim 1.1$. We compare our experimental data with all three hypothesis (Fig.4.4). Due to relatively large error bars, all three curves fit the data fairly good, though the quadratic dependence seems to be the best.

The spectral shape of the dilepton excess seems also to change significantly as a function of the charged-particle rapidity density. The effect is illustrated in Fig. 4.5. As the charged-particle rapidity density grows, the "valley" between π^0-Dalitz and ρ/ω peaks gradualy disappears.

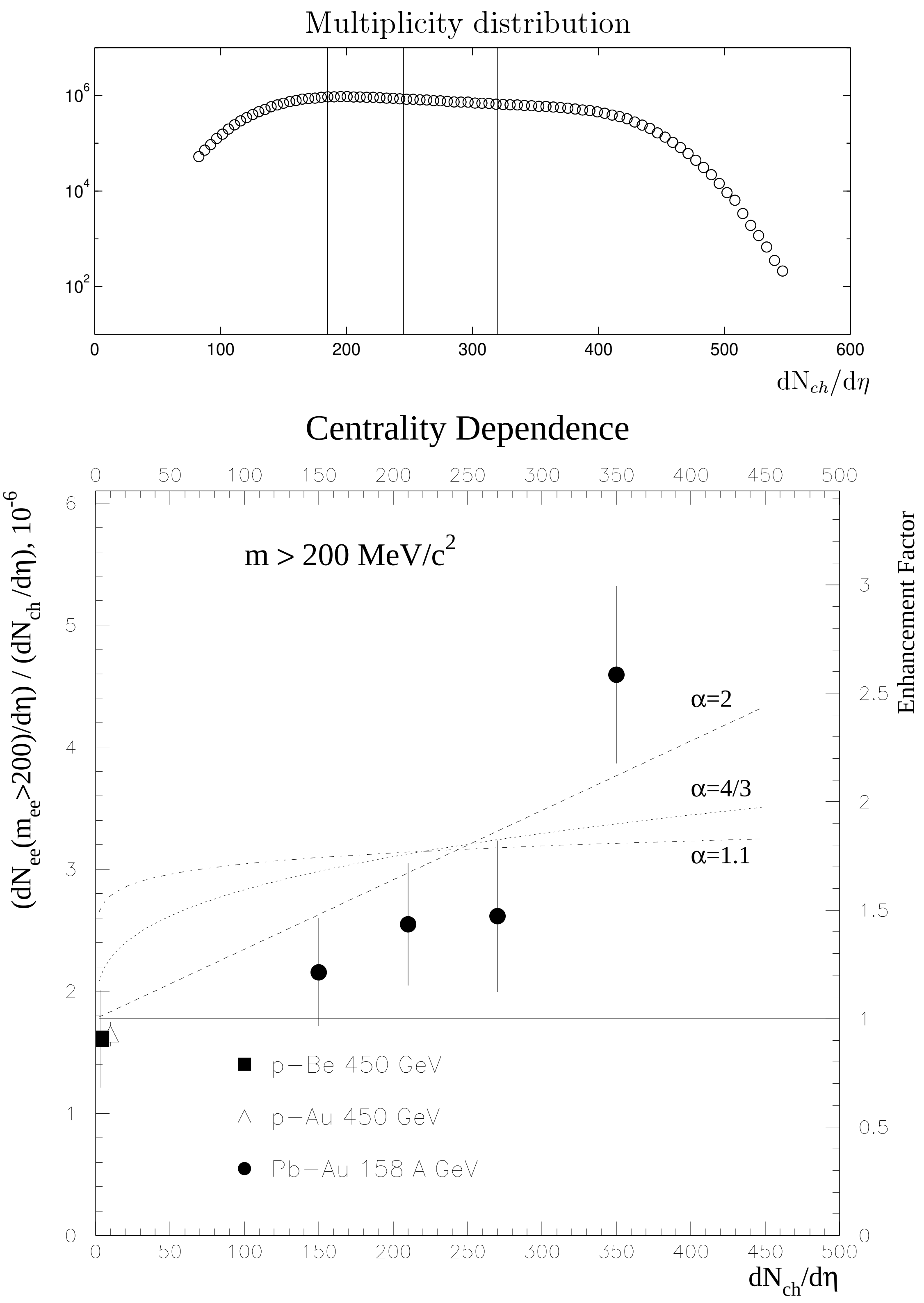

Figure 4.4: Lower panel: dielectron yield and enhancement factor as function of particle density in comparison with different scaling functions $\frac{dN_{ee}}{d\eta} \sim (\frac{dN_{ch}}{d\eta})^{\alpha}$, $\alpha = 2$ [40], $\alpha = 4/3$ [41] and $\alpha = 1.1$ [42]. Upper panel: multiplicity distribution of recorded events. The vertical bars show the division in 4 bins with approximately the same number of events in each bin.

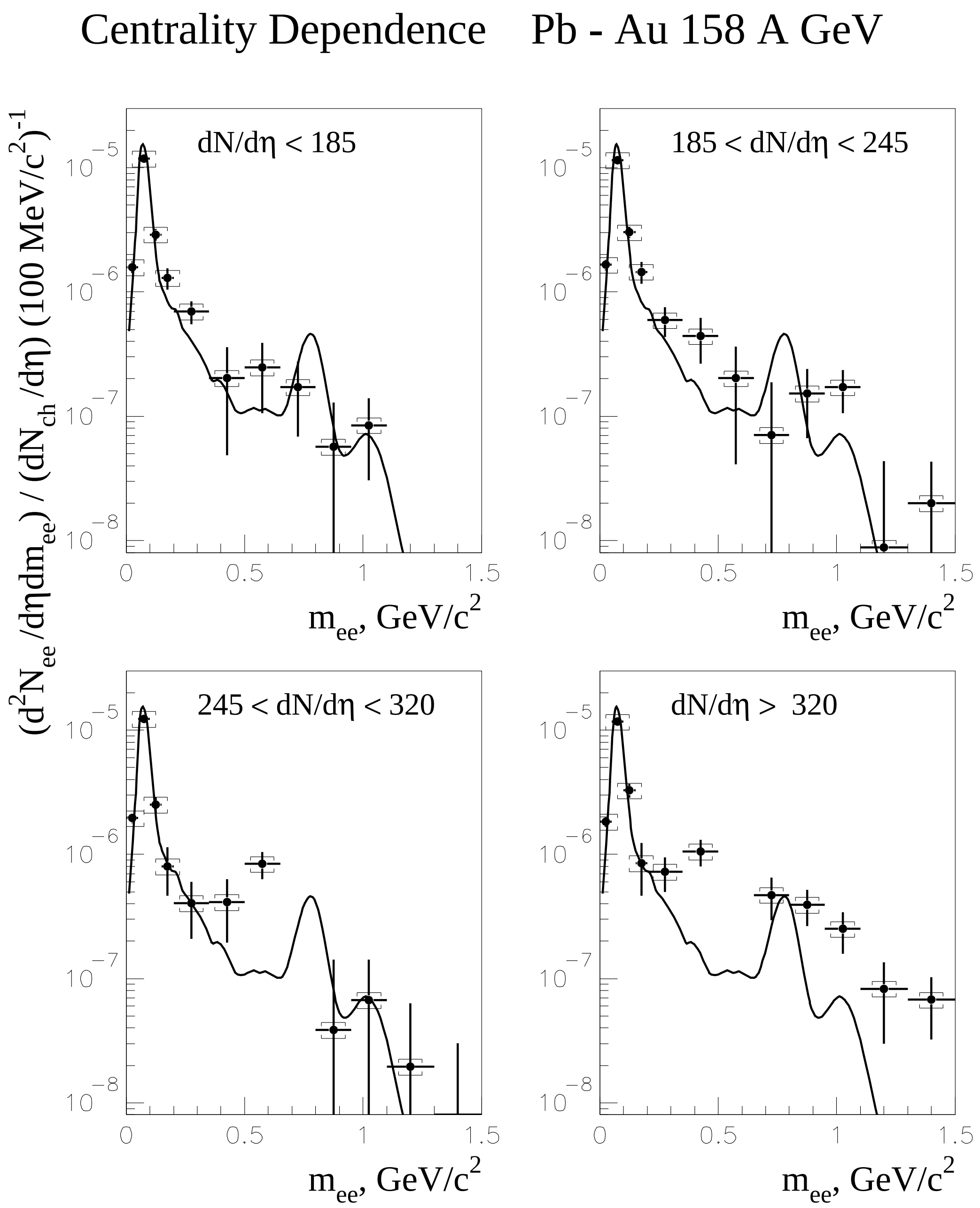

Figure 4.5: Inclusive e^+e^- spectra for different multiplicities

4.2 Comparison to other CERES results

4.2.1 1995 data results

The first CERES measurement of low-mass pairs with the Pb beam was performed in the fall of 1995. This was a relatively low-statistics run. The final sample contained 1038 ± 55 reconstructed e^+e^- pairs for invariant masses below 0.2 GeV/c^2 with a signal-to-background ratio of 1.05. For masses above 0.2 GeV/c^2, CERES found 5834 e^+e^-, 2494 e^+e^+, and 2696 e^-e^- pairs resulting in a net signal of 648 ± 105 pairs with a signal-to-background ratio of 1/8 [39].

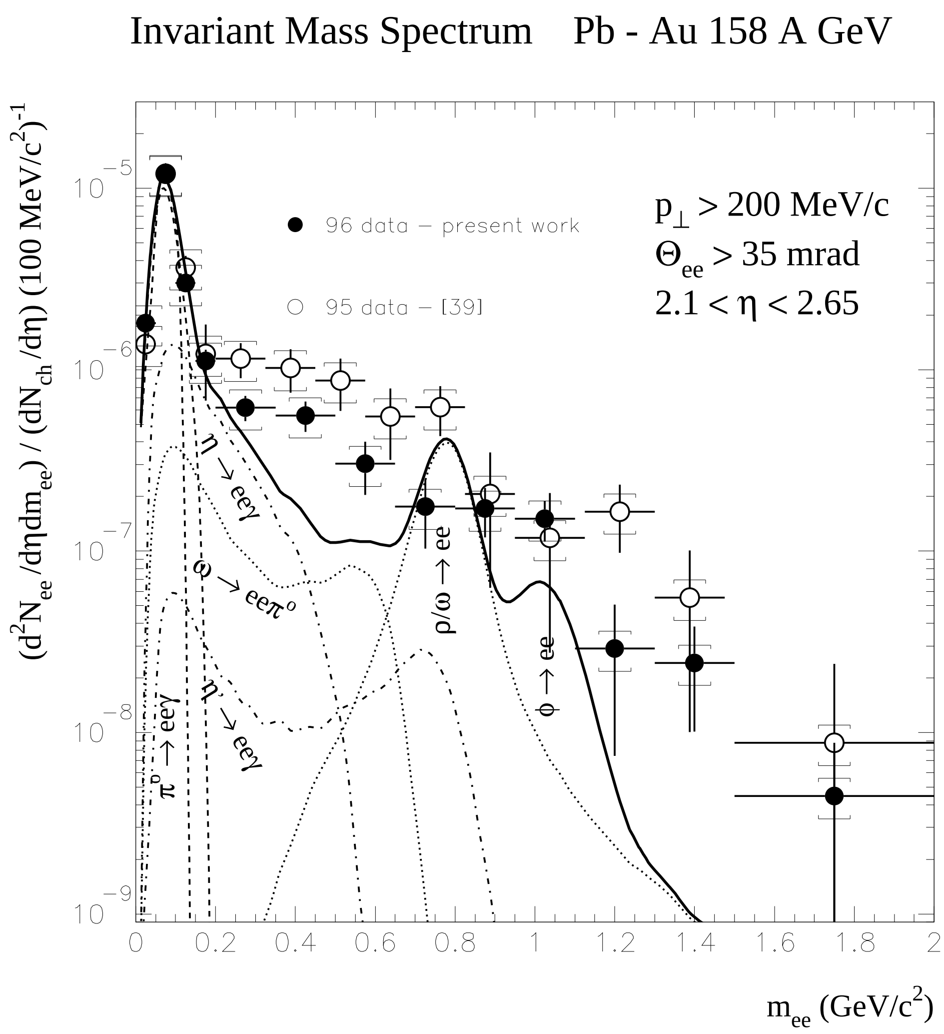

Figure 4.6: Comparison of the e^+e^- invariant mass spectra from the 1995 [39] and 1996 data sets.

The invariant mass spectra, obtained from the 1995 data and the present analysis of the 1996 data are shown together in Fig. 4.6. The data points are shown with statistical (vertical bars) and systematic (brackets) errors plotted independently of each other. First of all one notes

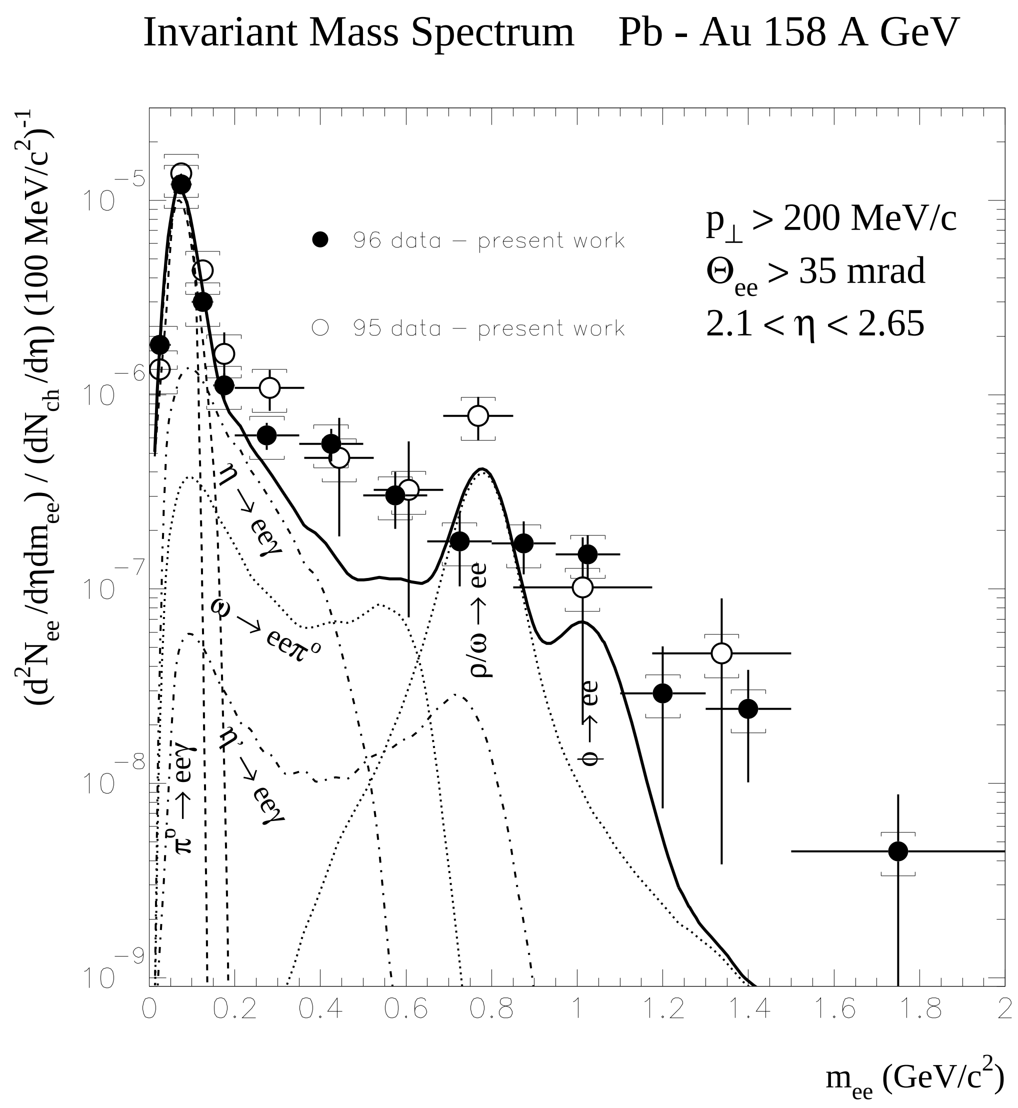

Figure 4.7: Comparison of the e^+e^- invariant mass spectra from the reanalyzed 1995 data set and the 1996 data set.

that the two data sets are compatible within their error bars. This is a noteworthy feature if one considers the complexity of the analysis, in particular the huge filtering. For example, in the 96 data sample, out of $42 \cdot 10^6$ analyzed events, the final result displayed in Fig. 4.6 contains a total of 1722 pairs with $m > 200$ MeV/c^2. However, one also immediately notices that the 1995 points are systematically higher. The experimental set-up was unchanged in the two runs, however, the analysis procedures were slightly different. In the 1995 data analysis the physics rejection cuts were adjusted by maximizing the quantity ϵ^2/B (which is a measure of the magnitude of the signal in a background-free situation) where ϵ is the pair reconstruction efficiency obtained from Monte-Carlo simulations, while B is the background taken to be equal to the measured like-sign pair background [39]. This procedure disregards the size of the signal itself. But it uses the measured like-sign pair background for B. In contrast, in the present analysis all rejection cuts were adjusted on samples of fully reconstructed γ-conversions and π^0-Dalitz decays, without using at all the measured signal or the measured background of open pairs with m>200 MeV/c^2.

We have investigated whether the systematic effect displayed in Fig. 4.6 could be a reflection of the systematic errors of the different analysis procedures. We repeated the second stage of the 1995 data processing (see sect. 3.1), i.e. the cuts on the compressed data. In order to simplify the comparison and limit the scope of the work, the structure of the cuts was preserved as in [39]. The physics rejection cut values were entirely based on Monte-Carlo both for the optimization of the signal and the rejection of the background, thereby avoiding the use of the open pair data to maximize the background rejection. The quality and matching cuts (see sect.3.4) were left unchanged.

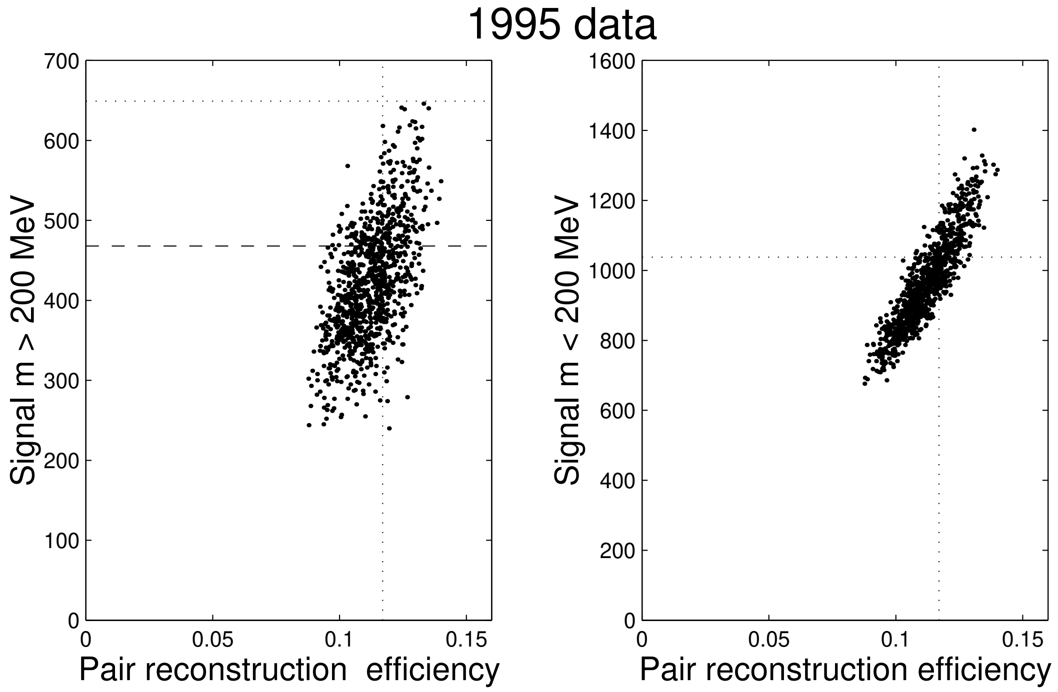

Figure 4.8: Effect of random variation of the cut values by ± 20% in the 1995 results. The set of cuts, leading to the results shown in Fig. 4.6 and 4.7, are reperesented by the crossing of the dotted lines for the original analysis [39] and dotted with dashed lines for the present reanalysis.

The invariant mass spectrum of e$^+$e$^-$ pairs from this reanalysis of the 1995 data is shown in Fig. 4.7 together with the 1996 data results. The two data sets are in agreement within statistical errors and no systematic difference is apparent anymore. Quantitatively, the new sample contains 1044 ± 53 reconstructed e$^+$e$^-$ pairs for invariant masses below 0.2 GeV/c^2 with a signal-to-background ratio of 1.0 . For masses above 0.2 GeV/c^2 we find a net signal of 468 ± 101 pairs with a signal-to-background ratio of 1:11 . The enhancement factor in the mass region 0.2 – 2 GeV/c^2 is 2.7 ± 0.6, in agreement with the 1996 results within 1σ.

We have also checked the stability of the result by performing 1000 random variations of the cut values within ± 20% of the values established in the original [39] analysis. The results of this random walk are given in Fig. 4.8. One can see, that the results of [39] represent a marginal point in the distribution of Signal vs. Efficiency, while the results of the reanalysis correspond to the most dense area of this distribution.

4.2.2 Monte-Carlo analysis method

The 1996 data have also been analyzed [43, 44] using a method in which all cuts are tuned on Monte-Carlo events both for the optimization of the signal and the background rejection. The results are as follows. The final sample contains 5631 $\pm$ 129 reconstructed e^+e^- pairs for invariant masses below 0.2 GeV/c^2 at a signal-to-background ratio of 1/0.97. For masses above 0.2 GeV/c^2 the net signal is 2018 ± 237 pairs with a signal-to-background ratio of 1/13. In the mass interval $0.2 \leq m \leq 2.0$ GeV/c^2 the enhancement factor is 2.4 $\pm$ 0.25 (stat). These results are quantitatively in good agreement with the present work. The ratio between the number of

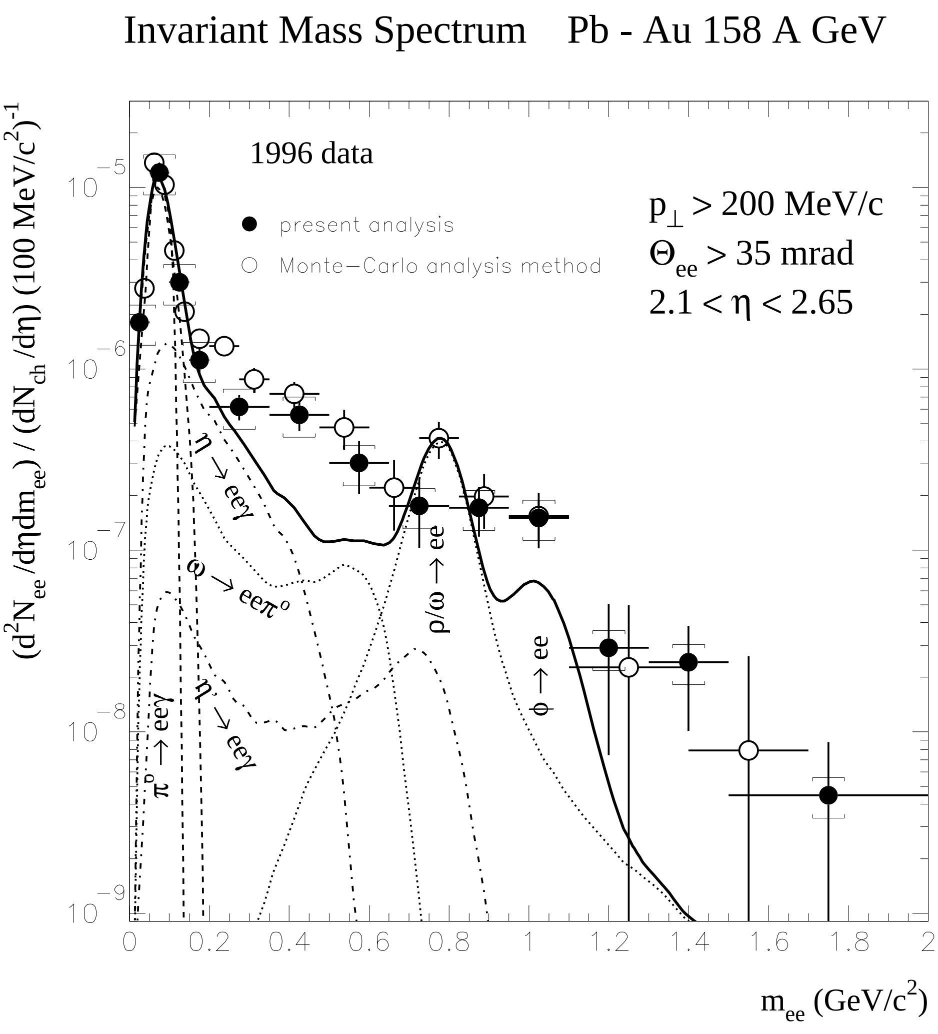

Figure 4.9: Comparison of the e^+e^- invariant mass spectra obtained from the 1996 data in the present work (solid dots) and using a Monte-Carlo analysis method (refs. [43, 44]).

pairs with $m > 200$ MeV/c^2 and $m < 200$ MeV/c^2 is 0.36 ± 0.03, which is fairly consistent with our value of 0.34 ± 0.05. Also the ratio between the number of pairs with $p_t < 400$ MeV/c and $p_t > 400$ MeV/c is consistent, we get 0.25 ± 0.11, and the Monte-Carlo method yields 0.21 ± 0.1. So the reason why we find 1722 open pairs in comparison to 2018 is because the final efficiency after all our cuts is about 15% smaller.

The invariant mass spectra are compared in Fig. 4.9. Keeping in mind that the analysis methods are different (although they both use the same strategy), the level of agreement displayed in Fig. 4.9 is remarkable and well within the errors.

4.3 Comparison to other CERN experiments

Other results are now available from the HELIOS-3 and NA38/50 experiments, involved in the measurement of $\mu^+\mu^-$ pairs at the CERN SPS. The results cover measurements with p, S and Pb beams, and have also revealed with heavy-ion beams an enhancement of the dilepton yield over a very broad range of invariant masses.

The HELIOS-3 collaboration studied muon pairs in p–W and S–W collisions. The comparison of the two spectra reveals an enhancement that covers a very broad mass range, from about 200 MeV/c^2 up to below the J/ψ. The excess though, is considerably lower than the one measured by CERES in S–Au collisions [45]. This could be due to their different rapidity coverage. CERES covers the mid-rapidity region $2.05 < \eta < 2.65$, whereas HELIOS-3 covers the forward region $3.7 < \eta < 5.5$. Consequently, the average charged particle rapidity densities accessible by the two experiments differ by at least a factor of 2 [46], and this strongly affects the dilepton yield as discussed in section 4.1.3.

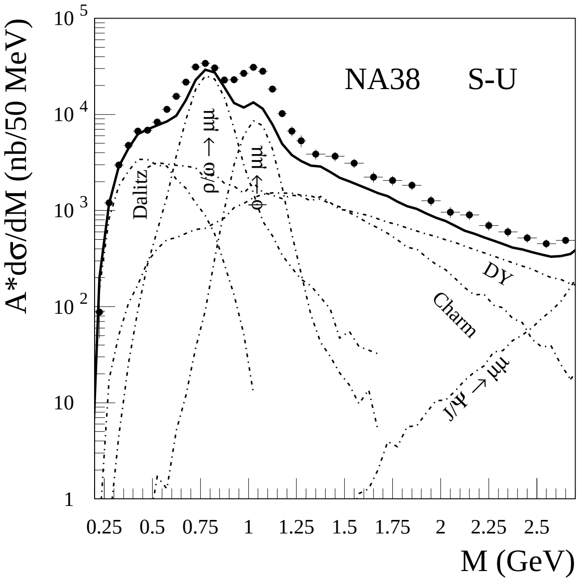

Figure 4.10: Inclusive $\mu^+\mu^-$ mass spectra measured by NA38 in 200 A·GeV S–U collisions. The thick line represents the summed yield of all known sources. The individual contributions are also shown [47].

The NA38/50 collaboration, focussed on the J/ψ production, is also studying the low-mass region. Preliminary results on p–U, S–S and S–U collisions at 200 GeV/nucleon were presented at the Quark Matter 97 Conference [47]. Whereas the p–U data are well reproduced by a cocktail of hadronic sources (with the somewhat uncertain extrapolation of the Drell-Yan contribution into low masses), the S data show an enhancement of low-mass pairs which clearly extends over the intermediate mass region as illustrated in Fig. 4.10.

The shape and the enhancement factor in the low-mass dilepton spectrum as measured by CERES and by NA38 differ significantly. The resonance decays are clearly visible in the NA38 spectrum, whereas in the S and Pb CERES results the structure is completely washed out (see Figs.1.3 and 4.1). The question of consistency between the two experiments thus arises. Resolution effects can be readily ruled out since the low-mass spectrum in p–Be and p–Au collisions measured by CERES with the same apparatus clearly shows the ρ/ω peak (see Fig.1.3 – right panel). The origin of this difference is likely to be in the phase space. Although the two experiments cover nearly symmetric ranges with respect to mid-rapidity ($\eta = 2.1 - 2.65$ and $\eta = 3 - 4$ in CERES and NA38 respectively) they are very different in their p_t coverage. CERES has a relatively low p_t cut of 200 MeV/c on each track whereas NA38 is restricted to $m_t > 0.9 + 2(y_{lab} - 3.55)^2$ GeV/c^2. As was mentioned in sect. 4.1, CERES sees a great part of its excess in the low-p_t region (below $p_t^{ee} < 500$ GeV/c), which is invisible for NA38. Moreover, NA38 has no centrality selection in the trigger whereas the CERES data correspond to the top 35% of the geometrical cross section, and the results discussed in sect. 4.1.3 clearly indicate that the enhancement increases faster than linearly with multiplicity.

4.4 Discussion

4.4.1 Reliability of the results

We discuss two questions concerning the reliability of the results:

- Could the analysis method lead to a systematic bias?
- Could the excess originate from improper background subtraction?

1. Our method of cuts adjustment using (i) "pure" samples of γ-conversions and π^0-Dalitz decays, independently of the open pairs and (ii) the random variation of the cuts make the possibility of a bias in the final results very unlikely. In addition, the good agreement between the results of the Weizmann and Heidelberg groups (see sect. 4.2.2), obtained by different analysis methods adds confidence to the reliability and stability of the results.

2. The signal is obtained by subtracting the number of like-sign pairs from the number of unlike-sign pairs. By doing this, we must be sure that the combinatorial background is the same in these two samples. Otherwise, since the signal-to-background ratio is very low, a small difference between the two could have significant consequences on the signal.

We also used the Monte-Carlo efficiency study to verify, that the data processing algorithm does not introduce any bias on the + vs. − or like-*vs.*-unlike reconstruction efficiency. We studied the pair reconstruction efficiency by overlaying two pairs of π^0-Dalitz tracks on a single raw event. This overlay yields 2 genuine and 4 fake pairs in each event. The 4 fake pairs (2 of them – like-sign, and 2 – unlike-sign) represent ideally the combinatorial background. We calculated the reconstruction efficiency of these artificial pairs.

The results showed, that within the statistical errors – less than 1% at 3σ (99.5%) confidence level the CERES data analysis chain does not prefer pairs of either sign.

The Heidelberg group made another test: they reversed all the rejection cuts, yielding therefore a "clean" background sample. Their study indicated [44], that we can exclude an asymmetry of more than 1% with a 90% confidence level.

4.4.2 Hadronic sources

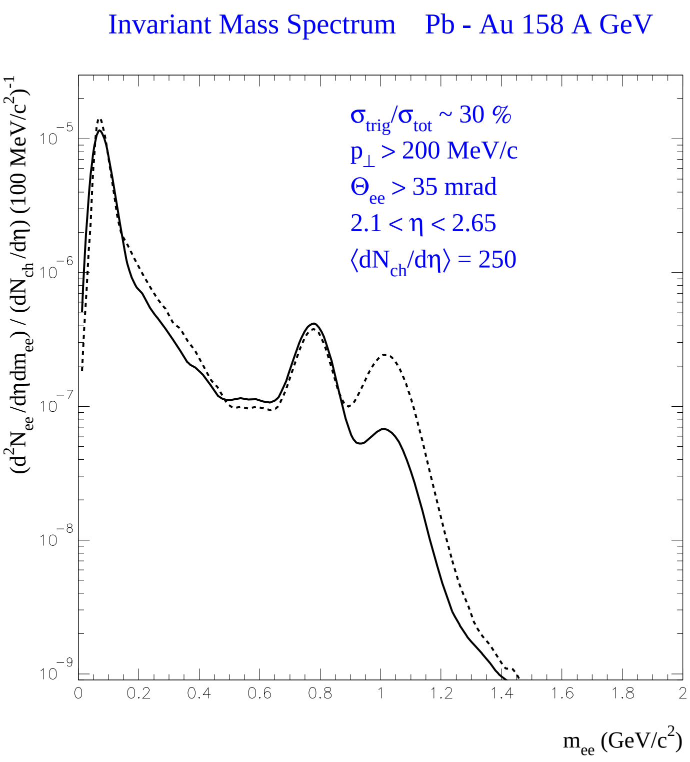

Figure 4.11: e^+e^- inclusive spectra according to p–p scaled (solid line) and thermal [44] (dashed line) models.

In section 4.1, the results were compared to the expected contributions from the known hadron sources under the assumption of constant particle production ratios in going from p–p to nucleus–nucleus collisions. One may question the validity of such an assumption although it is a reasonable one and it has no free parameters. More specifically, one could ask whether it would be possible to reproduce the low-mass S–Au and Pb–Au data of CERES with a modified "cocktail", using an enhanced production of the η, η' and ω. Inspection of the S–Au spectrum of Fig. 1.3 or the Pb–Au spectrum of Fig. 4.1 reveals that this can fairly well be achieved. However, this would create a contradiction with other existing experimental information. For example, the ratio η/π^0 was measured by WA80 [48] and WA98 [49] in S and Pb-induced collisions and was found close to the ratio measured in p–p collisions, thus not allowing the enhancement of the η by the factor of 3-5 which would be needed to bring the cocktail close to the data. Alternatively, one would have to enhance the η' or/and the ω yields by at least one order of magnitude; such a dramatic increase would have observable consequences in the real photon yield (since these particles have a large branching ratio to decay into photons) creating a conflict with the data of CERES and WA80 that give an upper limit of real photon enhancement of about 10%. We therefore conclude that it is not possible to modify the particle ratios in the cocktail of known hadronic sources such that one could explain the observed low-mass dilepton enhancement. However, small modifications of the particle ratios are certainly possible and even justified. The contributions of hadron decays to the e^+e^- yield in the limited acceptance ($2.05 < \eta < 2.65$) of the CERES spectrometer depends on the production yield of the hadrons, the branching ratio to decay into e^+e^- and on the p_t and rapidity distributions of the hadrons. There is now growing evidence, that except for the branching ratios all other ingredients are different for p-induced and Pb-induced collisions:

- The production of the heavier hadrons is enhanced compared to the π^0 production, as for example the η/π^0 ratio as observed by WA98 [49] and the $2\phi/(\pi^+ + \pi^-)$ ratio by NA50 [47] in Pb-induced collisions. The measured particle ratios are well explained by a thermal model, assuming chemical equilibrium [50], and consequently we can use this model to derive presently unknown particle ratios.

- It was observed that the inverse p_t-slope increases sytematically with the mass of the hadron [51]. This behaviour is well described in a model which assumes a constant temperature and radial flow.

- While the width of the rapidity distributions decreases with the particle mass in p-induced collisions, it is observed that it stays constant in Pb-induced collisions.

All these observed changes have been implemented in the CERES event generator to simulate the contributions of hadron decays [44]. Fig. 4.11 shows the inclusive e^+e^- spectra calculated by this method (dashed line) in comparison with the p–p generator, described in sect. 3.8. The two generators give very similar results at masses $m < 0.8$ GeV/c^2. Compared to the pure p–p cocktail the thermal model predicts a 30% larger yield for $m_{e^+e^-} > 0.2$ GeV/c^2, the main difference occuring in the predicted ϕ meson yield. So the enhancement factor of 1.8 that we report translates to 1.4, if we take the hadronic predictions from the thermal model.

4.4.3 Theoretical interpretations

The CERES results have triggered a considerable amount of theoretical work. In this section the main highlights are summarized.

It is rather clear that the explanation of the low-mass excess requires an additional source, not present in the p–p case. The two-pion annihilation channel $\pi^+\pi^- \to e^+e^-$ which is expected to become important in a high density environment, is an obvious candidate. The characteristic features of the excess – its onset at a mass $m_{ee} \sim 2m_\pi$, its extension to the low-mass region below and around the ρ-meson suggest indeed that the excess is due to this channel. This would then be the first indication of thermal radiation emitted from the dense hadronic matter formed in relativistic heavy-ion collisions.

Many authors reported calculations, which have all included the pion annihilation channel. The collision dynamics was treated in completely different ways in these works (see ref. [52]

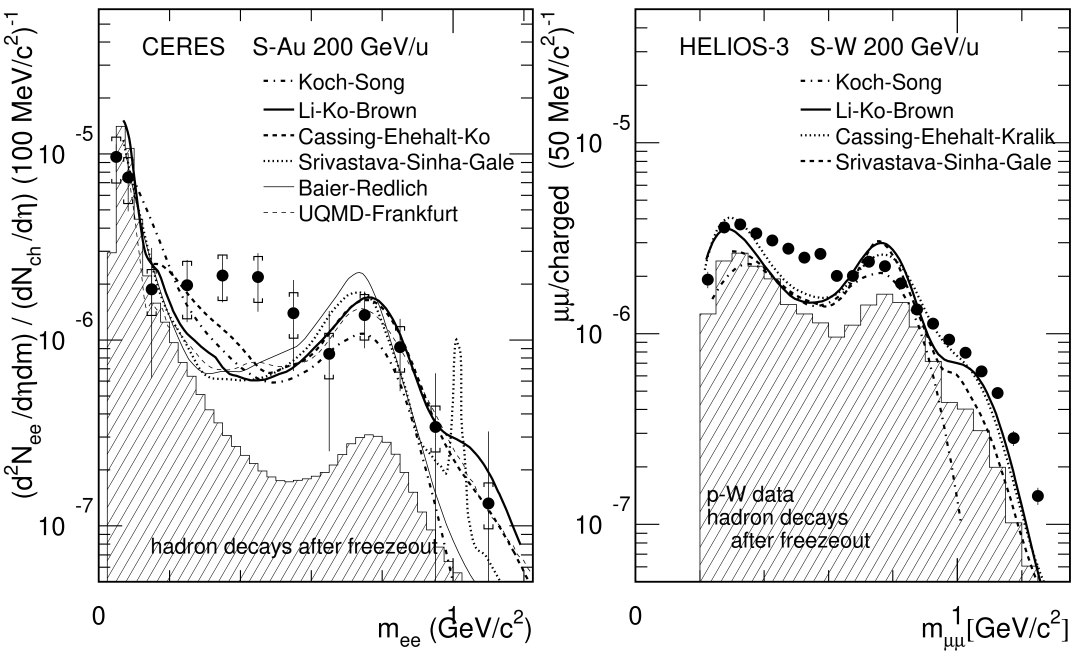

Figure 4.12: Comparison of the CERES and HELIOS-3 results with different models [52] including the two-pion annihilation channel.

for a comprehensive overview and references). We can quote transport models with explicit propagation of baryons and mesons that assume the formation of a hadronic system in thermal equilibrium [53] or without equilibrium [54]. Some treat the system in a hydrodynamical models, and some of them invoke formation of a QGP [55, 56, 57]. The common constraint is that the models are required to reproduce experimentally observed hadronic variables like multiplicity, rapidity and p_t distributions. Surprisingly enough, the predictions of all theses models are very similar (up to a factor of $\sim$2, see Fig. 4.12), though their assumptions on the collision dynamics are as mentioned above quite different. This may indicate that the dilepton yield is quite insensitive to particular details of the collision evolution. One sees, that the pion channel accounts for a large fraction of the observed excess. The calculations reproduce well or even overshoot the dilepton yield near the ρ/ω mass (a direct consequence of the inclusion of the pion annihilation channel which is dominated by the pole of the pion form factor at the ρ mass). However, they all fail to reproduce the data at lower masses, in the region 0.2 $< m_{e^+e^-} <$0.5 MeV/c^2.

Data in this mass region have been quantitatively explained by taking into account the in-medium modifications of the vector mesons. Namely, it was supposed that meson masses – in particular the ρ meson – decrease in the hot and dense fireball as a precursor of chiral symmetry restoration [8]. With this approach, first proposed by Li, Ko and Brown [53] following the original Brown-Rho scaling [58], excellent agreement has been achieved with the CERES data (solid line in Fig. 4.13). At SPS energies, the ρ-meson mass drops by approximately a factor of 2, mainly due to the high baryon density of the system.

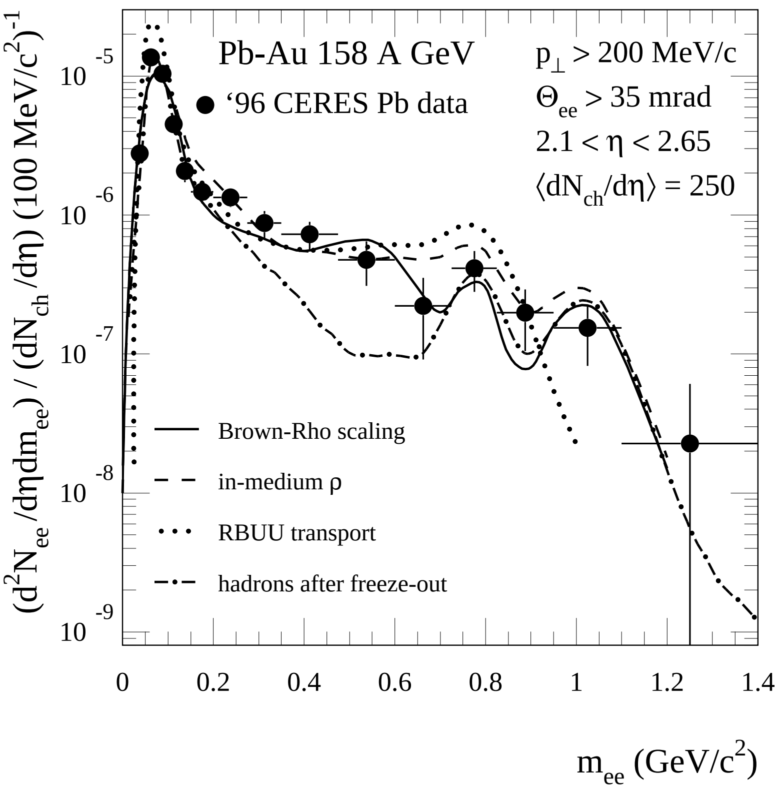

Figure 4.13: CERES results compared to calculations using dropping ρ mass (Brown-Rho scaling), in-medium ρ-meson broadening and RBUU transport model. The dash-dotted line represents the yield from hadrons after freeze-out in thermal model (sect. 4.4.2).

Later a different approach was proposed. It is based on effective Lagrangians and uses a ρ-meson spectral function which takes into account the ρ propagation in hot and dense matter, including in particular the pion modification in the nuclear medium and the scattering of ρ mesons off baryons [59, 60]. This causes a significant broadening of the ρ-meson line shape and consequently leads to a considerable enhancement of low-mass dileptons. These calculations also reproduce the CERES Pb–Au data quite well (see Fig. 4.13, dashed line).

The two approaches are however principally different in their underlying physical picture. In the Brown-Rho scaling the constituent quarks are the relevant degrees of freedom, and chiral symmetry restoration is invoked. The approach of Wambach and coworkers relies on a hadronic description and collision broadening. However, it turns out that the dilepton production rates calculated via hadronic and partonic models are very similar at SPS conditions [61] thus explaining the similar results of the two approaches.

Furthermore, the calculations themselves are not free of debate. Both approaches rely on a high baryon density for the dropping mass or the enlarged width of the ρ meson but the role of baryons is still a question open to debate. The calculations of Zahed and coworkers [62, 63] are in principle similar to the one described above. They address the same physics of in-medium modifications of the ρ spectral function enforcing known constraints, and yet, with a realistic nucleon density ρ_N, they fail to reproduce the low-mass data. The RBUU transport calculations of Koch [64] find also very little effect due to the baryons and come to a reasonably close description of the data (Fig. 4.13, dash-dotted line), but with a considerable overestimation in the ρ/ω mass region, which could be due to an overestimation of the ω-meson production yield.

4.5 Summary and outlook

The results of CERES on Pb – Au collisions confirm the significant excess of dielectron pairs observed by CERES, HELIOS-3 and NA38/50 in S–Au collisions at 200 GeV per nucleon. For central Pb–Au and S–Au collisions the shape of the spectrum and the magnitude of the enhancement are similar. We have found evidence for a non-linear dependence on the multiplicity. Data on p_t-spectra show that the yield is enhanced over the entire range, though more at low pair p_t (below 500 MeV/c). This new information should put significant constraints on the theoretical models which try to interprete the CERES results and should help discriminating among them.

The results obtained with the S and Pb beam seem to hint at in-medium modifications of the vector mesons. The best way to further explore this exciting possibility is to study the 2-body dilepton decays of the ρ, ω and ϕ mesons. It is clear that the present CERES spectrometer does not allow to do that due to the low mass resolution which is of order of $6-7\%$ at the ρ mass. Improving the resolution to the level of the natural width of the ω peak can give us the desired tools to disentangle the meson peaks, and as a consequence to follow their behavior. The lifetimes of ρ, ω and ϕ mesons are 1, 23 and 44 fm/c, respectively. If the initial fireball lives for the order of $10-20$ fm/c, most of the ρ mesons will decay inside the interacting system, while a non-negligible fraction of the ω and ϕ mesons will also decay inside the interacting system. Precise measurement of their yield and their shape should therefore provide information on whether or not the scenarios invoking chiral symmetry restoration are at the origin of the low-mass excess.

To achieve a mass resolution of the order of 2%, which is close to the natural width of the ω meson, CERES has undertaken a major upgrade of the apparatus by the addition of a Time Projection Chamber (TPC) downstream of the double RICH spectrometer. Simulations show that the upgraded CERES apparatus will allow precise spectroscopic studies of the vector mesons ρ, ω and ϕ.

In addition to that, the TPC upgrade will also allow to improve signal-to-background (S/B) ratio which is the major weakness of the CERES results. The TPC can allow us to decrease the magnetic field between the two RICH counters, and probably even to switch it off completely (since its function of momentum measurement will be fulfilled by the TPC). RICH-2 can then play the same role as RICH-1 in identifying γ-conversions and π^0-Dalitz decays, adding redundancy to the rejection scheme and thereby improving the signal-to-background ratio.

The measurements of low-mass pairs in Pb–Au collisions at 158 GeV per nucleon will be

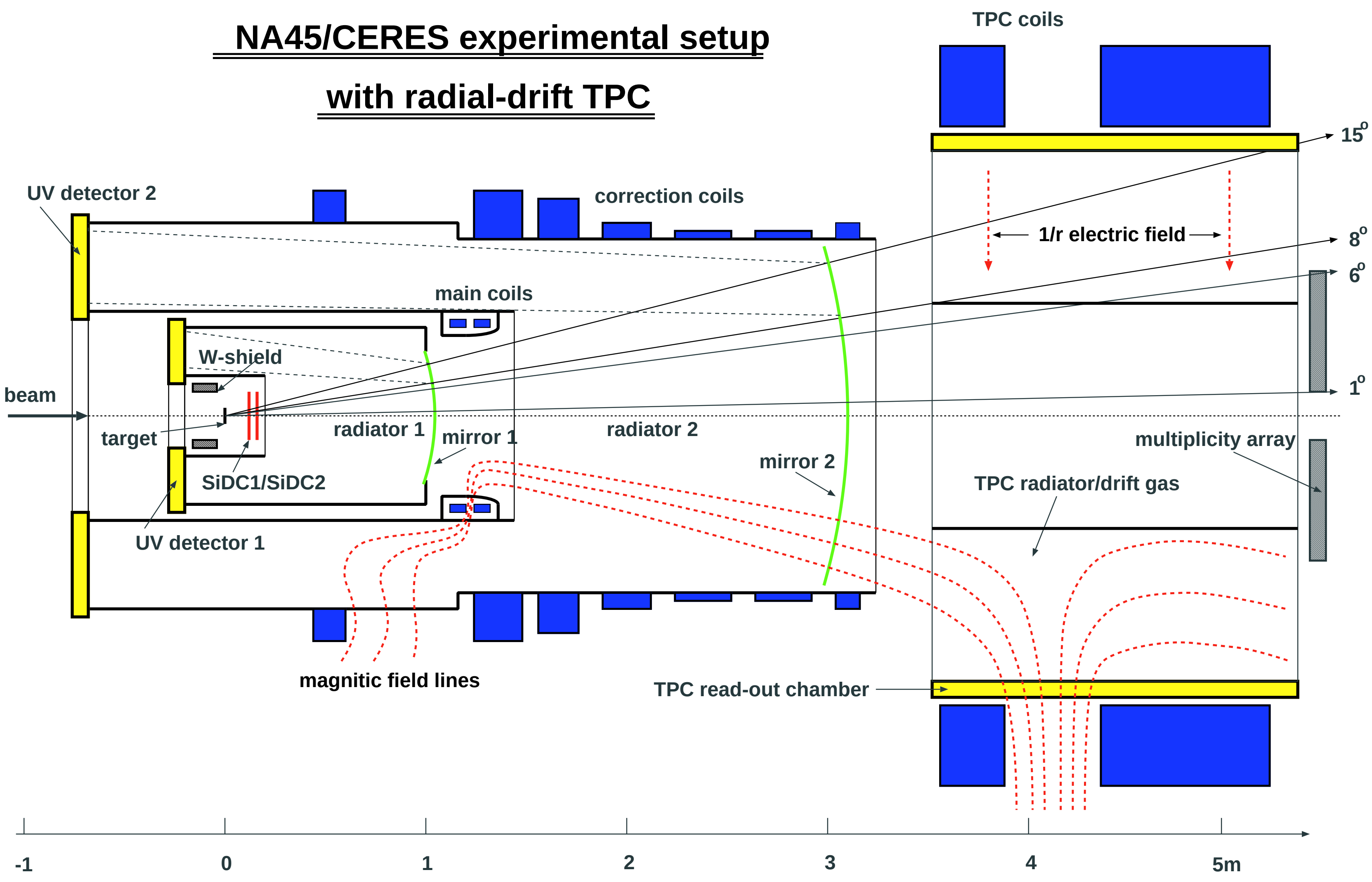

Figure 4.14: Schematic view of the upgraded CERES spectrometer.

repeated with the upgraded spectrometer at the end of year 2000. In addition, the CERES collaboration will perform measurements of Pb – Au collisions at low energies, of about 40 GeV per nucleon where the baryon density is expected to be highest, in 1999.

Appendices

Appendix A

A Toy Model: Building "Signal" out of Statistical Fluctuations

In order to investigate possible implications of using real data for tuning the cuts, we generate two N-dimensional samples of equal size, A and B, where all N parameters have the same normal distribution[1], truncated at $\pm 3\sigma$. Then we apply N cuts on the N parameters one after the other. Each cut value is chosen to maximize the value of the "background-free equivalent" $(A - B)^2/(A + B)$. We vary cut values in the range 0–2σ around the mean value of $+1\ \sigma$.

The background-free equivalent, or the effective signal S_{eff} is defined as the signal size with the same statistical accuracy as if it were to have zero background:

$$\frac{\Delta S_{eff}}{S_{eff}} = \frac{1}{\sqrt{S_{eff}}} = \frac{\Delta S}{S} = \frac{\sqrt{U+L}}{S} \tag{A.1}$$

and consequently

$$S_{eff} = \frac{S^2}{S+2L} \tag{A.2}$$

We performed this procedure 1000 times, each time generating a pair of 6-dimensional samples and applying the cut values adjustment algorithm. The distribution of the resulting "signal" (A – B) is shown in Fig. A.1. Beginning with 100 000 "like" pairs and the same amount of "unlike" we end with an average sample of 60290 "unlike" and 60050 "like" pairs, thereby yielding an average net signal of 240±100.

[1] Normal distribution is a good approximation to most of the relevant parameters, since technically each cut value is applied to each one of the two tracks of the pair, so even very asymmetric distributions are "normalized".

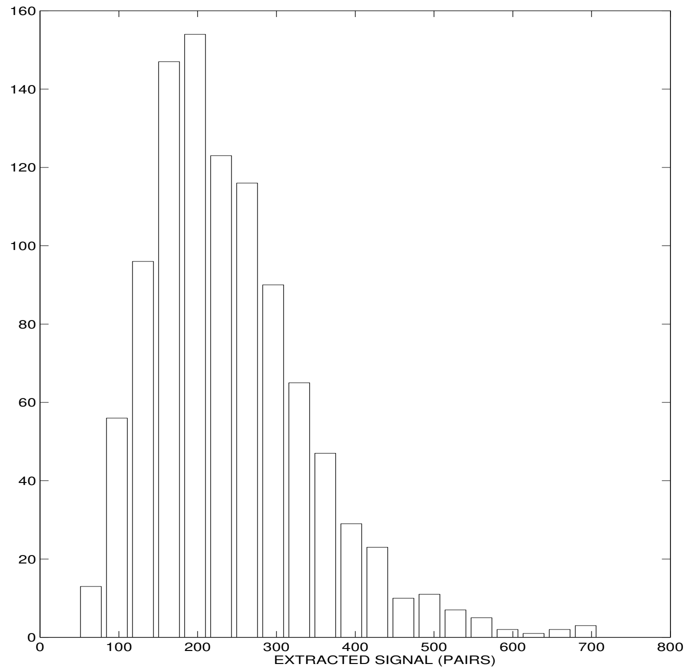

Figure A.1: Building a signal out of fluctuations while optimizing cuts. Starting point: 10^5 "like" pairs and 10^5 "unlike". 6 cuts are "optimized".

Appendix B

Energy Deposition by Conversions Inside the SiDC-1

The amplitude a of a γ-conversion occuring inside the SiDC-1 is proportional to:
i) the energy loss of two minimum ionizing particles per unit length and
ii) the ionization path x, i.e. distance travelled by the e^+e^- pair from the conversion point to the downstream side of the SiDC detector.
Therefore a is equal to

$$a = \frac{dE}{dx} \cdot x,$$

The amplitude a is distributed according to a probability density function $h(a)$ which in turn depends on the probability density functions of dE/dx and x.

The energy loss per unit length dE/dx is distributed according to the distribution function f(dE/dx), which is a convolution of two Landau distributions. The ionization path x is distributed uniformly (we measure the distance in units of thickness of the silicon wafer), since a γ-conversion can occur at any depth in the silicon wafer with equal probability, so its distribution function $g(x)$ is given by

$$g(x) = \begin{array}{ll} 1 & \text{if } 0 < x < 1 \\ 0 & \text{otherwise.} \end{array}$$

Denoting dE/dx= y we obtain for the probability function $P(a < z)$ (which is an integral of the distribution function $h(a)$)

$$P(a < z) = \int_{y \cdot x < z} g(x)\ f(y) dx dy$$

i.e.

$$P(a < z) = \int_0^\infty f(y) dy \int_0^{min(1,z/y)} dx = \int_0^z f(y) dy + \int_z^\infty f(y) \frac{z}{y} dy$$

Taking the derivative to obtain the distribution function $h(a)$ from the probability function $P(a)$ yields

$$h(z) = \frac{dP(a < z)}{dz} = f(z) + \int_z^\infty \frac{f(y)}{y} dy - f(z)$$

Finally,

$$h(a) = \int_a^{\infty} \frac{f(y)}{y} dy,$$

where
$h(a)$ is the amplitude distribution of the SiDC-1 conversions, and
$f(y)$ is the amplitude distribution of the double hits.

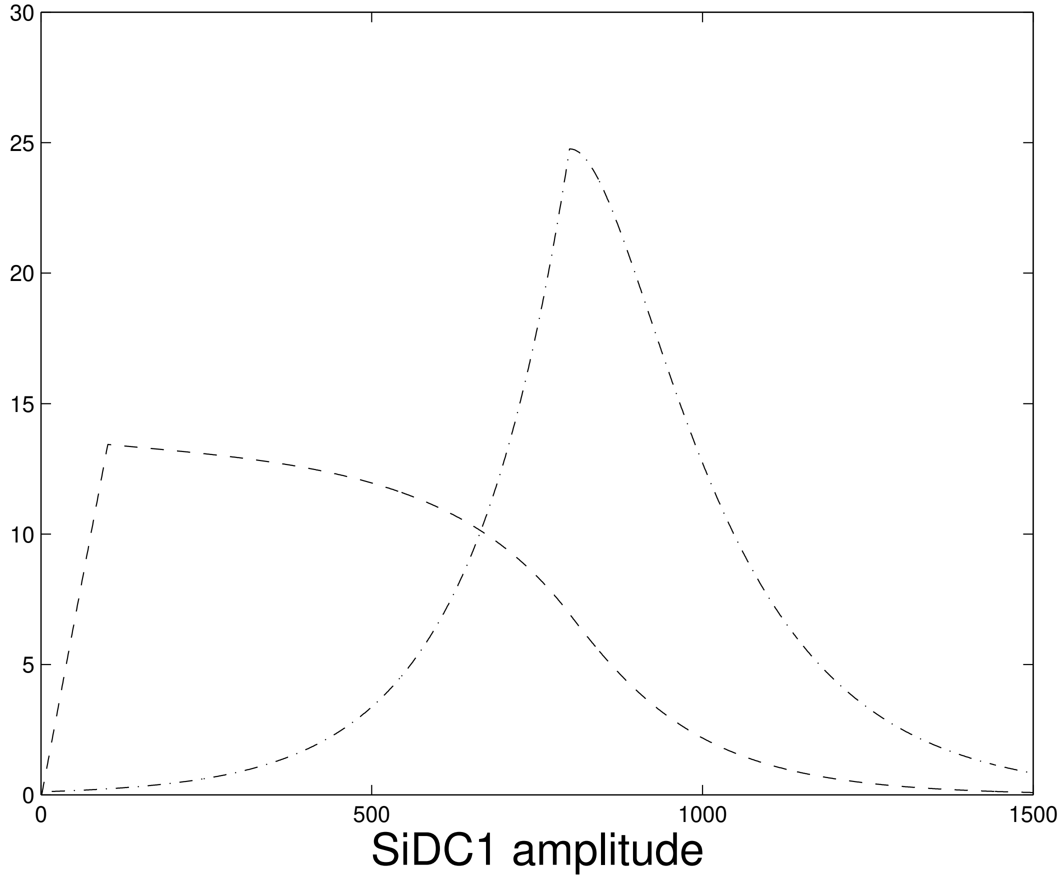

Figure B.1: Amplitude distribution in SiDC-1 of a double hit from unresolved target conversions (dashed-dotted line) and of hits from conversions originating in the SiDC-1 (dashed line).

Appendix C

Combinatorial Background Subtraction

As was shown in sect 3.6, like-sign pairs are formed from combinatorial background only, while unlike-sign pairs have both signal and background contributions. The background part B of the unlike-sign pair sample is calculated as

$$\mathrm{B} = 2\ (\mathrm{N}_{e^+e^+}\ \cdot \mathrm{N}_{e^-e^-})^{1/2}.$$

In the case of charge symmetry, i.e. when $\mathrm{N}_{e^+e^+}$= $\mathrm{N}_{e^-e^-}$, this is a trivial result:

$$\mathrm{N}_{e^+e^+} = \mathrm{N}_{e^-e^-}, \mathrm{N}_{e^+e^-} = \mathrm{N}_{e^+e^+} + \mathrm{N}_{e^-e^-} = 2\ \cdot N = 2\ (\mathrm{N}_{e^+e^+}\ \cdot \mathrm{N}_{e^-e^-})^{1/2}.$$

We will show now that this assumption is also valid when the detector has different reconstruction efficiency for positive and negative tracks, or when there is an intrinsic imbalance between positive and negative tracks. The simple relation

$$\mathrm{B} = \mathrm{N}_{e^+e^+} + \mathrm{N}_{e^-e^-}$$

obviously does not hold in this case. In the general case that we are considering the relevant quantities are the probabilities of detection of positive-sign and negative-sign tracks p_+ and p_-. The probabilities of detection of $++$, $--$, $+-$ pairs are respectively

$p_{++} = p_+^2$
$p_{--} = p_-^2$

$p_{+-} = 2p_+p_-$

since combinations $+-$, $-+$ have equal probability. Therefore

$$p_{+-} = 2\sqrt{p_{++}\, p_{--}}$$

A non-uniform reconstruction efficiency in the azimuthal direction is a source of asymmetry between p_+ and p_-. Suppose that the SiDC and the PC have dead areas in the radial direction, both of width $\Delta\varphi$, rotated by φ one with respect to the other, e.g. the PC dead area is rotated by $+\varphi$ (counter-clockwise) with respect to that of the SiDC. The rotation angle φ corresponds to the deflection of particles having a momentum $p = K/\varphi$, $K \sim 93$ GeV $\cdot$ mrad. Then for the subsample of particles with momentum p the reconstruction efficiency is asymmetric:
– for positive particles, the inefficiency due to the dead areas is $\Delta\varphi/2\pi$, since a particle lost in SiDC is also lost in the PC;
– for negative particles, the inefficiency due to the dead areas is $2(\Delta\varphi/2\pi)$, since the dead areas in SiDC and PC loose different particles.

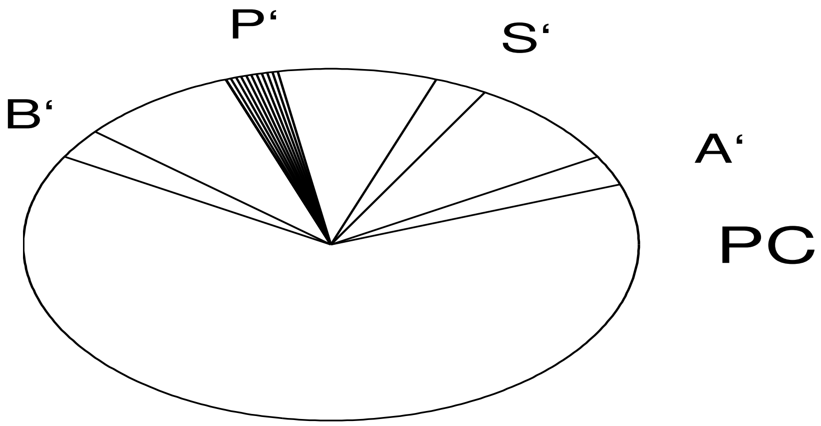

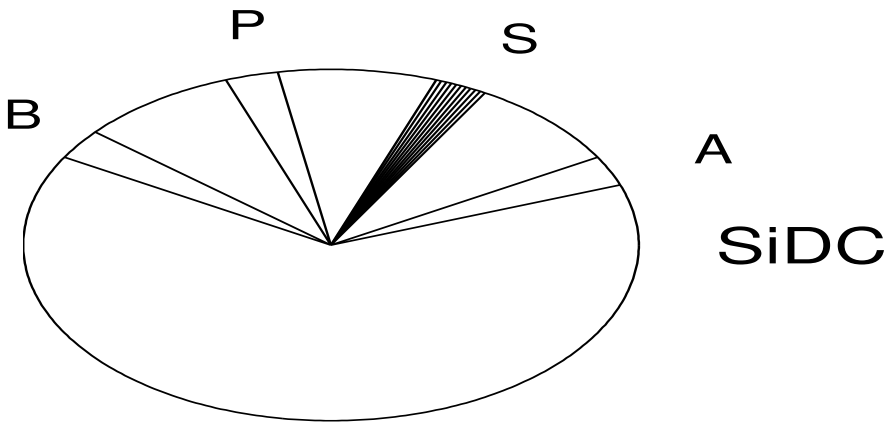

Figure C.1: Schematic figure illustrating the effect of dead areas in the reconstruction efficiency of positive vs. negative charged particles. S is a dead area in the SiDC, P‘ is a dead area in the PC (rotated counter-clockwise by an angle $+\phi$). From all positive particles deflected counter-clockwise in the magnetic field by an angle ϕ, only those having a trajectory $S \rightarrow P$‘ are lost ($A \rightarrow S$‘, $P \rightarrow B$‘ are not). From all negative particles of the same momentum (deflected clockwise), $S \rightarrow A$‘ and $B \rightarrow P$‘ are lost: the former in the SiDC and the latter in the PC.

Bibliography

[1] S.A. Bass et al. *Signatures of Quark-Gluon Plasma formation in high energy heavy-ion beams: a critical review.* Preprint DOE/ER/40561-11-INT98; J. Phys. G: Nucl. Part. Phys, in press.

[2] J.W. Harris and B. Müller *The search for the Quark-Gluon Plasma.* Annu. Rev. Nucl. Part. Sci. **46** (1996), 71–107.

[3] I. Tserruya. *Heavy ion collisions.* CERN-PPE/95-185 and Proceedings of the International Europhysics Conference on High Energy Physics, Brussels, Belgium, 1995.

[4] A.M. Poskanzer et al. - Editors. Quark Matter 95 Proceedings. *Nucl. Phys.*, **A590** (1995).

[5] P. Braun-Munzinger et al. - Editors. Quark Matter 96 Proceedings. *Nucl. Phys.*, **A610** (1996).

[6] T. Hatsuda et al. - Editors. Quark Matter 97 Proceedings. *Nucl. Phys.*, **A638** (1998).

[7] L. Riccatti et al. - Editors. Quark Matter 99 Proceedings. *Nucl. Phys.*, **A**, in press.

[8] R. Pisarski, *Phenomenology of the chiral phase transition.* Phys. Lett. **B110** (1982) 155–158.

[9] T. Alber et al. (NA49 collaboration), *Transverse energy production in* $^{208}Pb + Pb$ *collisions at 158 GeV per nucleon.* Phys. Rev. Lett. **75** (1995) 3814–3817.

[10] A. Shor. ϕ *meson production as a probe of the Quark-Gluon Plasma.* Phys. Rev. Lett. **54** (1985) 1122–1125.

[11] J. Izuka, K. Okada and D. Shito. *Systematics and phenomenology of boson mass levels.* Prog. Theor. Phys. **35** (1966) 1061.

[12] P. Koch, B. Müller and J. Rafelski. *Strangeness in relativistic heavy-ion collisions.* Phys. Rep. **142** (1986) 167.

[13] S.D. Drell and T.M. Yan. *Massive lepton pair production in hadron - hadron collisions at high-energies.* Phys. Rev. Lett., **25** (1970) 316–320.
S.D. Drell and T.M. Yan. *Partons and their applications at high-energies.* Ann. Phys., **66** (1971) 578.

[14] T. Matsui and H. Satz. *J/ψ suppression by quark-gluon plasma formation.* Phys. Lett. **B178** (1986), 416–422.

[15] A. Shor. *Charm production in a Quark-Gluon Plasma.* Phys. Lett. **B215** (1988) 375–380.

[16] K. Kajantie et al. *Dilepton emission and the QCD phase transition in ultrarelativistic nuclear collisions.* Phys. Rev. **D34** (1986) 2746–2754.

[17] R. Baur et al., (CERES-Collaboration), *The CERES RICH detector system*,(Proc. First Workshop on RICH Detectors, Bari 1993) Nucl. Inst. Meth. **A343** (1994) 87–98.

[18] G. Agakichiev et al. (CERES-Collaboration), *Systematic study of low-mass electron pair production in p–Be and p–Au collisions at 450 GeV/c.* Eur. Phys. J **C4** (1998) 231–247.

[19] G. Agakichiev et al. (CERES-Collaboration), *Enhanced production of low-mass electron pairs in 200 GeV/nucleon S-Au collisions at the CERN super-proton synchrotron.* Phys. Rev. Lett., **75** (1995) 1272–1275.

[20] V. Steiner. *The CERES Spectrometer for the Measurement of Electro-Positron Pairs in Relativistic Hadron Collisions.* Ph. D. Thesis, Rehovot, Israel (1993).

[21] R. Baur et al., *In-beam experience from the CERES UV-detectors: Prohibitive spark breakdown in multi-step parallel-plate chambers as compared to wire chambers*, (Proc. First Workshop on RICH Detectors, Bari 1993) Nucl. Inst. Meth. **A343** (1994) 231–240.

[22] W.Chen et al. (CERES collab.) *Performance of the multianode cylindrical silicon drift detector in the CERES NA45 experiment: first results.* Nuc. Inst. Meth. **A326** (1993) 273–278.

[23] A. Cherlin. *Charged hadron production in Pb-Au collisions at 158 A GeV using the CERES spectrometer.* M.Sc. Thesis, Rehovot, Israel (1998).

[24] G. Agakichiev et al. (CERES Collaboration). *Hadron physics with CERES: spectra and collective flow.* Nucl. Phys. **A638** (1998) 467c–470c.
F. Ceretto. *Charged hadron production in Pb-Au collissions at 158 AGeV/c.* Doctoral Thesis, University of Heidelberg, Germany (1998).

[25] F. Sauli, *Principles of operation of multiwire proportional chambers.* preprint CERN 77-09 (1977)

[26] M. Benayoun et al., *Impact reconstruction in pad chambers.* NIM **A342** (1994) 483–494.

[27] CERN Programm Library. See *http : //www.cern.ch*

[28] G. Agakichiev et al. *A new robust fitting algorithm for vertex reconstruction in the CERES experiment.* Nuc. Inst. Meth. **A394** (1997) 225–231.

[29] P.V.C. Hough. *Methods and means for recognizing complex patterns.* U.S. Patent 3069654, 1962.

[30] P. Braun-Munzinger, D. Miskoviec, A. Drees, C. Laurenco. *Open charm contribution to dilepton spectra produced in nuclear collisions at SPS energies.* Eur. Phys. J. , **C1** (1998) 123–130.

[31] S.V. Afanasiev et al., (NA49 collaboration) *Hadron yields and hadron spectra from the NA49 experiment.* Nucl. Phys. **A610** (1996) 188c–199c.

[32] I.G. Bearden et al., (NA44 collaboration) *Hadron distributions – recent results from the CERN experiment NA44.* Nucl. Phys. **A610** (1996) 175c–187c.

[33] M. Aggarwal et al., (WA98 collaboration) *Photon and neutral meson production in 158 AGeV ^{208}Pb+Pb collisions.* Nucl. Phys. **A610** (1996) 200c–212c.

[34] G. Agakichiev et al. (CERES Collaboration), *Neutral meson production in p–Be and p–Au collisions at 450 GeV beam energy.* Eur. Phys. J. **C4** (1998) 249–257.

[35] G. Tel-Zur. *Electron pair production in p - Be and p - Au collisions at 450 GeV/c.* Ph.D. Thesis, Weizmann Institute of Science, Rehovot, Israel (1996).

[36] *Review of particle properties.* Phys. Rev. **D54** (1996).

[37] M. Aguilar-Benitez et al. *Inclusive particle production in 400 GeV/c pp-interactions.* Z. Phys. **C50** (1991) 405–426.

[38] L.D. Landau and E.M. Lifshitz Course of Theoretical Physics. vol. 4 (second edition) *Quantum Electrodynamics.* Pergamon Press, 1982 §94.

[39] G. Agakichiev et al. (CERES Collaboration), *Low-mass* e^+e^- *pair production in 158 A* GeV *Pb–Au collisions at the CERN SPS, its dependence on multiplicity and transverse momentum.* Phys. Lett. **B422** (1998) 405.
G. Agakichiev et al. (CERES Collaboration), *CERES results on low-mass electron pair production in Pb-Au collisions.* Nucl. Phys. **A638** (1998) 159c–170c.

[40] V. Cerny, P. Lichard, and J. Pisut, *A clear-cut test of low mass dilepton production mechanism in hadronic collisions.* Z. Phys. **C31** (1986) 163–166.

[41] E.L. Feinberg. Nuovo Cimento,**34a** (1976) 391.

[42] J. Cleymans,K. Redlich and D.K.Strivastava. *Equation of state of hadronic matter and electromagnetic radiation from relativistic heavy ion collisions.* Phys. Lett. **B420** (1998) 261.

[43] B. Lenkeit. *Elektron-Positron-Paar Emission in Pb-Au-Kollisionen bei 158 A GeV/c.* Doctoral Thesis. University of Heidelberg, Germany (1998).

[44] B. Lenkeit for the CERES collaboration. *Recent results from Pb–Au collisions at 158 GeV/c per nucleon.* Quark Matter 99 Proc., to be published in Nucl. Phys. **A**.

[45] M. Masera for the HELIOS-3 Collaboration, *Dimuon production below mass 3.1* GeV/c^2 *in p-W and S-W interactions at 200 GeV/c/A.* Nucl. Phys. **A590** (1995) 93c–102c.

[46] I. Tserruya. *Summary of low-mass dilepton and direct photon results.* Nucl. Phys. **A590** (1995) 127c–138c.

[47] D.Jouan (NA50 Collaboration), *ϕ, ρ and ω production in collisions induced by deutron and heavy ions around 200 GeV per nucleon.* Nucl.Phys. **A638** (1998) 483c–486c;
A.de Falco (NA50 Collaboration), *NA38/NA50 results on the low mass dimuon spectra.* Nucl.Phys. **A638** (1998) 487c–490c.

[48] R. Albrecht et al. (WA80 Collaboration), *Production of η mesons in 200 A GeV/c S+S and S+Au reactions.* Phys. Lett. **B361** (1995) 14.

[49] T. Peitzmann et al. (WA98-Collaboration), *Probing the final and initial state in ultrarelativistic heavy ion collisions – results from the WA98 experiment.* Proceedings of the 29th International Conference on High Energy Physics (ICHEP98, Vancouver). World Scientific, 1999, pp. 1469–1473.

[50] P. Braun-Munzinger, I. Heppe and J. Stachel, nucl-th/9903010

[51] J. Stachel,*Towards the quark-gluon plasma.* To be published in Nucl. Phys. **A** (1999).

[52] I. Tserruya. *Dileptons and photons at the CERN SPS.* Prog. Theor. Phys. Suppl. **129** (1997) 145–160.

[53] G. Q. Li, C. M. Ko and G. E. Brown, *Effects of in-medium vector meson masses on low-mass dileptons from SPS heavy-ion collisions.* Nucl. Phys. **A606** (1996) 568–606
G. Q. Li, C. M. Ko, G. E. Brown and H. Sorge, *Dilepton production in proton-nucleus and nucleus-nucleus collisions at SPS energies.* Nucl. Phys. **A611** (1996) 539–567.

[54] W. Cassing, W. Ehehalt and I. Kralik, *Analysis of the HELIOS-3 $\mu^+\mu^-$ data within a relativistic transport approach.* Phys. Lett. **B377** (1996) 5–10.

[55] D.K. Srivastava, B. Sinha and C. Gale, *Excess production of low-mass lepton pairs in S+Au collisons at the CERN Super Proton Synchrotron and the quark-hadron phase transition.* Phys. Rev. **C53** (1996) R567–R571.

[56] C.M Hung and E.V. Shuryak, *Dilepton and/or photon production in heavy ion collisions and the QCD phase transition.* Phys. Rev. **C56** (1997) 453–467.

[57] J. Sollfrank, P. Huovinen, M. Kataja, P.V. Ruuskanen, M. Prakash, and R. Venugopalan, *Hydrodynamical description of 200A GeV/c S+A collisions; hadron and electromagnetic spectra.* Phys. Rev. **C55** (1997) 392–410.

[58] G. E. Brown and M. Rho, *Scaling effective Lagrangians in a dense medium.* Phys. Rev. Lett. **66**, (1991) 2720–2723.

[59] R. Rapp, G. Chanfray and J. Wambach, *Rho meson propagation and dilepton enhancement in hot hadronic matter.* Nucl. Phys. **A617** (1997) 472–495.
J. Wambach, R. Rapp, *Theoretical interpretations of low-mass dileptons.* Nucl. Phys. **A638** (1998) 171c–182c.

[60] W. Cassing, E.L. Bratkovskaya, R. Rapp and J. Wambach, *Probing the ρ spectral function in hot and dense nuclear matter by dileptons.* Phys. Rev. **C57** (1998) 916–921.

[61] R. Rapp, Proc. Quark Matter 99 Nucl. Phys. A (in press), hep-ph/9907342.

[62] I. Zahed, *Electromagnetic Emission Rates and Spectral Sum Rules* Nucl. Phys. **A638** (1998) 495.

[63] J.V. Steele, H. Yamagishi and I. Zahed, *Dilepton and photon emission rates from a hadronic gas.* Phys. Rev **D56** (1997) 5605

[64] V. Koch, Preprint nucl-th/9903008.

[65] P. Huovinen and M. Prakash, e^+e^- *yields in Pb+Au collisions at 158 A GeV/c: assessment of baryonic contributions.* Phys. Lett. **B450** (1999) 15–23.